

## **INFORMATION TO USERS**

**This manuscript has been reproduced from the microfilm master. UMI films the text directly from the original or copy submitted. Thus, some thesis and dissertation copies are in typewriter face, while others may be from any type of computer printer.**

**The quality of this reproduction is dependent upon the quality of the copy submitted. Broken or indistinct print, colored or poor quality illustrations and photographs, print bleedthrough, substandard margins, and improper alignment can adversely affect reproduction.**

**In the unlikely event that the author did not send UMI a complete manuscript and there are missing pages, these will be noted. Also, if unauthorized copyright material had to be removed, a note will indicate the deletion.**

**Oversize materials (e.g., maps, drawings, charts) are reproduced by sectioning the original, beginning at the upper left-hand corner and continuing from left to right in equal sections with small overlaps.**

**Photographs included in the original manuscript have been reproduced xerographically in this copy. Higher quality 6" x 9" black and white photographic prints are available for any photographs or illustrations appearing in this copy for an additional charge. Contact UMI directly to order.**

**Bell & Howell Information and Learning  
300 North Zeeb Road, Ann Arbor, MI 48106-1346 USA  
800-521-0600**

**UMI<sup>®</sup>**



**AN INVESTIGATION OF SMALL-SCALE  
RELATIONSHIPS BETWEEN OPTICAL AND HF  
RADAR AURORA**

A  
THESIS

*Presented to the Faculty  
of the University of Alaska Fairbanks*  
  
*in Partial Fulfillment of the Requirements  
for the Degree of*

**DOCTOR OF PHILOSOPHY**

By

Veronika Besser, Cand. Scient.

Fairbanks, Alaska

December 2000

UMI Number: 9992685

UMI<sup>®</sup>

---

UMI Microform 9992685

Copyright 2001 by Bell & Howell Information and Learning Company.

All rights reserved. This microform edition is protected against  
unauthorized copying under Title 17, United States Code.

---

Bell & Howell Information and Learning Company  
300 North Zeeb Road  
P.O. Box 1346  
Ann Arbor, MI 48106-1346

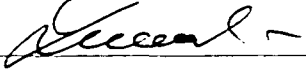
AN INVESTIGATION OF SMALL-SCALE RELATIONSHIPS  
BETWEEN OPTICAL AND HF RADAR AURORA

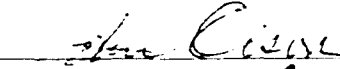
By

Veronika Besser

RECOMMENDED:

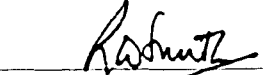




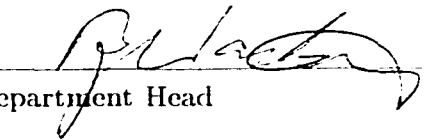







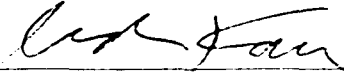


Advisory Committee Chair

  
Department Head

APPROVED:

  
Dean, College of Science, Engineering, and Mathematics

  
Dean of the Graduate School

12-1-00  
Date

# Abstract

An investigation is undertaken of the relationship between visual aurora and the occurrence of radar-detectable irregularities in the nightside ionosphere. Understanding how auroral signatures appear in HF radar backscatter could combine the advantages of detailed information about auroral fluxes in optical measurements with extended coverage of HF radars. Auroral particle precipitation ionizes the ionosphere and creates localized plasma density enhancements. Irregularities with various smaller sizes are generated from larger density structures through instability-induced cascading. HF waves are coherently scattered by decameter structures within the ionospheric plasma. Hence aurorally induced irregularities can be seen by the radar in the form of “HF radar aurora.”

A statistical treatment of the occurrence of optical and HF radar aurora reveals a high degree of variability in backscatter patterns even under seemingly similar auroral displays. The small-scale correspondence between visual aurora and HF backscatter thus represents a more differentiated picture than the spatially and temporally averaged data of earlier studies. The relationship between the occurrence or the characteristics of aurora and the occurrence of HF echoes can therefore not be quantified.

An analysis of single events isolates processes that lead to the observed variety of backscatter patterns in the presence of aurorally induced irregularities. They involve the ambient ionospheric density and localized enhanced densities at different altitude regimes and locations in the path of the radar signal. Conditions for HF wave propagation are partly determined by the aurora itself, partly they are imposed by ambient ionospheric density levels. It is found that low or high ambient densities have a dominating effect on the success of ionospheric probing. Low densities hamper the return of radar signals despite the presence of irregularities. High ambient densities can overcome some of the adverse effects on HF wave propagation associated with sporadic  $E$ . The information contained in the diversity of the relationships between optical and HF backscatter improves thus our knowledge about the nighttime ionosphere. A more detailed specification of ionospheric parameters is necessary to gain better insight into these relationships.

# Contents

List of Figures . . . . .	vi
List of Tables . . . . .	ix
Acknowledgements . . . . .	x
<b>1 Introduction</b>	<b>1</b>
<b>2 Irregularities at <i>F</i> Region Auroral Latitudes: An Overview</b>	<b>4</b>
2.1 Introduction . . . . .	4
2.2 Irregularity Research in History . . . . .	5
2.3 Ionospheric Equilibrium Densities . . . . .	6
2.4 Irregularity Occurrence . . . . .	9
2.5 Source Regions and Irregularity Production . . . . .	12
2.5.1 Convection of Subsolar Plasma . . . . .	12
2.5.2 Particle Precipitation . . . . .	13
2.5.3 Plasma Instabilities . . . . .	16
2.5.4 Electrostatic Turbulence . . . . .	20
2.6 Transport and Lifetime . . . . .	23
2.7 Detection Methods . . . . .	26
2.7.1 Coherent Scatter Radars . . . . .	26
2.7.2 Scintillation . . . . .	29
2.7.3 Plasma Density Measurements . . . . .	30
<b>3 Instrumentation and Site Characteristics</b>	<b>33</b>
3.1 SuperDARN HF Radar . . . . .	33

3.1.1	Radar Specifications and Variables . . . . .	35
3.1.2	Propagation Modes . . . . .	39
3.2	Meridian Scanning Photometer . . . . .	42
3.3	Allsky Camera . . . . .	48
<b>4</b>	<b>Analysis of Optical and HF Radar Data</b>	<b>51</b>
4.1	Comparison With Dayside Conditions and Other Studies . . . . .	52
4.2	Outline of the Observations . . . . .	53
4.3	Statistics of Aurora and HF Backscatter on Small Scales . . . . .	59
4.4	Data Sampling on Larger Scales . . . . .	63
4.5	Aspects of the Small-scale Relationships Between Optical and HF Aurora .	71
4.5.1	Aurora-induced Backscatter in Quiet Times . . . . .	71
4.5.2	Irregularity Growth . . . . .	78
4.5.3	Insufficient Ray Refraction through Low Ionospheric Densities . . . .	81
4.5.4	No Irregularities through High Ionospheric Densities . . . . .	87
4.5.5	Aspect Sensitivity . . . . .	90
4.5.6	Unfavorable Ray Propagation through High <i>E</i> Region Densities . . . .	93
4.5.7	Radio Wave Attenuation through High <i>D</i> Region Densities . . . . .	98
4.5.8	Backscatter under Disturbed Auroral Conditions . . . . .	103
<b>5</b>	<b>Discussion and Conclusion</b>	<b>107</b>
5.1	About the Importance of Ionospheric Densities . . . . .	109
5.2	Convection and the Role of the IMF . . . . .	115
5.3	Suggestions for Further Work . . . . .	120
5.4	Conclusions . . . . .	122
<b>6</b>	<b>Summary</b>	<b>124</b>
<b>A</b>	<b>Statistical Approach</b>	<b>128</b>
	<b>Bibliography</b>	<b>132</b>



# List of Figures

2.1	Electron density profiles at auroral latitudes for summer (left) and winter (right) days and nights under solar minimum and maximum conditions (IRI-95). . . . .	9
2.2	Statistical scintillation boundaries of $F$ layer irregularities under more disturbed (solid line) and less disturbed (dashed region) geomagnetic conditions. . . . .	10
2.3	Morphology of two HF backscatter curtains for three (local) geomagnetic disturbance levels and comparison with morphologies of the equatorward diffuse auroral boundary and <i>in situ</i> irregularity. . . . .	11
2.4	Nighttime electron densities as a function of altitude and invariant latitude. . . . .	15
2.5	Geometry of the $\mathbf{E}' \times \mathbf{B}$ gradient drift instability. . . . .	17
2.6	Volume scattering from layers with spatial periods $d$ for a wavelength $\lambda$ . . . . .	28
3.1	The antenna arrays of the SuperDARN HF radar at Pykkvibær, Iceland. . . . .	34
3.2	Modelled beam pattern for beams 4 and 6 and a 10 MHz frequency. . . . .	35
3.3	Example for a scatter diagram for one radar beam (Kodiak, February 8, 2000). . . . .	40
3.4	Modelled HF ray tracing for a given electron density, an azimuth of $30^\circ$ away from magnetic north, and a frequency of 12 MHz. . . . .	41
3.5	Schematic setup of the MSP, shown here with three channels. . . . .	42
3.6	MSP mount with five channels at the Longyearbyen Auroral Station. . . . .	43
3.7	Example for a MSP keogram (Poker Flat, February 8, 2000). . . . .	44
3.8	Mapping of MSP zenith angles to an altitude of 250 km. . . . .	46
3.9	Original and projected emission profile of a tall field-aligned auroral structure for a flat Earth. . . . .	47

3.10	Effects of altitude projection of MSP zenith angles to three different altitudes.	48
3.11	Schematic setup of the ASC. . . . .	49
3.12	Mapping of zenith angles to an altitude of 110 km. . . . .	50
4.1	All-day scatter results for SD Kodiak, beam 1, on February 24, 2000. . . . .	58
4.2	FOVs of the SuperDARN Kodiak radar, and the MSP and ASC at Poker Flat.	60
4.3	FOVs of the Pykkvibær and the Hankasalmi CUTLASS/SuperDARN radars, and the MSP and allsky camera at Longyearbyen. . . . .	61
4.4	Four day averages of SD Kodiak (upper panel) and Poker Flat MSP data (lower panel) for Kp values between 0 and 2 <sup>-</sup> . . . . .	65
4.5	Four day averages of SD Kodiak (upper panel) and Poker Flat MSP data (lower panel) for Kp values between 3 and 5 <sup>-</sup> . . . . .	66
4.6	Six day averages of CUTLASS Hankasalmi (upper panel), Pykkvibær (middle panel), and MSP Longyearbyen data (lower panel) with Kp values between 0 and 1 <sup>+</sup> . . . . .	68
4.7	Four day averages of CUTLASS Hankasalmi (upper panel), Pykkvibær (mid- dle panel), and MSP Longyearbyen data (lower panel) with Kp values be- tween 2 and 4 <sup>+</sup> . . . . .	70
4.8	Kodiak backscatter (upper panel), Poker Flat MSP auroral brightness (mid- dle panel) for 630 nm (red color) and 427.8 nm (blue color), and the total number of scatter and auroral cells in the MSP scanning plane (lower panel) on March 3, 2000. . . . .	75
4.9	Ratio of the red and blue emissions on March 3, 2000. . . . .	76
4.10	<i>E</i> region radar aurora from the Elmendorf 50 MHz coherent scatter radar on March, 3 2000. . . . .	77
4.11	Alaskan observations in the same format as in figure 4.8, for February 24, 2000.	80
4.12	Alaskan observations in the same format as in figure 4.8, for February 8, 2000.	82
4.13	Modelled ray tracing for the meridional radar beam on March 3, 2000, 8:45 UT. . . . .	84
4.14	Modelled ray tracing for the meridional radar beam on February 8, 2000, 09:14 UT. . . . .	85

4.15	Aurora and radar scatter on February 8, 2000, 09:50 UT. . . . .	86
4.16	North European observations in the same format as in figure 4.8, except for Pykkvibær and Longyearbyen data on December 5, 1997. . . . .	89
4.17	Alaskan observations in the same format as in figure 4.8, for February 9, 2000.	95
4.18	<i>E</i> region radar aurora from the Elmendorf 50 MHz coherent scatter radar on February 9, 2000. . . . .	96
4.19	Modelled ray tracing for the meridional radar beam on February 9, 2000, 07:14 UT. . . . .	96
4.20	Aurora and radar scatter on February 9, 2000, 07:14 UT. . . . .	97
4.21	Modelled ray tracing for the meridional radar beam on February 9, 2000, 07:59 UT. . . . .	98
4.22	Alaskan observations in the same format as in figure 4.8, for March 1, 2000.	104
4.23	<i>E</i> region radar aurora from the Elmendorf 50 MHz coherent scatter radar on March 1, 2000. . . . .	105
4.24	Modelled ray tracing for the meridional radar beam for assumed ionospheric conditions. . . . .	105
5.1	SNR and elevation angle for $\langle \Delta N^2 \rangle^{1/2} = 10^4$ , $z_{max} = 300$ km, $z_{1/2} = 150$ km, $N_{max} = 10^5$ cm <sup>-3</sup> , and a radar frequency of 8.5 MHz (left) and 14.5 MHz (right). . . . .	112
5.2	Convection of dayside plasma to the nightside. . . . .	117
5.3	IMF data by Wind for March 1, 2000. . . . .	119
5.4	IMF data by Wind for February 8, 2000. . . . .	119

# List of Tables

4.1	Overview over the data days taken in Alaska. . . . .	55
4.2	Overview over the data days taken in Northern Europe. . . . .	56
4.3	$D$ region absorption during the Alaskan data periods, as measured by the riometer in Gakona. . . . .	101
5.1	$F_2$ region parameter for the Alaskan data periods, as measured by the ionosonde in Gakona. . . . .	111
A.1	Product moment correlation coefficients for various combinations of auroral and backscatter occurrence. . . . .	129

# Acknowledgements

It has been a great pleasure to work in the Last Frontier of Alaska and space physics research. I am very grateful to faculty, staff and my fellow students for their contribution to the excellent working and studying conditions at the Geophysical Institute.

In particular I want to thank my academic advisor, Roger Smith. He opened the door to Alaska for me when I first met him at the Auroral Station in Longyearbyen, Svalbard, while I was a student at the University of Tromsø. Although he was increasingly involved in the administration of the Geophysical Institute, I could always count on a discussion and knowledgeable advice. I enjoyed the opportunity to conduct the experimental part of my research at the Auroral Station in Longyearbyen during part of every auroral season while I was in Alaska. In this context I also thank Geophysical Institute engineers Jim Desrochers and Dan Osborne for help and advice over the years on the assembly of instrumentation bound for Svalbard. I would like to thank the staff at UNIS, Longyearbyen, for the operation and maintenance of the optical instruments in the absence of Alaskan operators.

I want to extend my gratitude to my committee members, William Bristow, Charles Deehr, Dirk Lummerzheim, Hans Stenback-Nielsen, and John Olson for their time, professional advice, and comments on my thesis. It is a pleasure to acknowledge interesting discussions of optical data with Charles Deehr, who sometimes stepped in as second advisor. William Bristow and Dirk Lummerzheim deserve special thanks for not giving up on correcting my laborious English and long sentences. The correct mapping of allsky camera images onto geographical maps would not have been possible without the help of Hans Stenback-Nielsen and his original computer program. SuperDARN data were willingly provided by Mark Lester of the University of Leicester and William Bristow, who also supplied me with some helpful programs for data processing. Valuable ionosonde measurements were made available through the HAARP facility in Gakona, Alaska.

Furthermore, I want to thank my family for their support and interest through many years and three countries. Especially I want to thank my mother who enabled me to pick up this long path of study when I felt the need. And last but certainly not least, I thank my friend and now husband Andrei for loving support and the patience I needed to cast my research into this form.

# Chapter 1

## Introduction

The sun provides the radiation necessary for life on Earth. It also is the source of a high-speed particle stream carrying the solar magnetic field with it. The stream is called the solar wind. The Earth, with its own magnetic field, is embedded in this "wind" from the sun. Interactions between the two magnetic fields take place at the boundary between the Earth's magnetosphere and the solar-controlled domain. Energy and particles are transferred from the solar wind to the magnetosphere. The energy is stored in the magnetotail at the nightside of the Earth and periodically released. The release leads to the energization and precipitation of particles along field lines into the nightside atmosphere.

On their path toward the Earth, the precipitating particles collide with the increasingly dense neutral atmosphere. Subsequent ionization of the neutral constituents results in enhanced plasma densities in the precipitation regions. A visible result of the interaction between the precipitating particles and the gas around the Earth is the brilliant display of aurora familiar to those living at high latitudes. The enhanced plasma densities and the visual aurora are thus related to each other by a common source, the incoming particle fluxes. The purpose of this thesis is to study the relationship between both phenomena, as they are measured by ground instruments.

Optical measurements of the aurora date back more than a century. The first successful picture of an aurora was taken in 1892 in Norway [*Baschin*, 1900]. Nowadays aurora is continuously monitored, both from the ground and from satellites orbiting the Earth. Typical ground-based instruments include the television camera. Equipped with a fisheye lens, a

suitable camera can film the entire sky. Another “workhorse” for auroral data collection is the meridian scanning photometer, measuring the aurora along a slice of the sky at several of wavelengths simultaneously. Some of the different auroral wavelengths originate within different altitude regimes. Observations of the relative brightness at the different wavelengths yield information about the altitude of the auroral emissions. These two types of instruments provided the optical data for this thesis.

The systematic study of the ionospheric density structure (ionospheric irregularities) in polar regions took a large step forward with the implementation of the Super Dual Auroral Radar Network (*SuperDARN*). This network consists of a chain of 14 high-frequency (HF) radars distributed over the northern and southern high latitudes. Radio waves at HF frequencies are scattered coherently by electron density structures. Layers of irregularities with distances of half the radar wavelength enable positive interference of the scattered wave. A significant portion of the signal power is then reflected back to the radar. The *SuperDARN* radars are sensitive to irregularities with decameter sizes. The properties of the backscatter are directly related to conditions in the scattering region during the scattering process. The scattered power corresponds to the relative changes in the plasma density. Thus, the *SuperDARN* measurements generate a map of decameter-sized irregularities at polar latitudes. Data from these radars supplied the density irregularity measurements for the analysis.

An overview of irregularities in the high-latitude  $F$  region will be given in chapter 2. Statistical occurrence of irregularities and generation processes will be discussed. A description of the most common instrumentation for their detection will follow. Irregularities occur quite regularly in the auroral zone. Structures in the plasma density arise through creation of new ionization, as through auroral precipitation, and also where regions with high density and low density intermix. An example is the convection of high-density subsolar plasma into the low-density polar cap. Density gradients at the boundaries between regions with different properties imply a potentially unstable situation. In the presence of destabilizing factors, such as electric fields, field aligned currents, or velocity shear, perturbation amplitudes can grow and lead to the generation of smaller-scale irregularities. Destabilizing factors of importance for the  $F$  region will be discussed.

Chapter 3 will introduce the instrumentation used to collect the data for this thesis. A total of three HF radars located in Alaska, Iceland and Finland, two meridian scanning photometers and two allsky cameras observed the ionosphere at two different locations, over Alaska and over Svalbard, Norway.

Data acquired mostly in Alaska will be presented in chapter 4. The relationship between HF backscatter and optical aurora will be illustrated in terms of occurrence level as well as on a single case basis. Various patterns in the observations will be characterized and interpreted. Processes of importance for HF wave propagation will be explained.

Chapter 5 starts with a synthesis of the observations. The importance of ionospheric densities for the radar signal propagation will be investigated. Polar cap patches as possible sources for nighttime plasma densities will be suggested and discussed.



## Chapter 2

# Irregularities at *F* Region Auroral Latitudes: An Overview

### 2.1 Introduction

This chapter explains the nature, causes and detection of plasma irregularities. After an introduction of irregularity occurrence, a review of generation mechanisms is given followed by an overview of convection and irregularity decay properties. The last part of the chapter presents instruments used in the detection of ionospheric irregularities.

A plasma irregularity is a variation in the background ionospheric plasma density of at least a few percent or more over the background. The term plasma irregularity is commonly applied to regions with densities higher than in the background ionosphere although density cavities are also observed. Structures in the plasma density occur over a large range of scales from blobs with the size of several hundred kilometers or larger down to small scale lengths in the meter-range. At the different spatial scales, different physical processes are responsible for the generation, transport and decay. Nonlinear plasma processes couple the regimes to each other, passing energy and matter from one wavelength range into another. With conductivities and diffusion rates across the magnetic field being a fraction of their field-aligned values, density enhancements are typically field-aligned structures which extend upward into the magnetosphere [*Vickrey et al.*, 1980]. Apart from natural occurrences, man-made irregularities have been created by ionospheric heaters and by chemical releases.

## 2.2 Irregularity Research in History

Sporadically gathered knowledge about the existence of high-latitude ionospheric irregularities was obtained through blackouts or decreasing quality of HF radio transmissions when radio communication became strategically important during the Second World War. The need for a better scientific understanding of radio propagation led to a significant increase in the installation of sounding stations during the war and in the years that followed. The first systematic investigation of high-latitude  $F$  region irregularities was undertaken starting with the International Geophysical Year 1958/1959 by ground-based ionosondes and radars. It resulted in insight into the occurrence [Shimazaki, 1959; Bates, 1959] and impact of plasma anomalies on HF waves [Weaver, 1965; Hower *et al.*, 1966]. By that time generation mechanisms had been studied extensively only for lower latitudes. Based on this rich data base and theoretical work of different authors in the equatorial region, Reid [1968] estimated the relative importance of known processes in the high-latitude environment. He found that the inhibiting effect on instabilities produced by a larger magnetic dip angle at higher latitudes is more than offset by stronger ionospheric electric fields and the appreciable horizontal density gradients at auroral latitudes.

Experimental work in the 1970's and 1980's established knowledge about sizes and occurrences of ionospheric plasma structure. Instruments used in experimental studies included antennas for the detection of scintillations [Frihagen, 1971; Aarons, 1973; Rino *et al.*, 1978], coherent backscatter radars [Bates and Albee, 1969; Bates, 1970], incoherent radars [Kelley *et al.*, 1980; Vickrey *et al.*, 1980], detectors aboard rockets [Dyson *et al.*, 1974], and satellites [McClure and Hanson, 1973; Sagalyn *et al.*, 1974; Clark and Raitt, 1976]. Combined studies made it possible to correlate ground evidence with *in situ* measurements, to gather knowledge about irregularity generation. The simultaneous use of incoherent scatter radar and rockets led to evidence of a positive correlation between aurora and irregularity patterns [Kelley *et al.*, 1980]. Vickrey *et al.* [1980] investigated instability processes connected with field-aligned currents in the auroral region.

Parallel to experimental research, theories of irregularity generation mechanisms were developed. Important contributions in the field of dominant instabilities were made, among others, by Ossakow and Chaturvedi [1979], who worked analytically on the current con-

vective instability in the diffuse aurora, and *Keskinen and Ossakow* [1982] and *Keskinen and Ossakow* [1983a], who numerically simulated the evolution of  $\mathbf{E} \times \mathbf{B}$  type instabilities for long and short wavelengths, respectively. Further modelling work by *Huba et al.* [1988] and *Mitchel et al.* [1985] put the  $F$  layer anomalies in the context of a coupled ionosphere-magnetosphere system. The aspect of the influence of a conducting  $E$  region was numerically evaluated by *Vickrey and Kelley* [1982].

There are a few excellent reviews on the subject of high latitude  $F$  region irregularities. Descriptions of irregularity sources and detection techniques were covered in the work of *Fejer and Kelley* [1980] and in the extensive review of *Tsunoda* [1988]. *Hanuise* [1983] described the topic of the polar ionosphere under the aspect of irregularity detection by coherent radars. An overview over formation of plasma anomalies was given by *Keskinen and Ossakow* [1983b].

Theoretical  $F$  layer irregularity research has declined somewhat after the peak of activity in the field in the 1980's, although the subject is still considered as far from solved. Experimental detection, on the other hand, and utilization of plasma fluctuations as indicators of the state of the ionosphere, has progressed significantly since then. With the establishment of the first elements of what has become an international chain of HF radars probing the high-latitude ionosphere, the Super Dual Auroral Radar Network (SuperDARN), the foundation for large-scale monitoring of the polar environment was laid in the middle of the 1980's [Greenwald et al., 1985]. With a close correspondence between plasma drift and irregularity motion [Villain et al., 1985], detection of the convection pattern and the derived cross-polar potential became a major focus of this approach. Results on plasma motion include statistical overviews [Ruohoniemi and Greenwald, 1996], nightside convection patterns associated with aurora [Yeoman and Lühr, 1997; Voronkov et al., 1999], and plasma flow in the vicinity of auroral arcs [Weber et al., 1991].

## 2.3 Ionospheric Equilibrium Densities

The ionosphere is created by dissociation and ionization of the Earth's upper atmosphere. Photoionization, mainly due to extreme ultraviolet (EUV) and X-ray radiation of the sun, but also cosmic rays, and impact ionization due to auroral precipitation or heating processes

are responsible for charge separation in neutral constituents. The increase in density of charged particles through ionization is overall balanced by losses through recombination of electron-ion pairs during collisions. At all times, the number of positive and negative charge carriers are generally equal. Recombination rates are governed by atmospheric pressure, which decreases exponentially with height. Above 80 km altitude recombination rates are sufficiently small to allow a permanent population of ions and electrons. Production, loss, and chemical interactions with other charged particles and neutral constituents determine the density and composition of the ionosphere at any point in space. Gravity is responsible for an altitude-dependent structure in the plasma. Neglecting the curvature of the Earth as a first order approximation, the undisturbed ionosphere can be regarded as a set of horizontal layers with constant electron densities.

Although not physically separated, different height regions have their own characteristic atmospheric composition and density and, consequently, different absorption and recombination factors responding differently to ionization. They divide the ionosphere vertically into three major layers: the *D* region (below 80 km), the *E* region (between 80 and 130 km), and the *F* region (above 130 km). Most of the ionizing solar radiation is absorbed at altitudes above 80 km. Only very high-energy ionization sources reach down to *D* region heights. The high atmospheric density in the *D* region leads to high electron-neutral collision rates, which result in very small recombination rates. In general, few charged particles are therefore found in the *D* layer. Solar ionization in the *E* region is at a much higher level, because the thin atmosphere above the *E* layer does not considerably weaken the incoming EUV radiation. At these altitudes neutral pressure is decreased, compared to lower altitudes, so that electron-neutral collisions are negligible, but it is still sufficiently high to cause high ion-neutral collision rates. Fast production and loss rates determine therefore the development of the *E* layer plasma density. Continuing upward, much lower neutral densities in the *F* region reduce collision frequencies further. This results in greater relative importance of diffusion and drift terms accompanying chemical loss processes. The *F* layer can have a substructure, dividing it into the  $F_1$  ledge and the  $F_2$  layer. In the dark ionosphere of winter nights this division of the *F* layer is not observed due to lack of solar ionization. The  $F_1$  layer vanishes and merges with the higher layer, forming a single

broad  $F_2$  region. Located around 250 km or above is the overall ionospheric density peak, typically one or several orders of magnitude larger than the  $E$  layer maximum densities.

The vertical profile of the electron distribution varies according to time of day, season, solar cycle, and sporadic processes responsible for ionization. Figure 2.1 shows altitude profiles for an equilibrium ionosphere under the conditions of high and low sun spot activity, as calculated by the International Reference Ionosphere model IRI-95 [Bilitza, 1995] for Poker Flat, Alaska, during the solstices in 1996 and 2000. To the left are the profiles for summer; winter conditions are to the right. The large variability between 100 - 200 km in the curves is due to the dominating effect of solar illumination during the day and prevalence of loss processes in dark periods. Long recombination and diffusion times at  $F$  region altitudes tend to diminish the diurnal cycle. The pronounced enhancement of the  $F$  region electron density in the winter season is likely due to the peak of the solar activity falling right around this time. The maximum sunspot number is expected to occur in the winter 2000/2001.

It is worth noting that these are equilibrium curves, whereas the ionosphere, particularly at high latitudes, at no time finds itself in a state of equilibrium. Even under quiet conditions, disturbances happen at shorter temporal scales than relaxation times, especially at higher altitudes. The actual density distribution at any given time may differ significantly from these statistical profiles. In their study, *Roble and Rees* [1977] modeled electron densities as a function of height for various electron energy spectra. They found that significantly altered density profiles occur several seconds after the onset of typical auroral fluxes ( $\sim 10^9 \text{ cm}^{-2} \text{ s}^{-1}$ ) with medium ( $\simeq 1 \text{ keV}$ ) and high ( $> 1 \text{ keV}$ ) energies, representing a strong aurora-induced sporadic  $E$  layer. For persistent energetic precipitation, an inversion can take place after a few tens of seconds, the overall density maximum can be temporarily found then in the  $E$  rather than in the  $F$  region. With fast losses through recombination and diffusion, decay phases have similar time scales. This is confirmed by electron density measurements by incoherent scatter radars, such as the Chatanika radar [Vickrey *et al.*, 1980] and the EISCAT facilities in Scandinavia (online data under <http://www.eiscat.uib.no>). EISCAT measurements show values up to the order of  $10^6 \text{ cm}^{-3}$  at  $E$  region altitudes during substorms, exceeding  $F_2$  peak densities. Concentrations around  $10^5 \text{ cm}^{-3}$  occur on a regular basis during perturbed nighttime auroral conditions, lasting for several minutes or more.

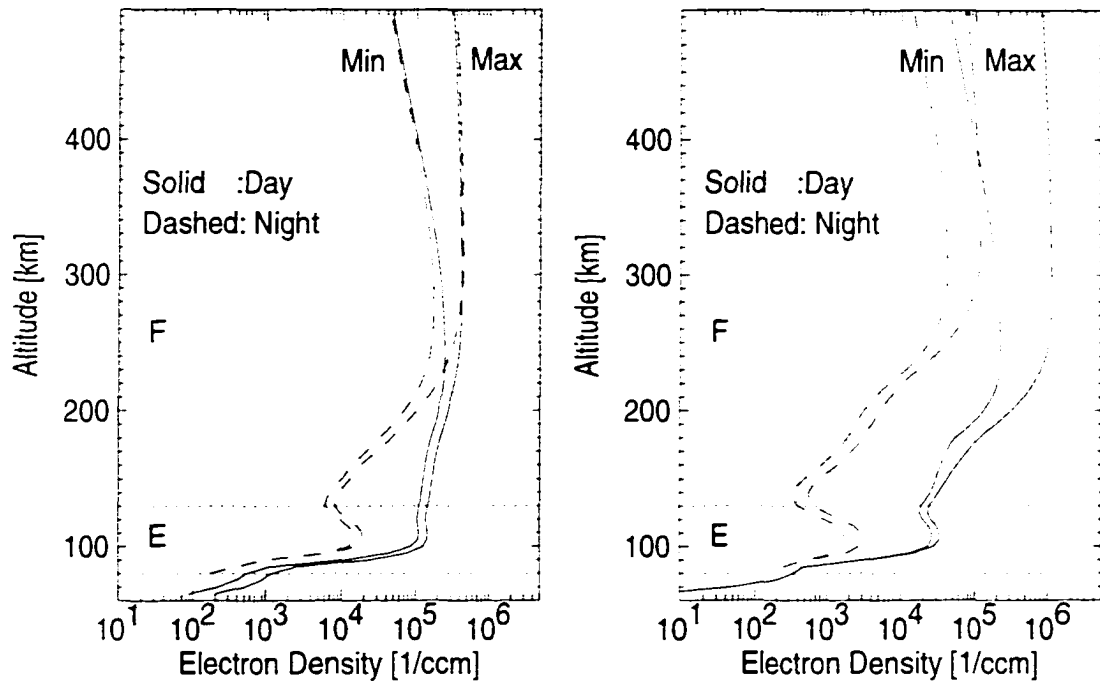


Figure 2.1. Electron density profiles at auroral latitudes for summer (left) and winter (right) days and nights under solar minimum and maximum conditions (IRI-95).

As shown in figure 2.1, maximum unperturbed densities in the  $F_2$  ( $E$ ) layer are on the order of  $5 \times 10^1 - 10^5 \text{ cm}^{-3}$  ( $5 \times 10^3 \text{ cm}^{-3}$ ) in the dark ionosphere at high latitudes around winter solstice 2000.

## 2.4 Irregularity Occurrence

There are two main global zones of maximum irregularity occurrences at  $F$  layer altitudes. One is found near the nighttime magnetic equator where the field configuration, with a large horizontal component of the magnetic field, together with the omnipresent vertical density gradient favor their generation (see section 2.5.3). The other region is at high latitudes under the influence of coupling between the ionosphere and the magnetosphere along magnetic field lines. The latitudes in between show a remarkable decrease in occurrence and magnitude of

irregularities. This is due to the stabilizing effect of increasingly higher dip angles (which implies that conducting field lines are increasingly parallel to the vertical density gradient) closer to the magnetic poles, relatively weak electric fields, and lack of the large-scale density perturbations characteristic of the high-latitude ionosphere. Statistical occurrence patterns of irregularities have been gathered by means of scintillation measurements and HF radars. Scintillation records show a distinct step in the irregularity pattern around the equatorward edge of the high-latitude convection pattern with elevated values at the poleward side, see figure 2.2.

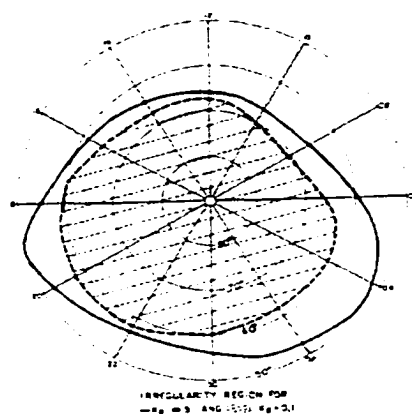


Figure 2.2. Statistical scintillation boundaries of  $F$  layer irregularities under more disturbed (solid line) and less disturbed (dashed region) geomagnetic conditions [Aarons, 1973].

The latitudinal location of the boundary varies with geomagnetic activity, with a position at higher latitudes during more quiet conditions. The irregularity intensity within the large contiguous polar area has distinct statistical enhancements and generally lower levels in the polar cap region. A maximum is found around magnetic premidnight to midnight at auroral latitudes. Progressing poleward the irregularity intensity decreases slightly throughout the polar cap, with a second, lower maximum somewhere between  $80^\circ$  geomagnetic latitude and the geomagnetic pole [Frihagen, 1971; Aarons, 1973]. On the dayside, the occurrence boundary is shifted slightly further poleward, corresponding to the latitude of the intersection of the magnetospheric boundary layer with the ionosphere.

In agreement with the irregularity detection by scintillation studies, two irregularity “curtains” could be identified with the help of a swept-frequency HF radar, see figure 2.3. The curtains describe a sharp increase in irregularities, as seen by the radar, which is situated equatorward of the curtain, scanning poleward. The curtains are approximately circular around the pole, aligned along regions of constant magnetic latitude with the irregularity center slightly offset from the magnetic pole towards the nightside and asymmetric around midnight [Möller, 1974]. The equatorward curtain is situated close to the equatorward diffuse auroral boundary with the most intense irregularities in the premidnight sector. After magnetic midnight, the irregularity pattern tends to weaken [Clark and Raitt, 1976]. Ruohoniemi and Greenwald [1997] come to a similar conclusion with respect to the irregularity locations. In their compilation of 5.5 years of HF backscatter records during solar maximum conditions, they find latitudinally wider regions of backscatter and increased probabilities of receiving scatter on the nightside versus dayside.

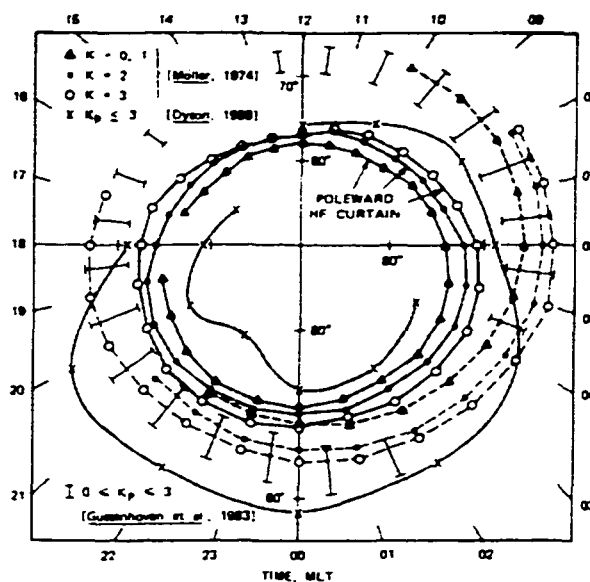


Figure 2.3. Morphology of two HF backscatter curtains for three (local) geomagnetic disturbance levels [Möller, 1974] and comparison with morphologies of the equatorward diffuse auroral boundary [Gussenhoven et al., 1983] and *in situ* irregularity [Dyson, 1969]. (From Tsunoda [1988].)



Primary generation mechanisms for the irregularities include single and combined effects due to solar UV irradiance, particle precipitation and auroral currents, the motion of the neutral atmosphere, plasma instabilities, and electric fields. The various processes will be discussed in detail in the following sections.

## 2.5 Source Regions and Irregularity Production

Structures in the plasma density can be caused by either the introduction of extra ionization in limited regions or by spatially rearranging existing plasma. The source mechanisms described in the first two sections below belong to the former group, the remainder of the processes to the latter. In both cases, developing irregularities can be the source for other irregularities with smaller scale sizes. In the presence of low background values, gradients in plasma density are often considerably large. Irregularities have been found to be L-shell aligned sheet-like structures [Rino *et al.*, 1978] with vertical electron density gradients being weaker than horizontal gradients [Vickrey *et al.*, 1980]. In particular, large structures may extend high up into the magnetosphere. The term “size” or “wavelength” of an irregularity reflects therefore always the spatial extension in a plane perpendicular to the magnetic field. Transverse irregularity sizes  $\lambda$  will be termed “large” ( $\lambda > 10$  km), “intermediate” ( $\lambda \approx 1$  km), and “small” ( $\lambda < 1$  km). Plasma instabilities can be effective at the walls of the large-scale features and produce smaller-scale structures. *In situ* rocket observations of the wide range of irregularity sizes occurring simultaneously indicate a close relationship of processes generating smaller structure [Kelley *et al.*, 1980, 1982].

### 2.5.1 Convection of Subsolar Plasma

The absorption of solar UV flux in the neutral atmosphere and the resulting ionization enhances plasma densities at altitudes above 80 km all across the dayside substantially and quite homogeneously. Plasma density increase with the incident solar angle and the duration of the solar illumination. Rapid loss processes in the *E* region and below reduce elevated concentrations within half an hour after sunset to night levels. Due to low atmospheric densities in the *F* layer recombination is slow. Lifetimes of enhanced ionization regions can therefore exceed many hours.

Transport of subsolar plasma with enhanced densities poleward into the low density polar cap is a precursor for large density structures at polar latitudes in the northern winter [Anderson *et al.*, 1988]. During the summer, when the polar regions are constantly illuminated in the northern hemisphere, background densities are too high to permit appreciable density gradients. There are several mechanisms under which dayside plasma can enter the polar cap. It has been proposed, that for a rapidly expanding polar cap the convection channels expand equatorward, thus encompassing sunlit plasma regions, and transporting them into the polar cap [Anderson *et al.*, 1988; Idenden *et al.*, 1997]. On occasions precipitation on dayside high latitudes was found to coincide with the observed density enhancements [Rodger *et al.*, 1994].

The volume with enhanced plasma densities enters the dayside polar cap, forming a the “tongue of ionization” there. Occasionally it can detach from the dayside high latitudes. Variations in the orientation of the interplanetary magnetic field (IMF) have been shown to govern the formation of polar cap patches through time varying convection [Sojka *et al.*, 1993]. The polar cap patches  $\mathbf{E} \times \mathbf{B}$  drift with the ambient plasma antisunward. They have been studied with a variety of ground-based instruments [e.g., Kersley *et al.*, 1995; McEwen and Harris, 1996; James and MacDougall, 1997; Pedersen *et al.*, 1998]. These patches represent the largest-scale irregularities found, with sizes of several hundred kilometers of up to 1000 km. Until their decay to plasma with background densities, they are themselves sources for smaller-scale irregularities [Kersley *et al.*, 1995; Sojka *et al.*, 1998].

### 2.5.2 Particle Precipitation

At high latitudes, at all local times, downward fluxes of electrons and protons are responsible for locally developing plasma enhancements in the ionosphere. The precipitating particles collide with and ionize the ambient atmosphere, thus creating a secondary electron population at about the same spatial sizes, but with a lower energy range. These secondaries are the main factor in the density build-up in precipitation regions. The typical energy of precipitating electrons ranges from 200 eV to 50 keV depending on source region and energization mechanism [Rees, 1988]. With an average loss of 35 eV per collision to the ambient plasma through ionization and energization, the number of created secondaries is

proportional to the energy level in the incoming primaries and in general several orders of magnitude larger than the number density of the primaries [Rees, 1988].

The altitude where the primaries are effectively stopped, i.e. where they blend in with the local thermal population after a sufficient number of collisions, depends on their initial energies. Higher particle energies imply lower impact parameter, thereby decreasing the collisional cross sections. On the other hand, increasing atmospheric densities at greater depths along the electron path eventually offset small the cross sections and consequently enlarge the collision frequency. Maximum values of ionization rates for higher energies are thus found at increasingly lower altitudes. The bulk part of the incoming energies in a precipitation event is deposited within the last 10 km before the kinetic energy is entirely converted to thermal energy [Rees, 1988]. Primaries with energies between 100 eV and 1 keV deposit most of their energy in the *F* layer, while 100 keV electrons reach down to the border area between *E* and *D* region [Rees, 1963]. Soft, diffuse precipitation on the order of a few hundred eV is an important source of *F* region irregularities with large scale sizes ( $>10$  km) [e.g., Kelley *et al.*, 1982; Basu *et al.*, 1983].

Numerous *in situ* studies have found evidence for the correlation of soft particle flux and the appearance of irregularities in the auroral *F* region. Among the examples are correlated studies with ground-based and satellite data [e.g., Dyson and Winningham, 1974; Basu *et al.*, 1983], and rocket measurements [e.g., Kelley *et al.*, 1980, 1982]. Being field-aligned, these large-scale structures contain relatively steep edges at the poleward and the equatorward side. They extend up to many hundred kilometers along the magnetic field. The majority of them is located in the magnetic evening/midnight sector, corresponding to the location of and the intensifications in the mean auroral oval [e.g., Clark and Raitt, 1976; Ruohoniemi and Greenwald, 1997]. Longitudinal resolution reveals sheet-like irregularities, in close association with the east-west aligned auroral electrojet [Rino *et al.*, 1983]. Density enhancements occur in the range of a factor of 2 - 10 over background values prior to the onset of soft particle flux [Vickrey *et al.*, 1980]. Kelley *et al.* [1980] described electron fluctuations of several times  $10^3$  cm<sup>-3</sup> during the expansion phase of an auroral substorm, with a vertical layer thickness of several hundred kilometers. Roble and Rees [1977] computed the time span between the onset of auroral activity in a particular region and the density enhancement to be several minutes. Observations however indicate time scales of one minute

[Kelley *et al.*, 1980] or even less [Tsunoda, 1988]. An example of a locally produced density structure was reported by Basu *et al.* [1983], who watched the “birth” of a kilometer-sized irregularity. In a coordinated studies including satellite measurements, they found large particle fluxes of low-energy electrons coincident with scintillation records. The appearance of the irregularity came within 1 - 2 minutes of onset of the precipitation-induced large-scale density buildup.

Precipitation-induced density structures are found experimentally by incoherent scatter radar measurements with varying scale sizes [Vickrey *et al.*, 1980; Kelley *et al.*, 1982]. An example of such a measurement is presented in figure 2.4. It shows the density variation with altitude, latitude, and time in the two consecutive scans. Scan durations are 13 minutes each. With diffusion across the magnetic field being slow in the *F* region, the investigated structures are therefore likely to be attributed to the spatial variation in precipitation.

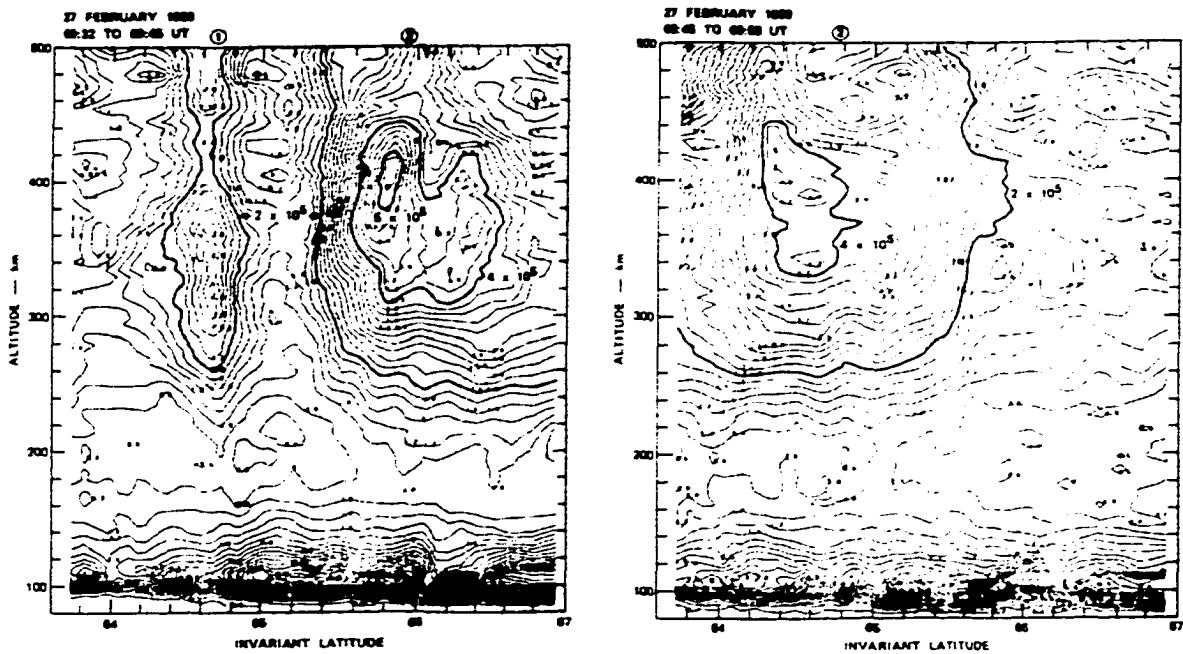


Figure 2.4. Nighttime electron densities as a function of altitude and invariant latitude. Two consecutive 13-minutes scans made by the Chatanika radar, Alaska, start times 9:32 UT and 9:45 UT. The contour interval is  $2 \times 10^4 \text{ cm}^{-3}$ . (From Vickrey *et al.* [1980].)

Highly energetic precipitation might also be associated with enhanced electron density blobs at  $F$  layer heights. These electron distributions are called “inverted-V” population, due to the spatial variation of their energy spectrum. The most energetic and therefore fastest electrons in the keV or many keV range form the middle part of the “V”. The flanks, covering latitudinal widths of up to  $2^\circ$ , consist of slower electrons, with a few hundred eV at the lower end of the energy range. The higher-energy electrons penetrate deeper into the ionosphere to  $E$  region altitudes. Less energetic electrons ionize at greater heights, thus creating a corresponding “V” shaped image with enhanced plasma densities in the ionosphere. Due to the large losses in the high-conductivity  $E$  region, the bottom part of that image vanishes rapidly. One or two ionization blobs are left at  $F$  region heights. The plasma density contour pattern spreads hereby outward latitudinally with increasing altitude around an auroral arc. In studies involving incoherent radar data, *Rino et al.* [1983] identified plasma structures attributable to both source mechanisms simultaneously: Near the equatorward boundary of the auroral oval they found evidence of latitudinally elongated large patches. These were identified to be caused by latitudinally localized precipitation of low-energy electrons from the inner edge of the central plasma sheet. Further poleward smaller blobs existed, the likely remainder of inverted-V auroral events. Correlating ground and satellite based observations, *Muldrew and Vickrey* [1982] also explained their measurements of  $F$  region irregularities with the upper legs of keV precipitation. They reported a density enhancement of about 15% in the observed case.

### 2.5.3 Plasma Instabilities

Patches of all sizes, generated by mechanisms described above are themselves sources for smaller-scale irregularities. They can provide large-scale density gradients on which a set of plasma instabilities operates to produce intermediate and small-scale irregularities. The free energy provided for the growth of instabilities comes from the presence of gradients, plasma drifts, motion of the neutral atmosphere, or currents. Small perturbations at the boundary between regions with the different properties in an unstable environment lead to larger turbulences, thus creating smaller-scale irregularities.

The growth rate or its inverse, the growth time, serves as an estimate of the effectiveness of an instability producing wave modes with growing amplitude in a specific environment.

It describes the linear growth phase of an instability. The time required until the actual appearance of smaller-scale irregularities has been determined from numerical simulations. This time depends, among others, on the wavelength, and is larger than the growth time of larger sizes [e.g., *Mitchel et al.*, 1985; *Huba et al.*, 1988]. Values found analytically can vary considerably, depending on input parameter and coupling mechanisms embedded in the assumption. Typical ionospheric values in most theoretical treatments of the  $F$  region imply a transverse electric field of 10 mV/m, an Earth magnetic field with 0.5 Gauss, field-aligned current of  $1 \mu\text{A}/\text{m}^2$ , and an electron density of  $10^5 \text{ cm}^{-3}$ .

### $\mathbf{E} \times \mathbf{B}$ Gradient Drift Instability

This mechanism is taken to be the primary driver for long wavelength (3-100 km) diffuse auroral  $F$  region plasma enhancements [cf., *Keskinen and Ossakow*, 1982; *Cerisier et al.*, 1985; *Sojka et al.*, 1998]. It arises in the presence of plasma density gradients in an environment with perpendicular electric and magnetic fields. Figure 2.5 shows the geometry involved, with a view upwards along the field lines into the region of interest.

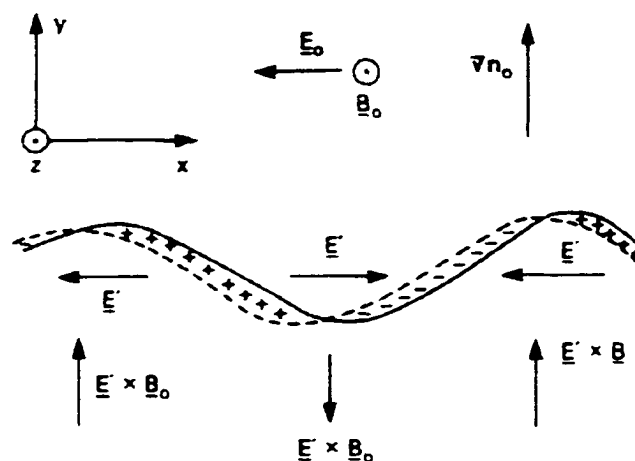


Figure 2.5. Geometry of the  $\mathbf{E}' \times \mathbf{B}$  gradient drift instability (see text for details).

The ambient magnetic field  $\mathbf{B}_0$  is directed out of the plane, the background electric field  $\mathbf{E}_0$  points towards left, i.e. east for the northern high latitudes, while the prevailing

density gradient  $\nabla n_0$  is directed upwards (northward). Ions and electrons Pedersen-drift in a plane transverse to the magnetic field, with a larger ion displacement due to their larger displacement between collisions. A small sinusoidal perturbation perpendicular to  $\mathbf{E}_0$  at the boundary sets up positive and negative space charges, which in turn give rise to small-scale electric fields  $\mathbf{E}'$  in alternating directions. The corresponding  $\mathbf{E}' \times \mathbf{B}$  drift carries the enhanced density areas downward (southward), relative to the background  $\mathbf{E} \times \mathbf{B}$  drift, and the depleted regions upward (northward), thus increasing the amplitude of the perturbation. The stability of such a configuration depends clearly on the relative orientation of density gradient and background electric field. Changing the sign of one of the two quantities reverses the trend and stabilizes the initial perturbation. Enhanced perturbed regions then fall back into the high-density volume. For a typical case during active times at the nightside of the Earth, with an ambient eastward electric field and an auroral arc representing an enhanced density region with inward pointing density gradients, the poleward side of the arc is stable to small perturbations, while perturbation amplitudes at the equatorward side tend to grow.

The same effect of a growing instability is achieved if, instead of the presence of an ambient field  $\mathbf{E}_0$ , a neutral wind is blowing antiparallel to an electron density gradient. In the rest frame of the neutral atmosphere this implies an electric field perpendicular to the density gradient on the borders of the enhancement. Because of the current continuity, regions with enhanced plasma densities (higher conductivities) have lower electric fields and  $\mathbf{E} \times \mathbf{B}$  drift slower than the ambient plasma. Therefore, the front end of the enhanced density region drifts slower than the background plasma and falling back into the high-density volume. That difference in velocities leads to the density enhancements falling into the ambient low plasma at the back side of the arc, an unstable situation [*Temerin and Kintner, 1989*]. Reversing the gradient vector or the relative motion of the two frames of reference results in a stable configuration. Differences in drift velocities of neutral and the charged population (i.e. slip velocity) are small in the auroral zone, but might occur in sharp reversal zones such as the equatorward convection boundary or the Harang discontinuity [e.g., review by *Tsunoda, 1988*].

In the night sector, poleward of the equatorward boundary of the auroral oval, plasma structures usually convect equatorward. The drift vector together with the sign of the

density gradient renders the poleward wall unstable [Keskinen and Ossakow, 1982]. Using observed ionospheric quantities, Vickrey *et al.* [1980] calculate growth times of 50-250 s for decameter sized irregularities. The largest growth rates are found on the poleward site of the convecting enhancements. Keskinen and Ossakow [1982] indicate growth times of 100 seconds. Hereby originally latitudinally confined enhancements break up into striation-like structures, elongated in the north-south direction. The formation and cascading from large ( $\simeq 100$  km) to smaller ( $\simeq 3$  km) scale sizes takes place on the order of an hour. Shorter time scales, i.e. half an hour, are found in the break down of kilometer-sized structures to tens of meter scale sizes [Keskinen and Ossakow, 1983a]. These times comprise the entire transfer from one wavelength regime to the smaller one. The first appearance of smaller structures happens well before that.

### Current Convective Instability

In stable geometries which are similar to those evoking the  $\mathbf{E} \times \mathbf{B}$  instability described above, but with one of the components pointing in a stabilizing direction, the presence of field-aligned currents can overturn the stability condition. The resulting instability is called the current convective instability [Ossakow and Chaturvedi, 1979]. For already unstable configurations the presence of field-aligned currents can increase growth rates [Vickrey *et al.*, 1980; Keskinen and Ossakow, 1982]. The combined effects of the current convective instability and the  $\mathbf{E} \times \mathbf{B}$  instability are termed "generalized  $\mathbf{E} \times \mathbf{B}$  instability."

Evidence of this instability has been found experimentally by studies combining ground based and *in situ* measurements. Vickrey *et al.* [1980] showed in satellite and incoherent scatter radar data, that the current convective instability likely acted on the poleward density gradient of equatorward drifting large-scale irregularities on the night sector, while the existence of intermediate-sized plasma structure was verified simultaneously by scintillation measurements. In a comparison of scintillation and *in situ* particle measurements Basu *et al.* [1983] similarly depicts a situation where a downward field-aligned current at the equatorward portion of the premidnight auroral oval likely destabilized an otherwise stable configuration.

The necessity of currents parallel to the magnetic field limits this instability to auroral regions, furthermore to regions of currents associated with diffuse particle precipitation



[*Ossakow and Chaturvedi*, 1979]. *Kelley et al.* [1982] pointed out that destabilizing currents have to be carried by a thermal population. The application of this instability theory for highly energetic current carriers has not been investigated. The dominance of either  $\mathbf{E} \times \mathbf{B}$  or current convective instability is favored by strong transverse  $\mathbf{E}$  fields, weak parallel currents, and low densities for the former instability and vice versa for the latter [*Keskinen and Ossakow*, 1983b]. Growth rates maximize for low ambient densities: below the  $F_2$  peak the current convective instability may therefore be more effective than the  $\mathbf{E} \times \mathbf{B}$  instability. The fastest linear growth times for long-wavelength irregularities in a typical diffuse auroral  $F$  region environment were found in two theoretical studies by *Keskinen and Ossakow* [1982] and *Ossakow and Chaturvedi* [1979] to be about 100 seconds and 5-6 minutes, respectively. But this instability also acts on smaller irregular structure, with comparable growth times of 100 seconds [*Keskinen and Ossakow*, 1983a]. In a case study *Vickrey et al.* [1980] found an experimental value of  $\leq 6$  minutes for the generation of wavelengths  $\geq 10$  km from larger sizes.

The current intensity is a determining factor in the generation of this instability. Larger field-aligned currents will accelerate growth rates. Too large currents (drift velocities  $\geq 1$  km/s), however, excite the collisional electrostatic ion cyclotron instability rather than the current convective instability [*Chaturvedi*, 1976]. Typical parallel current intensities of  $1 \mu\text{A}/\text{m}^2$  in the diffuse  $F$  region, with drift velocities around 60 m/s, are well below that threshold. Other effects might also be active in the generalized  $\mathbf{E} \times \mathbf{B}$  instability. Modifications include magnetic shear [*Huba and Ossakow*, 1980] and ion inertial and collisional implications [*Chaturvedi and Ossakow*, 1981].

#### 2.5.4 Electrostatic Turbulence

Horizontal ionospheric electric fields act to impose structure on ionospheric plasma. Turbulent isotropic vector electric fields have been shown to vary latitudinally in regions corresponding to the statistical auroral oval. *Kelley and Mozer* [1972] reported static fields fluctuating over a broad frequency range and concluded an intimate relationship between ionospheric turbulences and electric field variations in the plasma. A possible explanation has been invoked as oscillations occurring independently on adjacent field lines. This occurs when Alfvén waves on adjacent L-shells resonate with slightly different frequency [*Lyatsky*

*et al.*, 1999]. Turbulent electric fields occur also in the polar cap, especially during extended periods of a northward component of the interplanetary magnetic field and during winter [Heppner, 1977]. Kelley and Kintner [1978] hypothesize that highly structured electric fields on the dayside, presumably originating in the magnetosphere, could be responsible for ionospheric density enhancements at the same scale sizes. Enhanced electric fields in the vicinity of auroral arcs have been repeatedly observed. During precipitation events the electron precipitation in the upward going field-aligned currents results in converging electric fields and inward Pedersen currents [Marklund *et al.*, 1998]. The electric field within auroral structures is typically markedly reduced, due to the accompanying higher conductivity. The field intensifications are found to occur at the arc edges or in between bright auroral fine structures. Values near auroral forms are of the order of tens to hundreds mV/m [Lanchester *et al.*, 1996], in auroral forms less than 10 mV/m, compared to quiet time values of the order of few mV/m [Marklund *et al.*, 1998].

Ion cyclotron waves, electrostatic waves due to ion sound waves in a magnetic environment, are among the sources for electric field variations. The energy for exciting the ion cyclotron instability is drawn from differences in the velocity between electrons and ions or within the ion population. Strong field-aligned currents have been found to excite ion cyclotron waves roughly transverse to the magnetic field through the dissipative effects of electron-neutral collisions [cf. review by Kelley, 1989]. The threshold parallel current density is generally higher than typical field-aligned current densities, but not higher than the largest values observed. In the *F* region the threshold is around several tens of  $\mu\text{A}/\text{m}^2$  [Satyanarayana and Chaturvedi, 1985]. Resulting irregularities have scale sizes which depend on the excitation process and ionospheric parameters. [Lakhina and Bhatia, 1984] calculated scale sizes in the range 3 - 15 meter, due to instabilities arising in a non-equilibrium ion velocity distribution. Relative drifts between electrons and ions of a few kilometers per second in field-aligned currents lead to long-wavelength ion cyclotron waves and irregularities in ranges of hundreds of meters [Chaturvedi, 1976]. Growth times vary with the number density of resonating ions, but are generally below one minute [Lakhina and Bhatia, 1984].

On the nightside, electrostatic waves have been found to occur in the vicinity of auroral arcs. During a rocket flight through an auroral arc Kelley and Carlson [1977] detected intense (10 mV/m) ion cyclotron wave emissions at the edges of the arc. Electrostatic waves

near auroral arcs are also reported from measurements in the *E* region [*de la Beaujardière et al.*, 1977]. The magnetosphere as a possible source for irregular electric fields mapped down along field lines has been discussed by *Maynard et al.* [1982] and *Vickrey et al.* [1982].

The scope of the impact of electric fields on the ambient plasma varies with the dimension. Small-scale structure in the electric field can produce a structured plasma density at the same sizes. On large scales, spatial as well as temporal, large electric fields both accelerate ions relative to neutral components and increase the ion temperature because of the associated enhanced Joule heating. Both mechanisms increase the low reaction rate of  $O^-$  with  $N_2$ , the dominant ion species at *F* region heights, therefore increasing the relative occurrence of  $NO^+$ . The  $NO^+$  recombination rate is large compared to the recombination of  $O^-$ , thus possibly creating local depletion zones. With the Chatanika radar, *Kelly and Wickwar* [1981] found phenomena consistent with this explanation for electric fields  $E \geq 40$  mV/m.

### Velocity Shear

Different velocities in regimes of adjoining plasma domains constitute a free energy source for the growth of plasma instabilities. Velocity shear has been suggested to play an important role in the generation of ionospheric irregularities [*Kintner*, 1976; *Kelley et al.*, 1976; *Basu et al.*, 1988]. This instability occurs for a irregularity in the velocity space instead of or in addition to anomalies in density. Several modes with different wavelengths can hereby be excited. Perturbations with several kilometer minimum sizes are likely due to the Kelvin-Helmholtz instability [*Perkins and Jassby*, 1971; *Keskinen et al.*, 1988]. *Hallinan* [1976] sees this mechanism active in the curling up of auroral forms.

Other velocity shear driven waves form at smaller wavelengths, as was discussed by *Perkins and Jassby* [1971]. An instability of the latter type, the shear driven resistive drift wave, was believed to be active due to strong horizontal velocity shears with extremes up to  $20 \text{ (m/s)} \times \text{m}^{-1}$  which were found across an auroral arc [*Kelley and Carlson*, 1977]. The authors detected simultaneous irregularities in the meter range, likely causally related to the shears with scale sizes of up to a few hundred meters, and deduced a minimum growth time of 2.5 s. In their review of *F* region instabilities *Fejer and Kelley* [1980] pointed out, that this type of instability can explain some short wavelength structures at the edges of auroral

arcs. *Keskinen and Huba* [1983] reported that shear in field-aligned electron velocities in the vicinity of intense discrete auroral arcs might be unstable and lead to centimeter- and meter-scaled irregularities. Anisotropic plasma velocities have also been cited as a possible factor in the generation of meter-scale irregularities [*Keskinen and Ossakow*, 1983b].

### Other Mechanisms

*Hudson and Kelley* [1976] showed that plasma anomalies in the range of hundreds of meters can be explained by parallel density and temperature gradients generating electrostatic turbulences in a plane perpendicular to the magnetic field. Depending on the plasma density and the density gradient scale length  $L$  certain modes are expected to be excited and dominate in various regimes given by  $\rho_i/L < (m_e/m_i)^{1/2}$ : universal drift mode,  $(m_e/m_i)^{1/2} < \rho_i/L < (m_e/m_i)^{1/4}$ : drift cyclotron mode, and  $(m_e/m_i)^{1/4} < \rho_i/L$ : lower hybrid drift mode, where  $\rho_i$  is the ion Larmor radius and  $m_e$  and  $m_i$  are electron and ion mass respectively [*Mikhailovskii*, 1974]. Highest growth rates are found for  $L$  close to the electron or ion Larmor radius. While the former is well below the meter size, the ion gyroradius for soft particles has a value of around 10 m in the auroral  $F$  region. *Vickrey and Kelley* [1982] argued for the importance of universal drift waves for the irregularity generation between the wavelength range around 100 m to smaller scales. Gravity waves with transverse wavelengths of several hundred kilometers also create corresponding structure at ionospheric heights, detectable by HF radars [e.g., *Samson et al.*, 1989; *Bristow et al.*, 1994].

## 2.6 Transport and Lifetime

The large polar cap patches which form under the influence of dayside ionization and IMF configuration in the polar cap (cf. section 2.5.1) drift antisunward across the polar cap, following the convection pattern. As they arrive at auroral latitudes at the night side, the patches convect towards the boundary between open and closed magnetic field lines. Here they are forced to reconfigure in a confined latitudinal region and spread out along longitudes [*Robinson et al.*, 1985]. The omnipresent nature of irregularities, presumably arising from polar cap patches, led some researchers to speculate that the irregularity enhancement in

the Harang discontinuity is due to the solar patches drifting out of the polar cap rather than local production [e.g. review by *Tsunoda*, 1988].

On the nightside, large-scale irregularities are also formed locally due to soft particle precipitation. They convect throughout the entire nightside on narrow paths (100 km) of constant invariant latitude spread over almost 12 hours of longitude [*Kelley et al.*, 1982; *Tsunoda*, 1988]. All through their existence the irregularities are subject to cross-field diffusion and recombination. However, recombination in the *F* region is slow, due to small recombination rates for the major *F* region ion  $O^+$  [*Rees*, 1988]. Instabilities act on the walls of big patches, generating smaller ionization blobs, which can be found in their trailing edge [*Pedersen et al.*, 1998].

Neglecting collisional effects, *Vickrey and Kelley* [1982] calculated the lifetime under the influence of classical cross-field diffusion. Effective decay times for large ( $> 10$  km) irregularities in the dark ionosphere are of the order of several hours, and up to a day. The lifetimes were found to be unaffected by anomalous diffusion [*Kelley et al.*, 1982]. This time is large enough for the irregularities to survive cross-polar transport and redistribution in the nightside auroral zone [*Kelley et al.*, 1982]. Therefore, large-size irregularities can be found in the whole polar region, independent from the source region.

Intermediate and smaller structures ( $\leq 1$  km) have increasingly shorter decay times. Irregularity lifetimes are proportional to  $(\lambda^2 \times D_{\perp})^{-1}$ , where  $\lambda$  is the irregularity wavelength, and  $D_{\perp}$  the perpendicular diffusion coefficient [*Basu et al.*, 1998]. Typical values for  $D_{\perp}$  are on the order of  $1 \text{ m}^2/\text{s}$ . Density anomalies with scale sizes from 100 m to 1 km were found to have lifetimes of minutes to hours respectively [*Vickrey and Kelley*, 1982; *Basu et al.*, 1998]. According to the mechanism of cross-field diffusion only, structures of 100 m size are limited to a region within a few degrees of their production zone [*Kelley et al.*, 1982]. *Vickrey and Kelley* [1982] argue that diffusion processes at these scale lengths are fast enough so that only very few irregularities should indeed exist at any time. Meterscale irregularities on the other hand dissipate on a time scale of seconds [*Tsunoda*, 1988] and are therefore locally very confined. Since there is no doubt about the existence of irregularities on these scales, plasma instabilities operating on larger-scale irregularities must be involved to produce the observed spectrum of coexisting irregularities. Thus it has to be assumed that detected density enhancements in the meter range are not produced directly but through cascading

from longer wavelengths. The presence of small structures is therefore an indicator for the simultaneous presence of larger irregularities.

The extent of decay through plasma instabilities, although doubtlessly important, is hard to quantify since it depends on a variety of ionospheric and magnetospheric parameters. Analytical and numerical simulation techniques indicate decay times of kilometer-sized structures into smaller irregularities. Numerical simulations of the effects of the  $\mathbf{E} \times \mathbf{B}$  gradient drift instability by *Huba et al.* [1988] indicated fast decays of kilometer-sized structures into smaller irregularities. Instability growth times vary with inclusion of the magnetosphere in the model. Coupling of the high-latitude  $F$  layer with the collision-free magnetosphere through field-aligned electron flows tends to stabilize  $F$  region processes. In the example of a 40 km irregularity, including magnetospheric effects, the time for the complete rearrangement of the original size to a turbulent mixture of various but still large dimensions was of the order of 10 - 15 minutes. Results by *Keskinen and Ossakow* [1983a] show that this instability type can provoke cascades of smaller density anomalies, breaking down irregularities from kilometer to tens of meter scale sizes within one hour. As discussed above, time scales can be smaller by the inclusion of field-aligned currents in this scenario.

The downward coupling to the conducting  $E$  layer influences also the development of irregularities through electrodynamic along the magnetic field lines threading a common vertical region. By the supply of electrons on field-aligned flux tubes, and closing horizontal currents the  $E$  layer conductivity affects diffusion processes and the growth of instabilities in the  $F$  region. The overall effect of the coupling to a conductive  $E$  region are an increased diffusion rate, and therefore a retarded instability growth and shorter irregularity lifetimes. The extent of the retardation depends on the ratio between the Pedersen conductivities at  $E$  and  $F$  layer altitudes. *Tsunoda* [1988] calculated a reduction of irregularity growth rate by a factor of 50 or more for high Pedersen conductances in the auroral  $E$  layer.  $F$  region cross-field diffusion can be increased by an order of magnitude or more due to  $F$  and  $E$  region coupling [*Vickrey and Kelley*, 1982].

For low  $E$  region densities and irregularity sizes at or below the kilometer threshold, another mechanism gains importance. So-called "images" in the  $E$  region form after the pattern in the  $F$  layer. They result from the Pedersen motion in the  $F$  layer, diffusing away from the regions of high density. With less horizontal mobility of the electrons, a

polarization electric field is set up, retarding further ion diffusion. Coupled to the E layer below, electrons are free to move along field lines. They move downward in the regions of enhanced plasma density, where the diffusing ions left a larger electron cloud, and upward in the vicinity, where positive charges prevail. Horizontal ion motion in the E layer closes the circuit, thus enhancing plasma densities directly beneath the F region patch. This counteracts the field-aligned current which otherwise would hasten F region decay, thus slowing the diffusion rate at higher altitudes. Significant image formation already takes place after one minute after appearing in the F region [Jones and Sparklen, 1978]. With high recombination rates in the E layer, the necessary condition is a relatively low density, specified by Vickrey and Kelley [1982] with not more than a few times  $10^4 \text{ cm}^{-3}$ . The fast chemistry in the E region suppresses images at larger than kilometer scales.

## 2.7 Detection Methods

Plasma density irregularities are most commonly probed remotely by their impact upon electromagnetic radiation passing the irregularity volume. Statistical and event studies have established a relationship between irregularity occurrence in the two most prominent techniques: scintillation measurements, and HF radar backscatter [Möller and Tauriainen, 1975].

### 2.7.1 Coherent Scatter Radars

Coherent scatter radars take advantage of the coherent addition of electron scattering amplitudes at the boundary between media with different indices of refraction. A part of the power of the electromagnetic wave incident normally on a sharp boundary will be reflected. The fraction of reflected power is given by  $(n_1 - n_2)^2 / (n_1 + n_2)^2$ , where  $n_1$  and  $n_2$  are the refractive indices of the media. The appropriate refractive index for any given configuration can be determined from the basic Appleton-Hartree equation [e.g., Davies, 1965]. Neglecting the presence of a magnetic field and collisions, it depends on the charge density via the plasma frequency  $f_p$  as

$$n = \sqrt{1 - \frac{f_p^2}{f_r^2}} \quad (2.1)$$

where  $f_r$  is the radar frequency. The plasma frequency is given as

$$f_p^2 = \frac{Ne^2}{\pi m} \quad (2.2)$$

with  $N$  being the electron density,  $e$  the electron charge, and  $m$  the electron mass, all quantities in cgs units. A numerical treatment of the Appleton-Hartree equation includes the presence of the Earth's magnetic field and collisions. Encountering layers of density fluctuations, the scattering repeats at every boundary. If the distance  $d$  between the layers with specific indices of refraction equals half the incident wavelength, the refracted waves interfere positively, according to

$$2d = \lambda_r / \cos(\alpha/2) \quad (2.3)$$

where  $\alpha$  is the angle to the layer normal, and  $\lambda_r$  the radar wavelength. See figure 2.6 for a schematic for the scattering from several layers. For the angle of incidence close enough to perpendicularity and sufficiently sharp inhomogeneities a major part of the compounded effect of the refraction is directed back to the radar. This is the Bragg law for the case of normal incidence ( $\alpha = 0^\circ$ ). Minimum observable fluctuation levels in the irregularities are of the order of at least few hundred  $\text{cm}^{-3}$  [Walker *et al.*, 1987]. Coherent radars operating in HF (3-30 MHz), VHF (30 - 300 MHz), or UHF (300 MHz - 3 GHz) frequencies, are therefore theoretically sensitive to density anomalies with scale sizes of 50 - 5 m, 5 - 0.5 m, and 0.5 - 0.05 m, respectively. At high latitudes, however, the requirement of orthogonal incidence to the field-aligned irregularities decreases the range of usable radar frequencies. The magnetic field in the vicinity of the magnetic poles has an increasingly large vertical component. For this reason radar beams have to be close to horizontal near the field-aligned density inhomogeneity. For probing the ionosphere at higher altitudes, this can only be achieved with the help of ionospheric refraction of the radar beam. Snell's law, here in its approximation for a flat Earth, determines the ray path according to the vertical density profile in the ionosphere:

$$n_1 \sin(\alpha_1) = n_2 \sin(\alpha_2) \quad (2.4)$$



where  $\alpha_1$  and  $\alpha_2$  are the incidence and the refracted angle respectively.  $n_1$  and  $n_2$  the indices of refraction in the adjacent layers. Indices of refraction in the ionosphere have typically values between 0.9 and 1. Higher densities result in a lower index of refraction, increasing the angle of the refracted wave. The vertical ionospheric gradient, overall positive upward to  $F$  layer altitudes, refracts the radar signal away from the layer normal, resulting in a curved path.

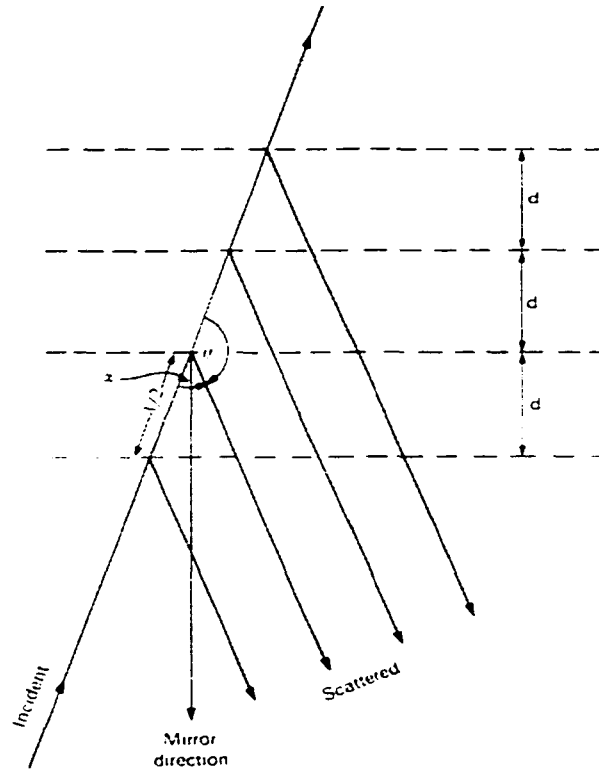


Figure 2.6. Volume scattering from layers with spatial periods  $d$  for a wavelength  $\lambda$ .

In a dispersive medium such as the ionosphere, the index of refraction is dependent on the wave frequency. Lower frequencies imply a prolonged reaction interval of the ambient plasma, and are therefore more strongly refracted. Frequencies higher than the HF band are prone to escape the top of the ionosphere. For transmission frequencies within the HF band the refraction can be sufficient to provide the desired orthogonality in the  $F$  region. The determining factor is the overall ionospheric density gradient. Peak  $F$  layer electron

densities higher than approximately  $10^5 \text{ cm}^{-3}$  are capable to sufficiently refract a 14.5 MHz radar beam, as calculated by [Walker *et al.*, 1987].

### 2.7.2 Scintillation

The scintillation observation techniques uses amplitude fluctuations due to rapid and irregular fading of radio signals from radio stars and satellite beacons. The fluctuations are caused by scatter or diffraction of the signals by irregularities in the Earth's ionosphere. The scintillation index is constructed from the scintillation amplitudes indicating the deviation from quiet times. The height range between 250 and 500 km has been established as the predominant region for scintillation-producing irregularities [Aarons, 1973]. If the radio signal passes through adjacent regions with different electron density, at higher latitudes always almost parallel to the magnetic field, it will encounter different indices of refraction on its path, with a resulting phase shift between the rays. This phase shift is a function of the difference in electron densities and integration path (i.e. the length of the irregularity along the ray path). It can be detected by appropriate antennas from Earth. Scintillation observations are performed in the range of few Hz to few hundred MHz, detecting irregularities with field-aligned dimensions of a few 100 meter to several kilometer, almost invariably located in the *F* region. As a necessary threshold it was found that the difference of electron densities in adjacent regions is required to be at least 10% [Frihagen and Jacobsen, 1971].

On the nightside of the Earth the regions with regularly enhanced scintillations levels are aligned along L shells and coincide with the diffuse auroral oval [Rino *et al.*, 1978]. Intense fluxes of low-energy electrons were found to be associated with large phase scintillations [Basu *et al.*, 1983]. In most of the cases, the scintillations are due to sheet-like *F* region irregularities. These irregularities occur in the vicinity of the equatorward boundary of plasma structure with enhanced density and a westward electric field component [Ossakow and Chaturvedi, 1979]. Although a geometry like this is stable to the  $\mathbf{E} \times \mathbf{B}$  instability, the presence of field parallel currents could outweigh the stabilizing effect of the ambient electric field. The scintillation technique is also used to detect irregularities in the polar cap [Kersley *et al.*, 1995].

### 2.7.3 Plasma Density Measurements

Instead of detecting irregularity footprints directly, measurements of the spatial development of plasma concentrations give information about structure in the plasma. The following instruments are suitable to reveal vertical or horizontal density profiles, indicating any presence of plasma structures.

#### Incoherent Scatter Radars

The principle of incoherent scatter is based on Thomson scattering of radio signals from free electrons. Particles accelerated by incident electromagnetic radiation emit radiation themselves. A small fraction of the emitted wave will be scattered back to the radar receiver. Given the small electron radius total radar cross sections for typical incoherent scatter sampling volumes are of the order of  $\text{mm}^2$  at *E* region altitudes [Hargreaves, 1992]. High transmitting powers and sensitive receivers are therefore necessary to detect the scattered signals. With every scatterer contributing to the total backscattered intensity, the power incident at the radar is a measure of the electron density in the probed volume. Strictly speaking, however, electrons are not independent particles if the probing wavelength is larger than the Debye wavelength. This is in fact the case for all radar wavelengths. For scale sizes larger than the Debye length the electron behaviour is controlled by ion motion. Scatter arises therefore from electron density fluctuations around longitudinal ion oscillations in the plasma. In addition to electron density the received frequency spectrum carries information about plasma Doppler velocities and electron and ion temperature and other derived quantities. An extensive and still valid overview over theory and practice of incoherent scatter radars has been given by Evans [1969].

Incoherent scatter radars are operated in the VHF band (30-300 MHz) and in the UHF band (300 MHz - 3 GHz) with wavelengths ranging from 10 m for lower VHF frequencies to 10 cm for the 3 GHz frequency. This type of radar is typically driven with pulsed radio transmission. The altitude of the target region is set by the choice of the time interval between transmitting and listening modes. Thus height profiles can be obtained in addition to horizontal scans with constant altitudes and different signal emission angles. Horizontal maps are useful for the observation of plasma irregularities, while rapid scans over limited

regions can detect temporal developments. An example of the use of incoherent scatter radars for the detection plasma structure is provided by *Kirkwood and Osepian [1995]*, who deduced information about energetic particle precipitation from the altitude profile of the electron density and its time variation.

### **Ionosondes**

Ionosondes transmit and receive radio waves sweeping over a range of frequencies, typically 0.5-10 MHz either as ground-based instruments (bottomside sounders) or above the  $F_2$  region density peak from above as payloads on spacecrafts (topside sounders). An ionosonde takes advantages of the fact that waves are reflected in the ionosphere, where their frequency is equal to or less than the local value of the plasma frequency. Sounding with varying emission frequencies creates therefore a vertical profile of the plasma frequency. The plasma frequency is closely related to the local plasma density via equation 2.2. The corresponding altitudes are calculated by the time a free-space electromagnetic wave travels twice the distance to the reflection point. Since the true speed is less than the assumed velocity, this "virtual height" is larger than the actual height. The real ionospheric density profile can then be regained by inverting a set of equations. The inversion depends upon the assumption of monotonic density distributions and results in ambiguities if there are downward gradients in the profile. Ionosondes are used for monitoring altitudinal changes of ionospheric layers profile modulations. Examples of scintillation-based work include morphology studies at auroral latitudes [*Basu and Aarons, 1980*] and in the polar cap [*Kersley et al., 1995*]

### **Other *in Situ* Instruments**

Several *in situ* instruments can be used to infer ionospheric densities. The measurements are often not direct, but indirect through the effect of an artificial electric field on plasma. Prominent members in this group of instruments are Langmuir probes, carried regularly aboard spacecraft and sounding rockets. They measure the current between two conducting elements at different electric potentials which are rapidly swept through a given range of potentials. With the current proportional to the charge concentration and the velocity of the current carriers, the total plasma density can be deduced. Instruments of this type are flown on rockets [e.g., *Narcisi and Bailey, 1965*] and satellites [e.g., *Krehbiel et al.,*

1981]. Electrostatic analyzers work after the same principle as a Langmuir probe with the difference that, as the name indicates, a fixed potential is used. Experiments with electrostatic analyzers on space vehicles were performed e.g. by *Sagalyn et al.* [1974] on ISIS-1.

## Chapter 3

# Instrumentation and Site Characteristics

This chapter introduces the instrumentation used for this thesis. In order to analyze the HF radar returns in the presence of optical aurora, locations and intensity of backscatter and auroral emissions were compared. This was done at two high-latitude locations: Alaska and Svalbard, Norway. Data were collected in the auroral seasons 1997/1998 to early 1999/2000 for Svalbard, and in early 2000 for Alaska. Indicators for optical aurora are mainly a meridian scanning photometer (MSP) and to a lesser degree an allsky camera (ASC).

In the first sections of this chapter the SuperDARN HF radar system is introduced, including an overview over the deduced variables and HF wave propagation. Subsequently the meridian scanning photometer is described, followed by the descriptions of the allsky camera.

### 3.1 SuperDARN HF Radar

The Super Dual Auroral Radar Network HF radars (figure 3.1) form an international array of HF coherent scatter radars. They are spread around different longitudes at high latitudes with a heavy weighting of the western and northern hemisphere. Currently there are eight radars operational at northern high latitudes, six in the Antarctic.

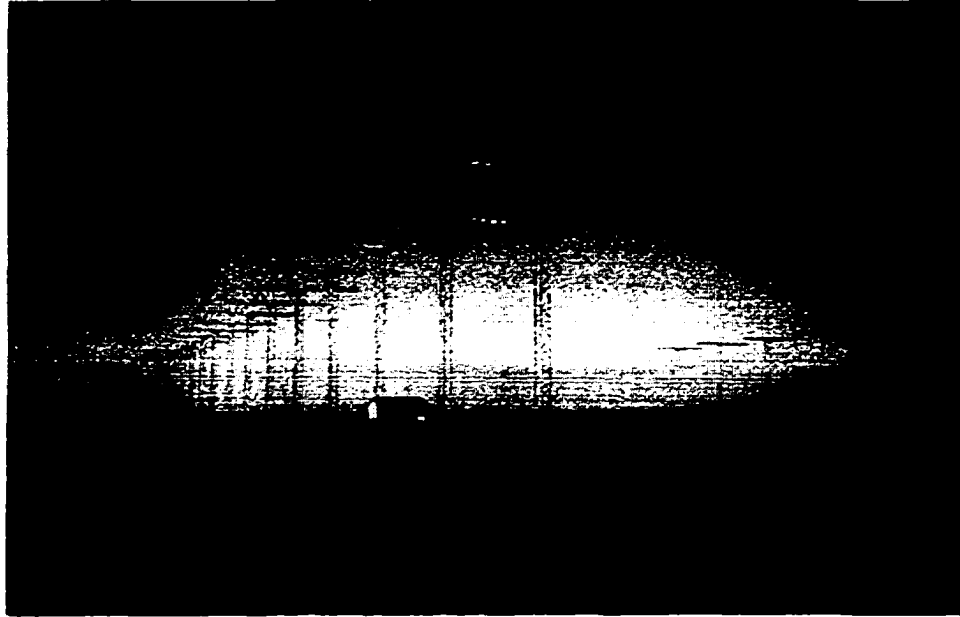


Figure 3.1. The antenna arrays of the SuperDARN HF radar at Pykkvibær, Iceland.

The operational frequency range of the radars is between 8-20 MHz. Typically employed frequencies of 10 - 14 MHz render the radar signal, according to the Bragg condition, sensitive to ionospheric irregularities with 11 - 15 m wavelength. The radar family is arranged in pairs, where two radars each overlook a common field-of-view from different look directions. This enables the derivation of a vector field. Based on the assumption of plasma flow being aligned along L-shells horizontal flow velocities could also be determined from single radar observations, albeit with a larger uncertainty [Ruohoniemi *et al.*, 1989]. Determination of flow patterns, in particular large-scale polar convection, and mesoscale convection in event studies, is one of the main SuperDARN applications.

Data from three different SuperDARN HF radars were used for the analysis. The newly commissioned radar at Kodiak (cgm 56.84° N, 95.58° W) provides coverage over large parts of Alaska. Only one radar of a pair could be used, since the complementing radar (at Prince George, Canada) was switched on at a later time and did not provide useful returns by the time and for the days the present data were taken. Over Svalbard, Norway, backscatter signals were investigated taken by the two Cooperative UK Twin Located Auroral Sounding

System (CUTLASS) radars, a SuperDARN subset. They are located in Pykkvibær (cgm 65.02° N, 68.57° E) . Iceland, and in Hankasalmi (cgm 56.36° N, 102.96° E), Finland.

### 3.1.1 Radar Specifications and Variables

The main antenna array of each radar following the SuperDARN standard consists of 16 log-periodic antennas enabling transmission over a range of frequencies within the HF band. The phase of the signals to each antenna is controlled electronically, which allows for maximum antenna gains in 16 directions. Besides the maximum power into the main transmission direction, the interference pattern of the 16 beams has additional side lobes. One main lobe has an azimuthal width of about 4°. See figure 3.2 for a modelled antenna pattern for two of the beams and a frequency of 10 MHz. The main lobes are normalized to 0 dB, whereas the side lobes in the forward direction and the backward pointing lobe have gains with at least 14 dB and 10 dB in power decrease. The 16 beam lobes overlap slightly to form a broad coverage of directions resulting in an azimuthal sector of 52°. Due to ionospheric refraction the range of the radio waves can be very large, typically between 180 - 3550 km.

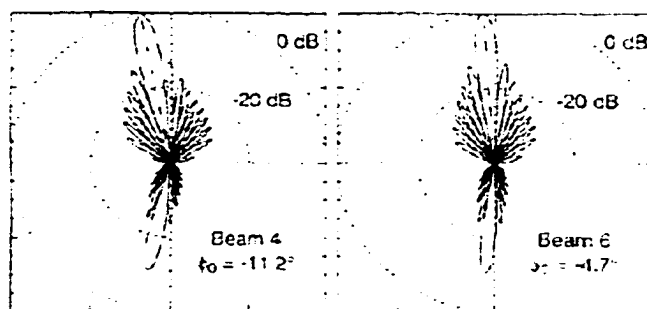


Figure 3.2. Modelled beam pattern for beams 4 and 6 and a 10 MHz frequency, the elevation angle is at zero degrees. After *Milan et al.* [1997b].

The signal pulses are transmitted in a specific sequence. The pulses in the sequence have characteristic lag separations. Minimum and maximum lag separation determine the shape of the backscatter auto-correlation function and the spectral resolution of the Doppler-shifted return signal. For the calculation of distance traveled, a straight-line propagation is assumed. This places the theoretical (virtual) scattering height at greater altitudes than the



actual scattering height, which is lower in altitude due to refraction. The estimated error of this assumption is in the range of 15-30 km [Villain *et al.*, 1984; Ruohoniemi *et al.*, 1987], less than the radar radial resolution. The range resolution is determined by the length of the transmitted pulses, 45 km for the typical pulse length of 300  $\mu$ s. This radial length together with the azimuthal resolution defines the size of a “backscatter cell” in the radar FOV. Each beam has 75 of those range gates, with a total of 1200 possible backscatter cells for any given scan. Under normal operating conditions transmission and listening modes are set to about 7 seconds per beam. Every 2 minutes a new scan is started making this the standard SuperDARN time resolution. However, some of the data presented here were obtained with one minute resolution.

The received scattered signal is preprocessed on site and further prepared at the research centers operating the respective radar sites. A functional fit to the decorrelation of the auto-correlation function at each range gate leads to an estimate of the power and spectral width of the received backscatter [Milan *et al.*, 1997b]. The mean line-of-sight Doppler shift is determined from the shift in the auto-correlation function as a function of lag number [Hanuise *et al.*, 1985]. These calculations render a total of three generally used variables. A secondary antenna system, consisting of four antennas, is positioned about 100 m distance from the main antenna array. Cross-correlation of the signals of the incoming wave at both antennas determines the angle of the wave vector. Due to large data volumes this additional information is not always stored along with the other variables. For this study, concentrating on the existence of irregularities and their detectability by HF radar signals, the main variable is, apart from the fact of scatter occurrence, the power in the scattered signal. A description of this and the other variables are given in the paragraphs below. For a more detailed description of the SuperDARN system see e.g. Greenwald *et al.* [1995].

### **Backscatter Power**

The absolute power of the backscattered signal is dependent on a number of variables, ionospheric as well as radar specific. Mathematically it is described by the radar equation. The radar equation includes ionospheric and radar parameters, and propagation-related variables, such as the range or absorption along the path. Ionospheric parameters are represented by the radar cross section, which depends among others on the electron density

fluctuations, the angle of incidence on the boundary normal of the irregularity structure, and the angle between the wave vector and the plasma flow [Hanuise *et al.*, 1991]. Radar parameters contain variables such as transmission wavelength and radar gain.

To identify a backscattered signal, the power of the received wave has to exceed the power in the background noise. The backscatter power is indicated as ratio of the power in the received signal to the noise level. The latter varies with the presence of other man-made HF radio transmission and also with the sky brightness temperature [Walker *et al.*, 1987]. The sky brightness temperature is an empirical equivalent measure representing the level of natural sky noise, it varies with the employed radar frequency and the receiver bandwidth. For a bandwidth of 60 kHz and a 10 MHz wave frequency the sky noise is of the order of  $2 \times 10^{-13}$  W. Maximum backscatter powers are of the order of 35 - 40 dB over the noise level. Compared to the 9600 W transmission power, the strongest signal power is of the order of 130 dB below.

### Doppler Velocity

The Doppler-shift in the frequencies of the return signal indicate the line-of-sight drift velocity of the ionospheric structure that is responsible for backscatter. Since collisions with the neutral atmosphere are negligible in the *F* region, the ambient plasma motion with velocity  $\mathbf{v}$  is a direct consequence of the ionospheric electric field,  $\mathbf{v} = \frac{\mathbf{E} \times \mathbf{B}}{B^2}$ . Ionization and structure within the ionization are equally affected by the electric field and drift with the ambient plasma.

Spatial and temporal velocity fluctuations, due to temporally enhanced local electric fields, are likely in the vicinity of auroral arcs [e.g., Marklund *et al.*, 1998]. During precipitation events electric fields are found converging towards auroral arcs [Marklund *et al.*, 1998]. The electric field within auroral structures is typically markedly reduced, because of the accompanying higher conductivity. The field intensifications are found to occur at the arc edges or in between bright auroral fine structures. Values inside and near auroral forms can vary markedly from below 10 mV/m to about 100 mV/m [Aikio *et al.*, 1993] or several hundred mV/m [Lanchester *et al.*, 1998] in the vicinity of the arc. Drifts as a result of electric field intensities larger than 50 mV/m are in the the range  $\geq 1$  km/s.

Enhanced convection velocities in connection with aurora have been reported by e.g. *Milan et al.* [1997a] and *Yeoman and Lühr* [1997]. *Milan et al.* relate the luminosity of the auroral emissions with the magnitude of the flow velocity. In their high temporal resolution radar echoes *Yeoman and Lühr* interpret the transient flow events during a substorm as effects of ionospheric current vortices associated with field-aligned currents.

### **Doppler Spectral Width**

The Doppler shift of the echo frequency has in general more than one spectral component. The spread in Doppler velocities has SI units of meters per second. The term spectral “width” is thus referring to the width of the spectrum in velocity space. Increases in spectral width may be due to structured events in the illuminated volume such as temporally or locally confined changes in velocity, or due to turbulent flows with varying line-of-sight velocity components, or to a multipeak velocity distribution from two or more distinct populations in velocity space. *Hanuise et al.* [1993] pointed out that the autocorrelation function determining the spread in drift velocities has a characteristic shape for the two latter of the possible processes.

Levels of spectral widths have been established as significant identifiers of the cusp in the dayside ionosphere. *Baker et al.* [1995] ascribed the wide and complex spectra to structured line-of-sight velocity differences within single radar gates, although the cause of this phenomenon is not quite understood yet.

### **Elevation Angle**

The extended elevation angles are a consequence of the vertical extension of the beam lobes. They range from around  $0^\circ$  to about  $35^\circ$ . The value of the elevation angles is not used in the determination of target distance together with the signal travel time. This information is to be included in calculations at some point in the near future (*W. Bristow*, personal communication, 2000). If taken into account, it could help resolve wave paths and subsequently data interpretation for abnormal ray paths. For example, high elevation angles together with a long range travel time indicates multi-hop propagation. Sudden variations over a large angle, although the scatter distance may remain the same, correspond to rapid changes in ionospheric conditions. An experimental evaluation of the return angles was done

by *Greenwald et al.* [1988]. The experimentally determined ray path showed variation from the theoretical path due to a non horizontally stratified ionosphere, leading occasionally to occurrences of topside ionospheric backscatter.

### Ground Scatter

Ground scatter can be identified by a characteristic pattern of the return signal. A combined occurrence of Doppler velocity values below 50 m/s and spectral spread of under 20 m/s is assumed to be due to groundscatter off the stationary surface of the Earth. Return echoes fulfilling both criteria are colored grey in the data diagrams and not included in the analysis of ionospheric scatter. Figure 3.3 presents backscatter from one beam of the SuperDARN Kodiak data in the typical display, as available on the SuperDARN homepage at <http://superdarn.jhuapl.edu>. The three panels show, from top to bottom, signal power, line-of-sight Doppler velocity, and spectral width. Indicated at the top are the transmission frequency and the noise level during the interval.

#### 3.1.2 Propagation Modes

Radio waves in the HF range are easily refracted by typical density gradients in the ionosphere. Due to their curved paths they can travel to large ranges and are therefore used in the ground-to-ground radio communication. The nomenclature in the HF mode propagation originates in the early days of radio transmission between ground stations. One ground-to-ground loop, involving a reflection in the ionosphere, was denoted as a whole hop. The hop is labeled according to the reflection altitude, e.g. 1F (1E) for reflection in the  $F$  ( $E$ ) region. This denomination is also used for ground backscatter in radar returns. Ionospheric backscatter as seen by a radar station originates between ground reflections and is consequently measured in half integers, such as  $\frac{1}{2}F$  or  $1\frac{1}{2}E$ . Here the latter propagation mode comprises forward scattering off the ground. A particular wave path cannot be resolved entirely in any given case without detailed knowledge of the ionospheric conditions along the path. However, based on modelling and experimental work certain propagation modes could be established [*Villain et al.*, 1984; *Greenwald et al.*, 1988]. They depend on the density structure in the ionosphere, the wave frequency, and the azimuthal look direction of the beam with respect to the magnetic orientation. Figure 3.4 illustrates

possible ray paths in the model by *Villain et al.* [1984] which include  $\frac{1}{2}E$ ,  $\frac{1}{2}F$  and  $1E$  modes. Any combinations of ground and ionospheric backscatter are theoretically possible. The limitation in far range detection is given primarily by the threshold of detectability of a weak return signal in the noise and the time limit on the listening mode of the antennas.

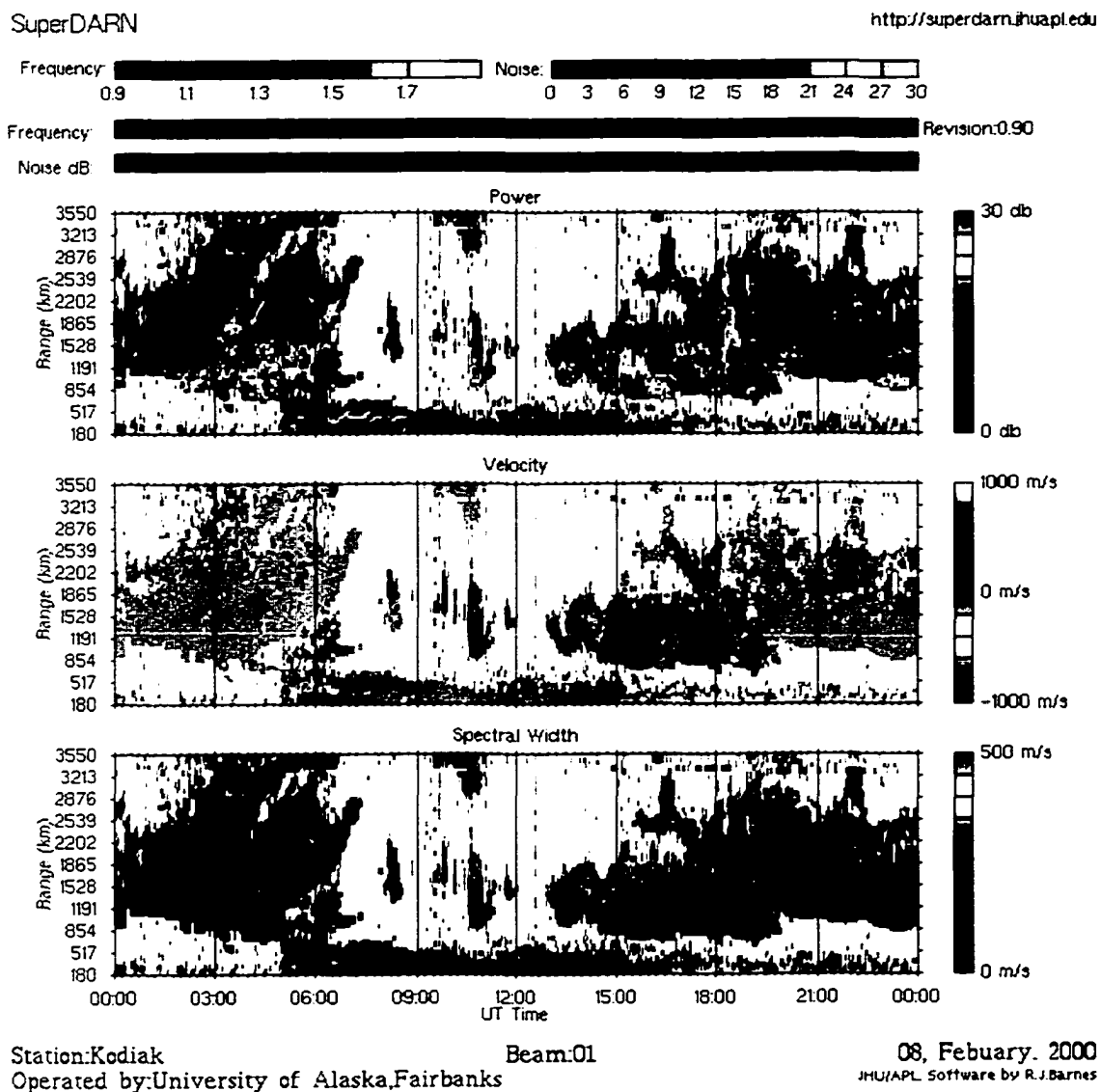


Figure 3.3. Example for a scatter diagram for one radar beam (Kodiak, February 8, 2000).

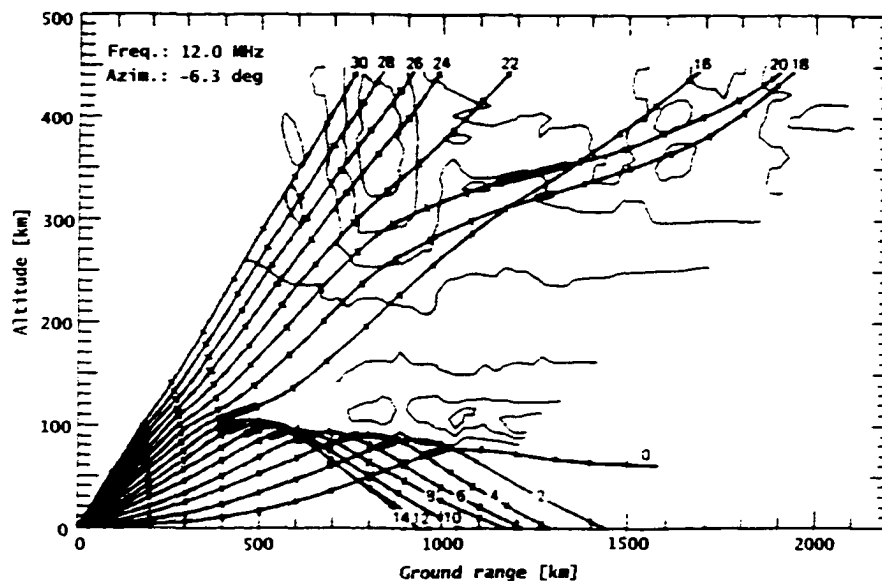


Figure 3.4. Modelled HF ray tracing for a given electron density, an azimuth of  $30^\circ$  away from magnetic north, and a frequency of 12 MHz [Villain *et al.*, 1984].

In the calculation of distances between radar and target a propagation along straight lines is assumed. The assumed virtual scattering height is set to 400 km for scattering in the *F* region. Scatter from this altitude is assumed whenever the slant range of the virtual scattering path exceeds 800 km. Near-range ( $\leq 600$  km slant range) *E* region scatter is projected into 115 km. Between 600 - 800 km the virtual height is calculated by an interpolation formula. As already mentioned, the error in these assumptions has proven to be less than the radial resolution [Villain *et al.*, 1984]. There are however possible ray paths, implying a large horizontal wave vector component, which would result in larger errors.

For the attempted spatial collocation analysis of optical and radar data, the geographical coordinates of the cell corners were converted to corrected geomagnetic coordinates (cgm). The corner coordinates are obtained per default from the SuperDARN data processing program. The conversion was done by means of a model (GEO-CGM.FOR, version 9.9) that was obtained from NASA's National Space Science Data Center at <http://nssdc.gsfc.nasa.gov/space/model/>. The altitude-specific information in the custom-

ary altitude corrected cgm (or PACE) coordinates is already implied in the prior program conversion to altitude-independent geographic coordinates.

### 3.2 Meridian Scanning Photometer

The meridian scanning photometer at the observatories in Poker Flat, Alaska. ( $65.41^\circ$  cgm N.  $212.53^\circ$  cgm E) and Longyearbyen, Svalbard. ( $75.12^\circ$  cgm N.  $112.8^\circ$  cgm E) served as main indicator for the optical auroral conditions. With an orientation along the geomagnetic meridian an MSP provides information about the expanding and contracting auroral oval and the north-south motion of auroral arcs within it. The instrument typically has four to five channels in operation monitoring four or five auroral emission lines simultaneously. Each channel consists of a narrow-band interference filter with  $4 \text{ \AA}$  spectral resolution and a cooled photomultiplier tube. A rotating mirror in front of the assembly scans the sky from geomagnetic north to south. See figure 3.5 for a sketch or figure 3.6 for a photograph of an MSP assembly. The zero angle is assigned to the northern horizon, the zenith is at 90 degrees, and 180 degrees denotes the southern horizon in the geomagnetic meridional

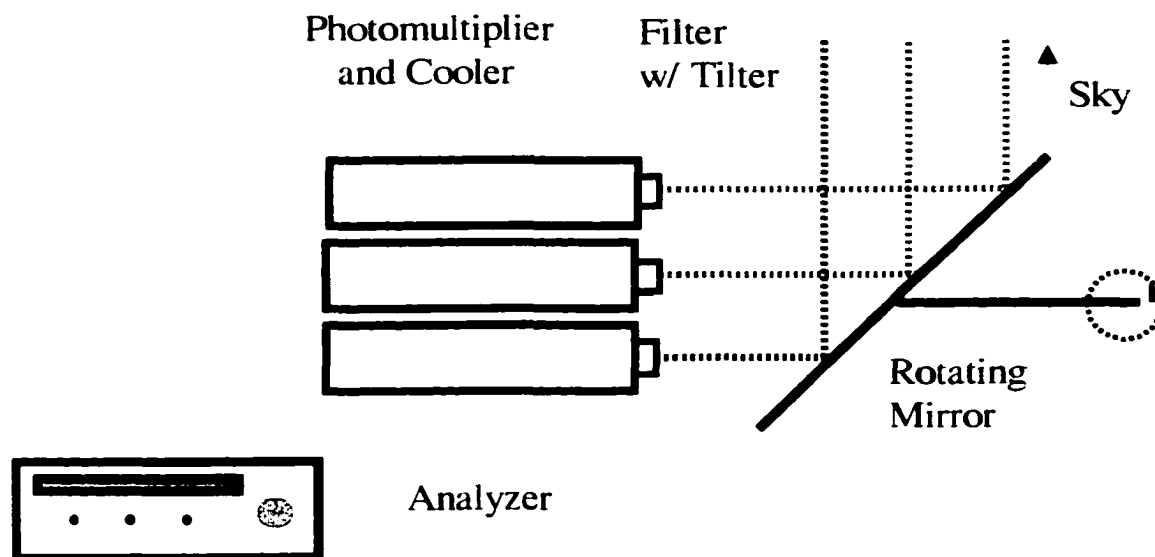


Figure 3.5. Schematic setup of the MSP, shown here with three channels.

plane. The incident light is directed through a filter to the entrance of the photomultipliers, filling approximately a  $1^\circ$  FOV. The filters are tilttable, and are rotated alternatively to two positions by a system-controlled motor. At one position, the passband is centered at the peak of an auroral line. At the other, the passband is in the close vicinity of the line, usually on the long wavelength side, to determine the background radiation. The location of the appropriate tilt angles depend on the desired wavelength and filter, and has to be calibrated periodically to adjust for temperature fluctuations and material performance. The subtraction of the measured base brightness from the peak line brightness, renders the auroral signal largely unaffected by continuum light contaminations. The mirror has a rotation period of 4 seconds, thus scanning the sky along the geomagnetic meridian in 2 seconds. Every other revolution is used to measure the peak and background line respectively. Two individual peak and base scans are averaged, totaling an overall time resolution of 16 seconds per produced scan.



Figure 3.6. MSP mount with five channels at the Longyearbyen Auroral Station. The instrument is to the right, the mirror to the left shows the front view of the cable-connected filter tilting devices.

The four traditionally monitored auroral wavelengths in the MSP are the forbidden transitions of atomic oxygen [OI] at 630 nm and 557.7 nm, the molecular band of  $N_2^+$  1NG



at 427.8 nm and the hydrogen Balmer line  $H_{\beta}$  at 486.1 nm. See figure 3.7 for a typical keogram with MSP data. The four panels show auroral brightness measured at the four wavelengths as a function of time and MSP elevation angle. North is at the top of each panel, south at the bottom. The day displayed is among the data intervals investigated.

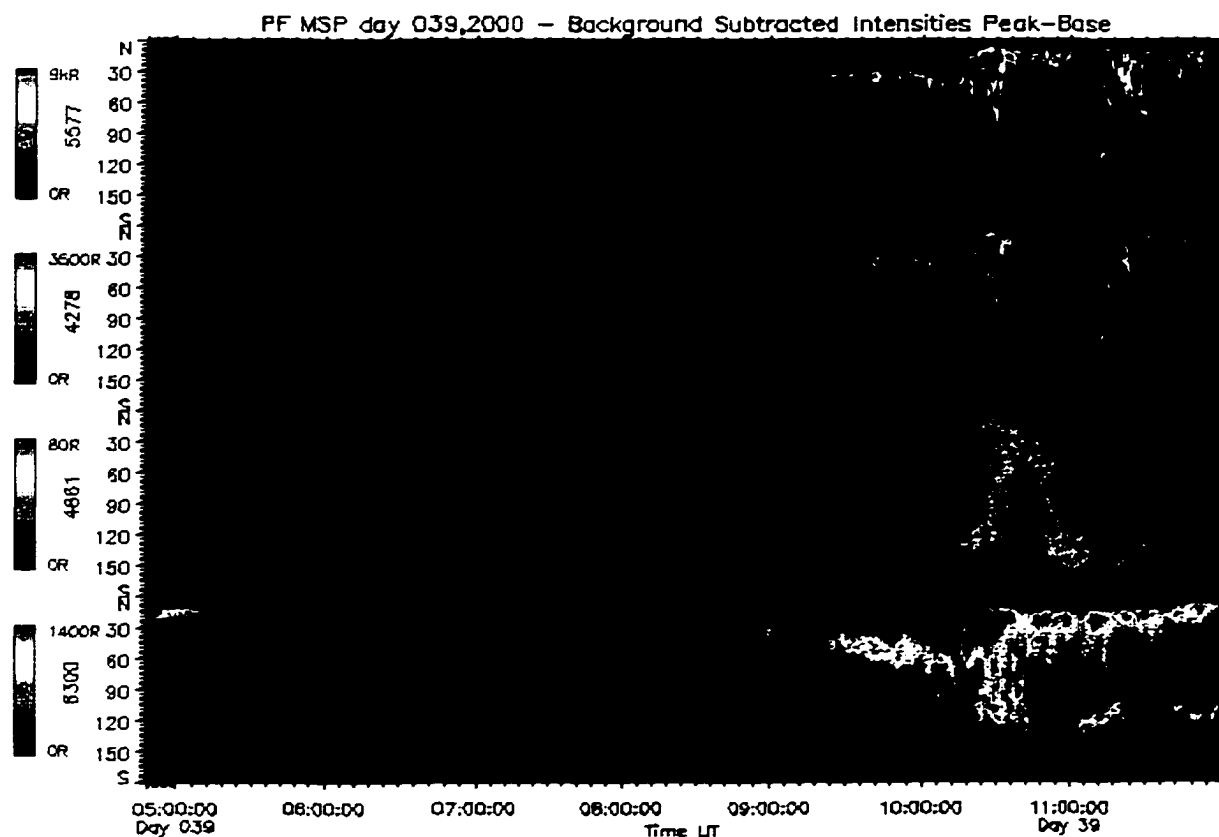


Figure 3.7. Example for a MSP keogram (Poker Flat, February 8, 2000). Measured auroral brightness as a function of time and MSP elevation angle. North is to the top in each panel. The wavelengths are, from top to bottom, 557.7 nm, 427.8 nm, 486.1 nm, and 630 nm.

The auroral emissions at the wavelengths at 427.8 nm, 557.7 nm, and 630 nm are excited mainly by electron impact. The hydrogen line is indicative of proton precipitation. Of these wavelengths, the red line at 630 nm originates in the same ionospheric altitude

range as probed by the radar. This auroral emission corresponds to soft precipitation (few hundred eV to 1 keV) with energy deposited in the  $F$  layer between roughly 200 - 500 km altitude. It is therefore a good indicator for auroral-related processes associated with plasma irregularity generation. Collisionally excited oxygen atoms have a radiative lifetime of 110 seconds [Vallance Jones, 1974]. Due to the long lifetime of the excited state, the emission of light can be prevented by collisional deactivation on shorter time scales. Collisions at lower altitudes are the reason for the high source altitude of this auroral wavelength. The transition region, below which quenching dominates, lies at about 200 km altitude. This mechanism, and the higher ionization rates in the last few kilometers of precipitation [Rees, 1988], render the lower red border better defined and more constant in altitude than the upper boundary. The upper border is very variable, with values between 400 up to 700 km, depending on the low-energy end of the incoming electron distribution. Peak emissions are typically in the range 220 - 300 km [Omholt, 1971].

To compare the optical measurements with the radar backscatter a constant emission altitude of 250 km for the red aurora was adopted. This allowed the projection of the measured brightness as a function of elevation angle into a constant altitude. MSP diagrams were made showing the red auroral as a function of magnetic latitudes, enabling comparison with the radar data. These diagrams will be introduced in chapter 4. Additionally, the lower border of the red emission was determined from the MSP keograms. It originates below the peak of the emission at 250 km. An altitude of 200 km for the lower border was assumed and overplotted on mapped MSP diagrams showing the red auroral line.

The blue auroral emission at 427.8 nm occurs at  $E$  region altitudes, with an average intensity peak at 110 km, implying higher precipitation energies [Vallance Jones, 1974]. Its intensity is relatively independent of the mean energy of the precipitating electrons. Therefore it is often used in relation to the 630 nm brightness to serve as an indicator for the characteristic energy of precipitating electrons. A higher ratio of  $I(630)/I(427.8)$  intensity signifies a greater ionization altitude and therefore lower characteristic energies. As a rough guideline, characteristic energies of 1 keV and lower are found for ratios of 1 and above [Lummerzheim et al., 1990]. In the present analysis the blue line is added to the mapped MSP diagrams for the supplementary information about the range of incoming

particle energies and affected altitude regions. It is displayed mapped into its adopted peak emission altitudes of 110 km.

The projection is performed by calculating the angular distance at the center of the Earth between the MSP observatory and the emission in the assumed altitude. It is based on the following assumptions: The Earth is a perfectly round sphere with a radius equal to the local Earth radius at the observation site. The scanning plane of the instrument is along the magnetic meridian. The meridian represents a great circle on the spherical Earth. The assumptions were tested in extending the direction of the scanning plane with extrapolated coordinates to the north in a test mapping. The extended coordinates were directly incident on the geom north pole, the scanning plane was therefore found to indeed have the assumed orientation. The resulting mapped magnetic latitudes are altitude-independent and can thus be directly related to the radar records in magnetic format.

The projection of the MSP elevation angles implies two concomitant effects that should be borne in mind in the data interpretation. The first is that mapping outside a narrow range of angles around the magnetic zenith introduces a distortion which increases with off-zenith look angle. Figure 3.8 shows the nonlinearity of mapping latitudes into an assumed emission height at 250 km. Emissions closer to the horizon than approximately  $45^\circ$  elevation

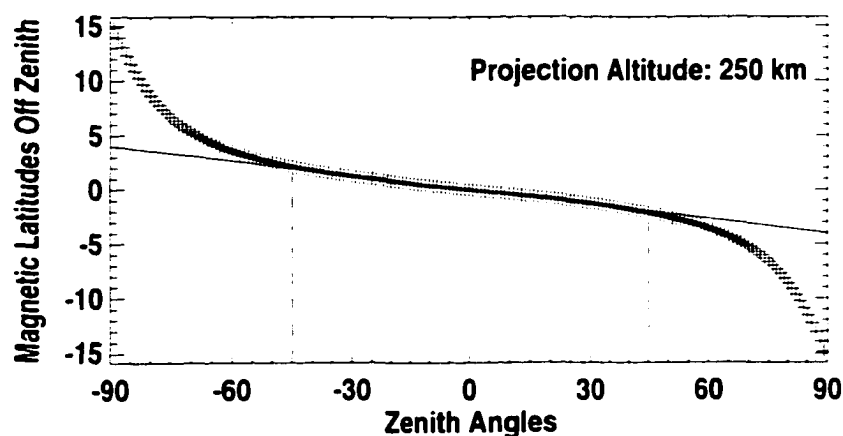


Figure 3.8. Mapping of MSP zenith angles to an altitude of 250 km. The solid line traces the tangent to the linearly mapped part. The dashed lines shows the linear range to be between  $\pm 45^\circ$  around zenith.

angle will appear increasingly stretched in latitude. Translated into magnetic latitudes, the linear interval ranges from around  $\pm 2.5^\circ$  degrees north and south of the zenith through the observatory. The second effect that must be kept in mind is that there is no discrimination between tall auroral rays and broad arcs at locations other than directly overhead. Both appear as latitudinally extended emissions in the mapped image. In an original MSP keogram the lower part of a height-extended structure has a higher off-zenith angle. In a mapped image the same structure translates to a stretched blob, with the lower border having the greater distance to the observing station (figure 3.9).

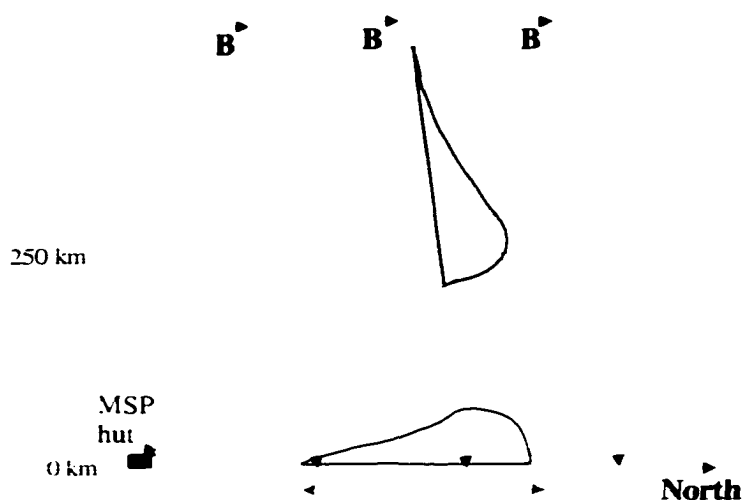


Figure 3.9. Original and projected emission profile of a tall field-aligned auroral structure for a flat Earth. The lower (upper) emission border maps to a greater (smaller) distance from the observing site, resulting in an apparent latitudinal extent.

The error introduced by the assumption of a constant emission altitude can be quantified by simulating a varying emission altitude. Softer precipitation can have the height of the peak brightness of the red aurora at 400 km or higher. At  $45^\circ$  degrees from the horizon as seen by the MSP, the difference in projected altitude between 250 km and 400 km translates into a displacement of  $1.2^\circ$  in latitude. For  $20^\circ$  from the horizon the displacement comes to  $2.6^\circ$  degrees. Figure 3.10 illustrates the difference in mapping for three assumed emission altitudes: 250 km, 350 km, and 450 km.

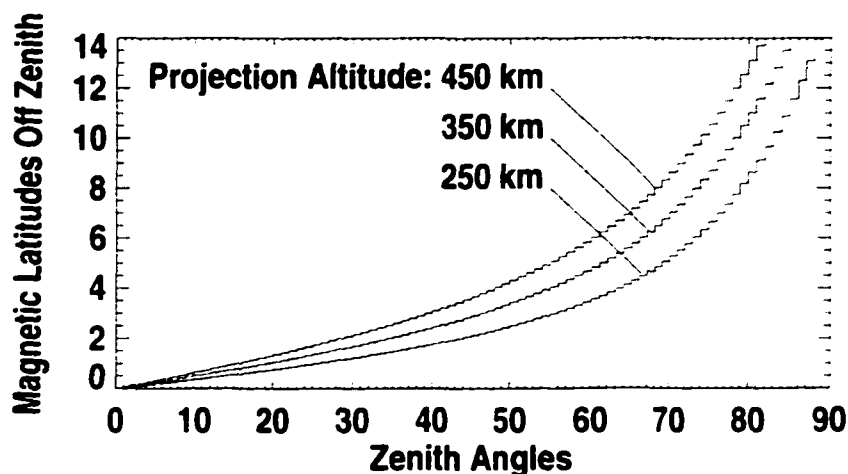


Figure 3.10. Effects of altitude projection of MSP zenith angles to three different altitudes: 250 km, 350 km, and 450 km.

### 3.3 Allsky Camera

To gain additional information about two-dimensional horizontal structure in the aurora, images from an allsky camera were investigated. Both observatories housing the MSP instruments are also equipped with allsky cameras. A schematic setup of the camera is shown in figure 3.11. The assembly includes a wide-angle  $f/2.8$  fisheye lens at the point of light entrance, followed by an intensifier. The camera is mounted vertically, recording the entire sky. Two lenses in the optical path focus the intensified image onto a  $1.5 \times 1.5 \text{ cm}^2$  CCD in the back of the camera. The intensifier has an adjustable gain, but readjusts its sensitivity automatically within the given range. During a bright auroral display sensitivity is thus decreased versus during dark and quiet conditions. Allsky images are therefore inherently not intensity calibrated, but register only relative brightness. A shutter enables manual or program-controlled protection from overexposure of the sensitive equipment. The recording is made for white light on this occasion, i.e. no wavelength filter is used. The recording speed is 30 frames per second. The storage medium is broadcast quality VHS tapes. The images for the data analysis were grabbed from the tapes at intervals in the

radar resolution of one or two minutes. The active wavelength range of the intensifier is in the visible between 400-900 nm, with the highest sensitivity between 600-700 nm. On the long wavelength end of this interval are auroral emissions which are very bright, compared to other wavelengths [Vallance Jones, 1974]. These are the auroral bands from molecular nitrogen  $N_2$  1P in the infrared. They are likely the dominating feature in an ASC image. However, the wavelength cannot be discerned in the white-light recordings. The emission altitude for the  $N_2$  1P transitions is at *E* region altitudes between 95 - 150 km [Vallance Jones, 1974]. An average altitude of 110 km was adopted as reference altitude in projections.

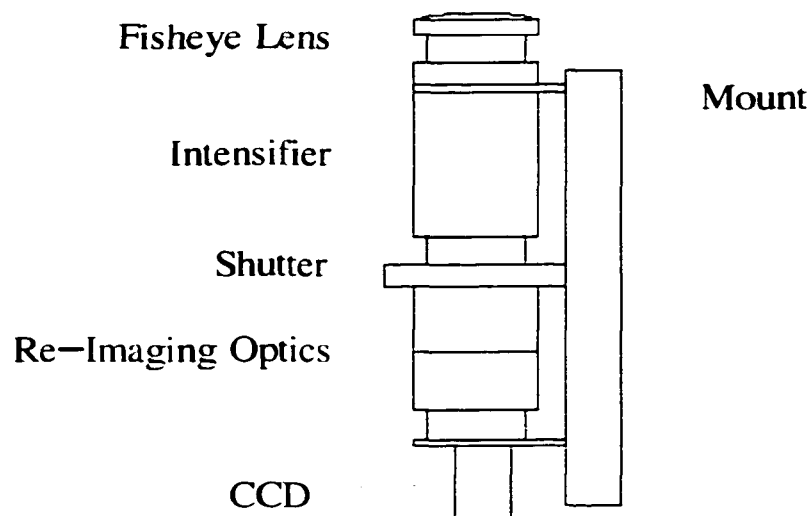


Figure 3.11. Schematic setup of the ASC.

For the analysis the images were calibrated spatially by comparing observed star positions against their catalogue coordinates. The calibration was repeated for every auroral season at a date close to the days of interest under clear sky conditions with visible stars. A coordinate conversion program, based on calculations by H. Stenbaek-Nielsen (University of Alaska, 1998), was then used to project every image pixel into geographic coordinates. The images could thus be superimposed on a map together with the radar backscatter locations.

Mapping of allsky images has the same restrictions as was discussed for the mapping of MSP scans, with the implication that vertical structures convert to seemingly horizontal extensions. The predominance of lower emission altitudes which are also vertically more confined, results in smaller errors close to the horizon, than for high emissions. An analysis of the linearity of the mapping function indicates that the range of linear projection extends to  $45^\circ$  degrees off zenith for 110 km altitude as shown in figure 3.12. However, a larger angle was chosen here ( $75^\circ$  degree) to provide additional information about the immediate vicinity of observed emissions. This produces an observed circle with a diameter of about 810 km radius at 110 km altitude.

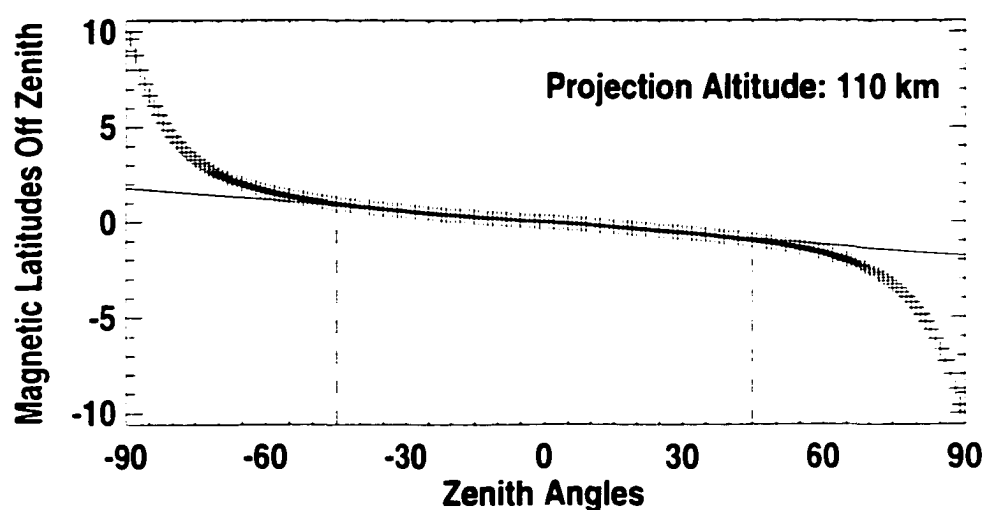


Figure 3.12. Mapping of zenith angles to an altitude of 110 km. The solid line traces the tangent to the linearly mapped part. The dashed lines shows the linear range to be between  $\pm 45^\circ$  around zenith.

## Chapter 4

# Analysis of Optical and HF Radar Data

The state of the ionosphere does not arise instantaneously but is a result of current processes and the immediate history, dating back minutes, hours, and even days. Linear and turbulent diffusion and decay, transport, and recombination have different time constants, some of them very large. For the large-scale scope of research involving coherent backscatter a close causal examination of ionospheric condition and the generation of a signal echo is not desired nor required. Independent of the whys and hows of scatter generation the working approach to data utilization is to use data whenever they are available. On the basis of a radar network spanning over large portions of both polar hemispheres a patchwork of signal receptions weave into a carpet of information about high-latitude ionospheric fields and dynamics.

This chapter takes a closer examination of the relationship between backscatter and aurora at magnetic nighttimes and speculates about its nature and stringency. There is no simple correlation between the two phenomena, the interplay of optical and radar aurora has vastly different facets. They range from linear correspondence through unrelatedness to anticorrelation. An appropriate choice of events could therefore support widely differing hypotheses. Different aspects of the connection between the two observational aspects are investigated to provide insight into underlying mechanisms.



The chapter starts with an overview over other work relating aurora and HF backscatter. Then the investigated data set will be introduced. A statistical approach to this data set will be described. Important processes determining the reception of HF signal echoes will be investigated and illustrated with the help of data. Given the complexity of the ionosphere detailed knowledge of cause and effect in any given case seems difficult to achieve. However, estimates of the efficiency of ionospheric parameters in the formation of measured phenomena are possible if the impact is intense and/or the background activities low. At times there are indicators that one particular factor in the general picture dominates. Examinations of such cases are presented with interpretations which can be deduced from them.

## 4.1 Comparison With Dayside Conditions and Other Studies

Previous studies combining HF scatter and aurora have mainly concentrated on dayside events. An obvious reason is the high plasma density on the dayside, which supports wave propagation much better than the dark ionosphere of the nightside. Optical dayside studies have mainly concentrated on the region of the magnetospheric cusp over Svalbard. While the cusp region itself lies in darkness, suitable HF propagation conditions are found through supply of ionization sources along field lines. Frequent steady particle fluxes for durations of minutes account for plasma concentrations and structure on the dayside [Fejer and Kelley, 1980].

Among the studies involving optical data, the detection of reliable signatures of the magnetospheric cusp region in HF backscatter has been investigated by Baker *et al.* [1995] and Rodger *et al.* [1995]. Baker *et al.* [1995] define cusp characteristics to consist of elevated values of spectral width, with peak values of  $\geq 220$  m/s, while 60 m/s are found at the neighboring regions. The technique of comparing signatures consisted of overplotting the lower emission boundary defined by an MSP over the radar keograms. This method gave only occasionally satisfying results during nighttimes. Rodger *et al.* found ionospheric signatures of the magnetospheric cusp region in radar and ASC to be better than  $1^\circ$ . However a clear one-to-one correspondence of optical and radar aurora could not be established. In a comparison between dayside auroral activity and coherent HF backscatter, Moen *et al.* [2000] pointed out the three likely sources for irregularities in the cusp region:  $\mathbf{E} \times \mathbf{B}$  gradi-

ent drift instabilities as the dominating source during southward IMF, velocity shear driven instabilities during northward IMF, and further field-line “stirring” [Tsunoda, 1988] leading to interchange of low and high density plasma tubes.

Correlated studies between auroral emissions and HF backscatter has also a short history for substorm-type aurora. *Yeoman and Lühr* [1997] estimated flow velocities during substorm times and found auroral signatures in HF returns. But they also encountered signal dropouts that they ascribed to magnetic activity. *Lui et al.* [1998] investigated a moderate isolated substorm. A few scattered signals were interpreted as originating at the expanding auroral electrojet, until they vanished in the following onset. *Lester et al.* [2000] discovered an occasional correspondence between the gradient in spectral width and the polar cap boundary, with large spectral widths poleward of the boundary. Very limited generation of irregularities by optical features was stated by *Milan et al.* [1997a], who concentrated on the change in the flow pattern in the vicinity of optical arcs. A similar approach was done by *Voronkov et al.* [1999], who found flow velocities with enhanced values during the substorm growth phase. Investigating flow changes during a small isolated substorm, *Lewis et al.* [1997] noted a change in flow direction, corresponding to the signature of an upward field-aligned current within the radar FOV. Large-scale dropout of backscatter at onset accompanied the backscatter pattern. It is quite common to find scatter dropouts hampering correlation studies between optical and HF radar aurora. It can be speculated, that this is the reason why close investigations of the relation between auroral emissions and backscatter reception have not yet been attempted.

## 4.2 Outline of the Observations

The data periods were selected on the criteria of availability of both radar and optical data during magnetic night, the condition of sufficiently clear sky, aurora in the FOV of the optical instruments, and the presence of a reasonable amount of scatter. This combined filter decreases the number of days in any auroral season drastically. Backscatter without auroral displays, albeit common, was not considered.

Among the data sets investigated, a distinct difference in backscatter occurrence was found between the Kodiak and the CUTLASS radar data. The occurrence level of received

echoes for the mid and far range in Alaska on many occasions exceeds the corresponding scatter occurrence over the Arctic Ocean. This is specifically noticeable in the vicinity of the optical observatories. The respective distance of the observatories to the radar sites, and the fact that the data collection took place in different phases of the sun spot cycle are likely important factors for this difference. The solar cycle in early 2000 approaches solar maximum conditions with higher solar fluxes and therefore higher ionization rates in the terrestrial environment. The data collection during the seasons 1997/1998 through 1998/1999 and late 1999, on the other hand took place during the rising solar cycle after the sunspot minimum number in summer 1997. In winter nights, with depleted ionospheric densities, under roughly solar minimum conditions, even waves with the lowest employed transmission frequencies are at times insufficiently refracted. The distance from Kodiak to the Poker Flat Observatory is with 875 km markedly shorter than the distance from the CUTLASS radars to the Auroral Station in Longyearbyen ( $\simeq 1800$  km). Higher power density in the vicinity of Poker Flat leads therefore to higher signal-to-noise ratios close to the observatory compared to Longyearbyen.

The differences in the auroral conditions at the two optical observation sites are determined by the  $10^\circ$  difference in their magnetic latitudes. This places the northernmost station in Longyearbyen during nighttime slightly poleward of the statistical auroral oval at around  $71^\circ$  degree latitude, whereas Poker Flat is positioned somewhat to the south of it, except under disturbed conditions. The two observatories experience therefore a different part of the nightly auroral display. Svalbard "sees" the poleward part of the poleward expansion rising from the southern horizon during increased magnetic activities in the magnetic night. The active nighttime interval intercepted at Poker Flat includes the equatorward expanding auroral oval of the substorm growth phase and the equatorward portion of the expansion phase. The diffuse auroral zone located in the equatorward section of the auroral oval, also affects the ionosphere over Poker Flat to a greater extent.

The first investigated data sets from Svalbard involving CUTLASS radars proved not to be very suitable for comparison with the meridional scanning plane of the MSP, due to generally few scatter events in this small area. The technique adopted for this site was to investigate the two-dimensional allsky camera images instead of the MSP scans, to enlarge the common FOV. Due to the bad quality of the ASC videotape in the auroral season

1995/1996 and the lack of ASC equipment at the Auroral Observatory in Longyearbyen in the season 1996/1997, data was only considered in the years 1997/1998 through 1999/2000. While this effort improved the understanding of the complex relation between optical and radar aurora considerably and as such constitutes a substantial part of the background for this thesis, the data set is very difficult to present in printed form. The reason lies in the scarcity of the scattered echoes in the relatively small common FOV of the instruments. Scatter and aurora development can easily be examined in the animations of the entire FOV, which however cannot be compressed in simple diagrams. In the SuperDARN Kodiak scatter records the same type of phenomena was found, but more scatter occurred in the MSP scanning plane. The majority of the data presented here originate therefore from Alaska.

Tables 4.1 and 4.2 show an overview over the data days contributing to this work for the Alaskan and Northern European events respectively. Indicated in the tables are the date, both in the day-of-year format and as year-month-day, the common times of the radar and optical observations, and the Kp values during these intervals. Days marked with an asterisk are presented in this chapter. The planetary K index describes variations in the

<b>Date</b>	<b>Times</b>	<b>Kp Values</b>
00063 - 000205	8-14	0 <sup>-</sup> . 1
00039 - 000208 *	8-12	2 <sup>-</sup> . 3 <sup>-</sup>
00040 - 000209 *	6-12	3 <sup>-</sup> . 1 <sup>-</sup>
00055 - 000224 *	8-10	4 <sup>-</sup> . 5 <sup>-</sup>
00057 - 000226	10-12	3 . 3 <sup>-</sup>
00061 - 000301 *	7-13	4 <sup>+</sup> . 4 <sup>-</sup>
00062 - 000302	6-12	2 <sup>-</sup> . 1
00063 - 000303 *	8-11	0 <sup>-</sup> . 1
00065 - 000305	8-12	1 <sup>-</sup> . 1
00067 - 000307	7-12	3 <sup>-</sup> . 3

Table 4.1. Overview over the data days taken in Alaska. Day of the year and date, times UT, and Kp values during the intervals. Days marked with an asterisk will be discussed.

magnetic field across a series of globally distributed magnetic observatories. They are due to the magnetospheric ring current and the auroral current systems. The Kp index is formed by taking a quasi-logarithm of the largest excursion in either the D or H component of the Earth magnetic field in a 3-hour period. The Kp index is a weighted average of the K indices from all stations. It ranges from 0 to 9. However, no Kp values higher than 5<sup>-</sup> are among the days under investigation. The three-hourly Kp indices start at the beginning of

Date	Radar	Times	Kp Values
97331 - 971127	e f	18-24 UT	1 <sup>-</sup> . 0
97337 - 971203	e	18-24 UT	1 <sup>-</sup> . 2
97339 - 971205 *	e	18-24 UT	2 . 3 <sup>-</sup>
97354 - 971220	e f	18-24 UT	1 <sup>-</sup> . 1
97356 - 971222	f	18-24 UT	1 <sup>-</sup> . 0 <sup>-</sup>
97360 - 971226	e	18-24 UT	0 <sup>-</sup> . 1 <sup>-</sup>
98027 - 980127	e f	18-22 UT	2 <sup>-</sup> . 1 <sup>-</sup>
98028 - 980128	e f	18-24 UT	1 <sup>-</sup> . 1
98323 - 981119	e f	18-24 UT	1 <sup>-</sup> . 1
98328 - 981124	e f	18-24 UT	4 . 3 <sup>-</sup>
98346 - 981212	e f	18-24 UT	2 <sup>-</sup> . 2
99007 - 990107	e f	18-24 UT	3 <sup>-</sup> . 2 <sup>-</sup>
99009 - 990109	e f	18-24 UT	2 . 3 <sup>-</sup>
99010 - 990110	e f	18-24 UT	1 <sup>-</sup> . 1
99014 - 990114	e	20-24 UT	3 . 4 <sup>-</sup>
99042 - 990211	e	18-24 UT	4 . 3
99334 - 991130	e	20-22 UT	2 <sup>-</sup> . 3 <sup>-</sup>
99335 - 991201	e f	20-22 UT	2 . 1 <sup>-</sup>
99349 - 991215	e f	18-22 UT	1 <sup>-</sup> . 3

Table 4.2. Overview over the data days taken in Northern Europe. Day of the year and date, radar site (e - Pykkvibær, f - Hanksalmi), times UT, and Kp values during the intervals. Data from the day marked with an asterisk will be discussed in this chapter.

each three-hour interval during the day. The additional column in table 4.2 refers to the location of the CUTLASS radar involved at this day (e - Pykkvibær, f - Hanksalmi).

The times in the investigation are on the nightside of the Earth, around local magnetic midnight. Local magnetic midnight for Poker Flat is at 11:10 UT, midnight at Longyearbyen is at 20:40 UT. The sky has to be dark for optical auroral observations. A dark ionosphere also permits sharper electron density gradients than can be present under sunlit conditions, thus enhancing ionospheric structure. The minimum solar depression angle for the days presented here is  $-27.5^\circ$ , ensuring a dark atmosphere up to around 800 km altitude. Due to absorption of the UV portion in the solar rays along the long pathlengths through the atmosphere in winter nights, ionization altitudes are still higher.

The effects of solar ionization can be seen in HF coherent backscatter echoes. Figure 4.1 presents scatter pattern of a whole day for one beam of the Kodiak radar for February 24, 2000. The three panels show, from top to bottom, signal power, line-of-sight Doppler velocity, and spectral width. The dominating feature in this plot is due to groundscatter, colored grey in the middle panel. It arises when ionospheric densities are high during the day (local noon is at 22:15 UT), reflecting radio waves back to the ground. As densities decay after sunset, the refracting layer is found at greater altitudes, moving groundscatter to larger distances. The groundscatter pattern is roughly symmetric around local noon, and depends on the ionospheric time constants.

The times and locations of importance for this nighttime study around Poker Flat latitudes are found in this diagram between approximately 06 - 12 UT, and at distances between 700 - 2000 km. The locations are set by the overlap with the optical FOV of the MSP. For this particular day, the ionospheric scatter associated with the Doppler red- and blue-shifted signals in that temporal and spatial interval is the candidate for investigation. Another important effect can be recognized on this day: The short change to higher frequencies at around 08:30 UT affects the reception of echoes, mainly causing a gap in the groundscatter. A change in frequency changes the critical angle, the angle below which rays are reflected from the ionosphere. The critical angle is lower for the less refracted higher frequencies. By decreasing the angle, the distance to the nearest ground scatter increases. The effect is not as severe for ionospheric backscatter, since the vertical extension of irregularities facilitates

scatter over a broad range of altitudes. The size of irregularities that the signal is sensitive to, does not change appreciably for this frequency shift.

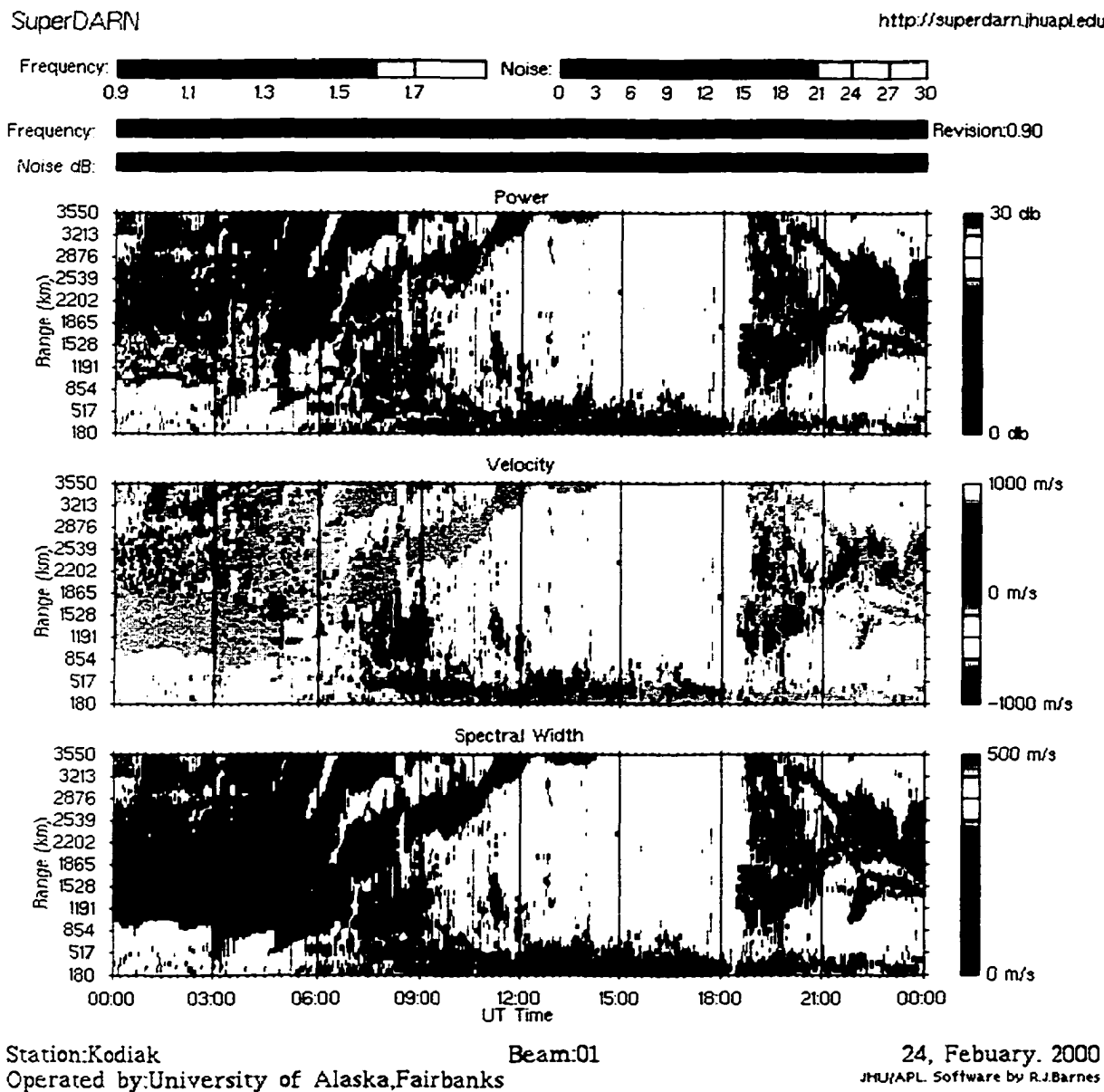


Figure 4.1. All-day scatter results for SD Kodiak, beam 1, on February 24, 2000.

The overview diagram for the CUTLASS radars has typically similar local time effects, but shifted in UT. The distances to the MSP FOV of the observatory on Svalbard are larger. They range from 1990 - 2160 km for the radar in Pykkvibær. A slightly larger interval, 1090 - 2370 km, is used for the latitudinally more spread FOV of the radar probing from Hankalsami.

Throughout the period of the present data, the Kodiak site has a time uncertainty. The radar started operations in the end of the first week of January 2000. In the middle of April 2000 a time delay of the system clock of 5 minutes was ascertained. The linearity of the delayed system clock is unknown. With the radar operations being uninterrupted since their beginning, a functional approach is therefore to assume a steady time slip. The approximately 100 days of operations with a final time difference of 5 minutes result therefore in an average daily delay of 3 seconds. This implies time shifts of 90 seconds to about 3 minutes for the first and the last day, respectively, in the given data set. With scanning periods of one minute and two minutes in the beginning and the end of the data period, respectively, the offset is about one-and-a-half times the time resolution. The daily delay was calculated based on the formula  $\Delta t = d \times 3s$ , where  $d$  is the number of days since January 6th, and added to the data time. To correct for this effect in the data, the scatter diagrams are shifted to the right relative to the time axis by the calculated daily delay. However since the actual clock behavior is unknown, the extreme scenarios give maximum errors in the determination of correct times. The clock could have suddenly lapsed at one point or another during these months, resulting in the complete five minute deviation from the correct timing from this hypothetical date. The error varies therefore for any date with the upper and lower margins  $[-\Delta t, + (5 \text{ min} - \Delta t)]$ . The error margins should be kept in mind when comparing optical and radar data on time scales of minutes.

### 4.3 Statistics of Aurora and HF Backscatter on Small Scales

In order to understand some of the implications of long-range radar scatter, i.e. sporadic and very variable backscatter pattern, a statistical approach was adopted. It should detect any inherent relationship. To this purpose the total of 41 data days (counting days for the



two CUTLASS locations separately) were brought into a comparable format, to identify common occurrences of backscatter and aurora.

The optical FOVs (allsky camera and MSP separately) were binned into the same cells sizes as the radar cells. The MSP scanning plane in Alaska coincides with the radar beam 1. Figure 4.2 shows the common FOVs of the SuperDARN radar in Kodiak and the MSP and the allsky camera at Poker Flat near Fairbanks overlotted on a map of Alaska. Magnetic north is to the top. The MSP scanning plane at 250 km height is approximately coincident with the beam labeled 1 of the SuperDARN station in Kodiak. The numbering starts with beam 0 in the west. MSP zenith angles in red are used for comparison with the backscatter echoes, the remaining angles are colored black. Also shown, in blue color, is the field-of-view of the allsky camera at an altitude of 110 km. The apparent step in the cell pattern in the vicinity of the radar site shows the transition from *E* to *F* layer scattering with the associated sudden curvature of the wave path. The backscatter grid corresponding to *E*

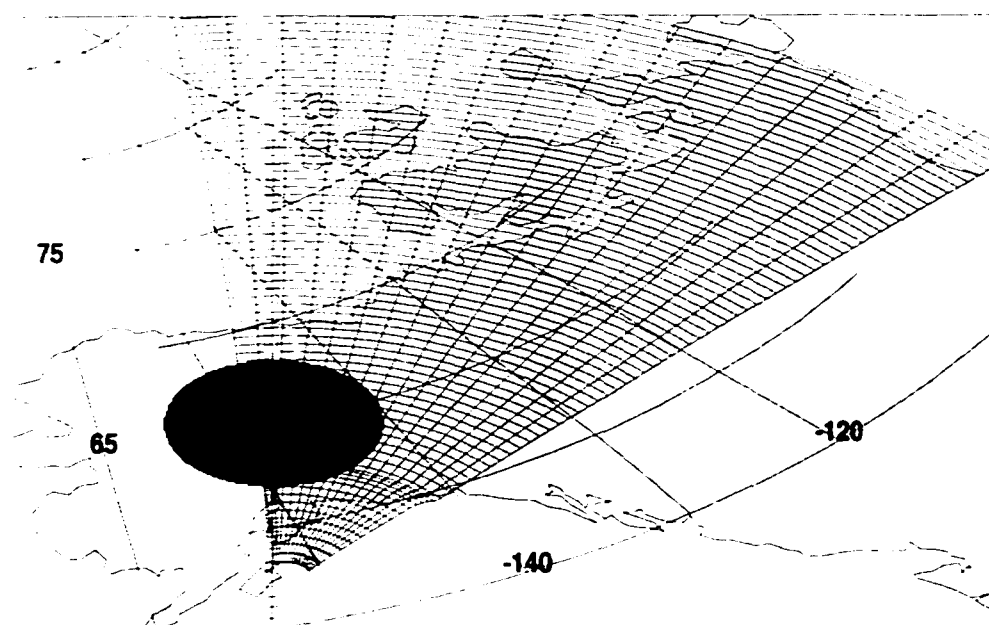


Figure 4.2. FOVs of the SuperDARN Kodiak radar, and the MSP and ASC at Poker Flat. The crosses indicate the scanning plane of the MSP for an altitude of 250 km. The analyzed range of angles, colored in red, coincides with the second beam from left. The ASC FOV in blue color is projected to an altitude of 110 km. Magnetic north is to the top.

layer scatter is mapped to 115 km. backscatter originating in the *F* region is projected to 250 km. Data south of the transition between the *E* and the *F* regions is excluded in the analysis to ensure echoes from the *F* region only, rendering an asymmetric coverage in the MSP angles. The common FOV is defined by radar cell ranges between 13 - 40, with corresponding MSP elevation angles between  $[8^\circ, 139^\circ]$ .

The FOVs of the CUTLASS radars and the optical instruments at the Auroral Station at Longyearbyen, Svalbard, are shown in figure 4.3. The details are analogous to the description of the figure on the previous page. The meridional scanning plane is traced in the radar FOV manually, by determining the cells surrounding the immediate vicinity of the MSP FOV. For Hankasalmi (Pykkvibær) beam numbers 8 - 11 (1 - 11) and cell ranges 26 - 51 (42 - 47) corresponded to the investigated MSP elevation angles between  $20^\circ - 163^\circ$  ( $20^\circ - 159^\circ$ ).

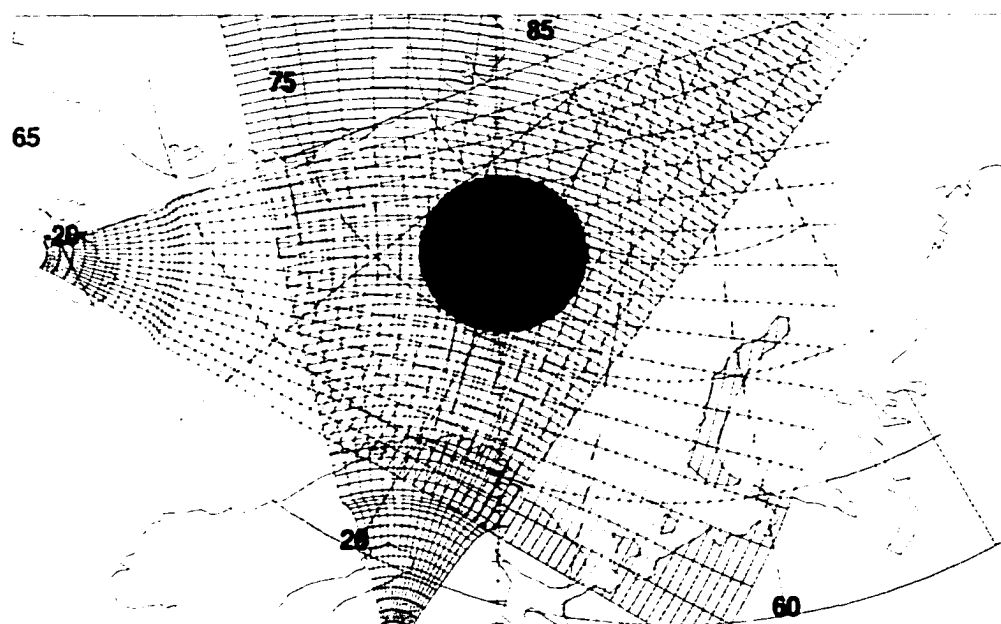


Figure 4.3. FOVs of the Pykkvibær and the Hankasalmi CUTLASS/SuperDARN radars, and the MSP and allsky camera at Longyearbyen. Details as in figure 4.2. Magnetic north is to the top.

The simultaneous use of the two radar sites overlooking a common volume allows for additional information as to irregularity occurrence versus ionospheric propagation conditions. Unfortunately due to the lack of signals in the backscatter pattern the use of this configuration was limited to a few cases.

For the allsky camera the common FOV was determined by comparison of the geographic coordinates of each image pixel and the radar cell. The optical instruments have a higher time resolution and typically several optical pixels correspond to the size of a radar cell. The median of all optical pixels in a cell was taken as the auroral brightness of that cell.

A threshold value was found to define the presence of aurora. This is a possible systematic error source, since this value may not reflect the absolute border between dark sky and even the weakest auroral emission. The problem is less significant in MSP data, since background values, such as moonlight or scattered man-made light, are subtracted automatically. Scattered auroral emissions under hazy conditions, however, cannot be distinguished. Allsky camera images, on the other hand, can contain light pollution, directly or scattered off clouds, due to the moon or city lights of nearby Longyearbyen, for the case of Svalbard data. Polluted images were treated manually. If the light sources could be clearly identified as no aurora, and were spatially confined and not overlapping with aurora, the affected regions were identified in the images and coloured black. The sensitivity of the allsky camera system is dynamically self-adjusting, which complicates the setting of an absolute threshold value. In general, the threshold was set "as low as possible," to pick up weak aurora, but still discard background noise. Variations in the threshold value were tried, the results proved to be fairly consistent if the threshold was not set "unrealistically" low or high, but still was found to correspond to the visible aurora.

Each cell in the common FOV was assigned a backscatter flag (scatter present/scatter not present). Similarly, an auroral flag indicated the presence or absence of aurora. Thus, each cell could have one of four flag combinations: both flags on, backscatter or auroral flag on only, or no flag at all. The latter group was disregarded. Summing up the occurrences of flags for each scan, a large data set was created with three numbers: the numbers of cells containing aurora, but no backscatter, those with backscatter not no aurora, and finally cells with both flags on. Two further groups were formed by summation over two of the variables in this basic set: the total number of auroral, and backscatter cells.

Hourly and daily normalized sums of the five variables were calculated. The data sets radar/MSP and radar/ASC were treated separately. The possible correlation between the groups was determined. Correlation coefficients would indicate whether or not an increase in backscatter occurrence is related in any way to optical aurora. However, the complexity in the data proved too large to give meaningful conclusions. No significance could be ascertained for the calculated correlations. Details of the calculation are described in appendix A. The lack of coherence can be attributed to the contribution of a very variable ionosphere to the observations. As a consequence, the relationship between optical and HF radar aurora cannot be quantified on low spatial resolutions.

A different approach was therefore taken to investigate the relationship between aurora and HF backscatter. The data were analyzed on a mainly case-by-case basis. The complex backscatter patterns could thus be categorized and underlying processes identified. However, to start with an overview over scatter and auroral occurrences, data were averaged to larger spatial and temporal scales.

#### 4.4 Data Sampling on Larger Scales

Pooling some of the data smoothes over the data variability and gives more consistent patterns. This was done for each of the three radar locations. The data intervals were sorted after low and high magnetic activity level, as indicated by the Kp index. For this purpose, the entire radar FOV was binned along magnetic latitudes. This represents a contraction of longitudinal information with the assumption, that structures responsible for backscatter are roughly latitudinally aligned. At two of the radar sites (Kodiak and Hankasalmi) the look direction is roughly north-south aligned. The latitudinal data values were therefore obtained from averaging over data points at the about the same distances to the radar site. For east-west orientation of the look angle of Pykkvibar, it implies that near-range and far-range data points have been contracted to the binned values.

From this generalized approach a positive correlation between magnetic activity and the occurrence and location of radar backscatter is evident. Beginning with data from the site in Alaska, figure 4.4 shows radar and optical data for four nighttime hours on the four days

of low  $K_p$  values between 0 and 2<sup>-</sup>. The upper panel of figure 4.4 displays an average over the power in ionospheric scatter from Kodiak.

It should be noted, that the average of the backscatter values over several days is in fact an average over the decibel values. Strictly speaking, this average is not representative for the average between the underlying signal-to-noise ratios. Averaging over the ratio of signal-to-noise results in relatively high values of averaged decibel. This makes it difficult to distinguish any pattern in the diagrams. The average between 0 dB and 35 dB is 17.5 "dB." Calculating with the signal-to-noise ratio, the result would be 32 dB. The choice to average over dB implies therefore an underrepresentation of the true averaged power, but it improves the readability of the diagrams.

The characteristic feature in the upper panel of the image is a band of backscatter between 08:30 UT and the end of the interval with minimum and maximum extensions of 64° and 74° magnetic latitude respectively and a slightly offset center at around 68°. Outside the clearly defined band there is remarkably low intensity, at most places just around or below the noise level. In addition there is a backscatter region around 80° prior to 09:00 UT, which has no correspondence in the optical observations. Particular structures in the diagrams are the result of the average over a small number of days only.

In the lower panel are the Poker Flat MSP records for the same days and time interval, binned in a similar way. Comparing the meridionally oriented FOV of the optical instrument with the latitudinally sorted radar data implies the assumption that the optical aurora is part of east-west aligned larger features. For any given case this might not be true, as the emissions could be part of a folded band, could be confined to a relatively small area, or could have a different orientation. This uncertainty is only partly overcome by averaging over several days. These MSP keograms take advantage of nearly the full range of the 181 angles from horizon to horizon (0°- 168°). The extreme latitudes are therefore quite distorted. The difference from overhead emission is clear when comparing the appearance of arcs around the station latitude of 65.4° with other latitudes. Averaging over a number of days as low as four represents a quite limited sample in a statistical sense. Single days or features are likely to dominate in the image.

The auroral brightness is visible in a band with variable latitudinal width, between 66°- 74°. This coincides roughly with what would be expected for location and width of

the auroral oval. Under quiet conditions the auroral oval is narrower and centered further poleward than during active periods. Average center and midnight latitudinal width of the oval for quiet periods are at  $71^\circ$  N cgm and  $\pm 1^\circ$  degree, respectively, while it is at  $68^\circ$  N cgm extending  $3^\circ$  in both directions during moderately disturbed times [Feldstein and Starkov, 1967]. The statistical auroral oval, the longterm auroral occurrence frequency distribution in geomagnetic time-invariant latitude coordinates, reflects the location and the extent of auroral precipitation. This includes soft sub-kiloelectronvolt precipitation and the inverted V structures associated with auroral substorm activity.

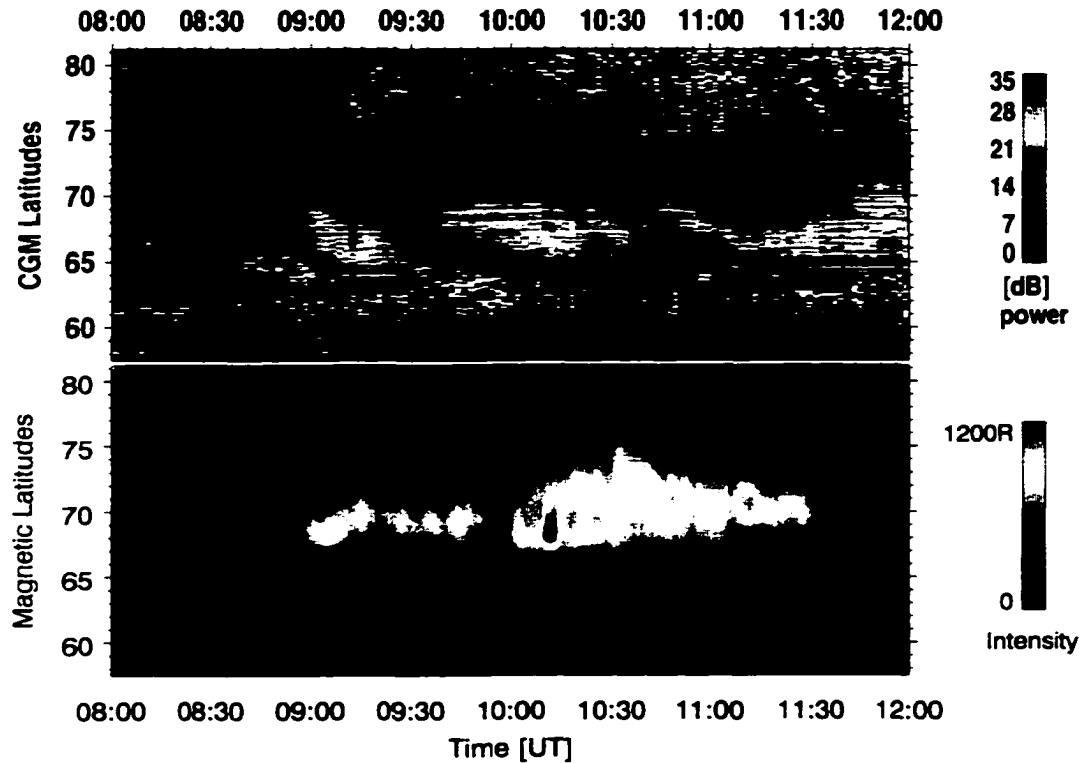


Figure 4.4. Four day averages of SD Kodiak (upper panel) and Poker Flat MSP data (lower panel) for  $K_p$  values between 0 and  $2^-$ . Magnetic midnight at Poker Flat is at 11:10 UT. Zenith in the MSP keogram is at  $65.4^\circ$ .

The region of enhanced backscatter between  $65^\circ$  and  $70^\circ$  is displaced slightly equatorward with respect to the optical aurora. Higher higher signal strengths are found at lower

latitudes. This agrees with the statistical findings of *Möller* [1974] (cf. chapter 2.4), who described a steep increase in irregularities poleward of the equatorward boundary of the auroral oval.

The same binning of HF backscattered power and MSP data for high Kp values can be seen in figure 4.5. The upper panel shows the backscattered power on the four days with the highest available Kp indices between 3 and 5<sup>-</sup>. Days with Kp indices in between these and the low values were omitted to emphasize the implication of a disturbed versus non-disturbed ionosphere. The backscatter region stretches here from 62° to 76° cgm latitude, with the center of the solid scatter block and the highest powers at 67°. On the poleward side the scatter incidences are at a lower level than for more quiet conditions. Enhanced auroral fluxes cause an increase in ionospheric densities. Radar rays are more refracted for

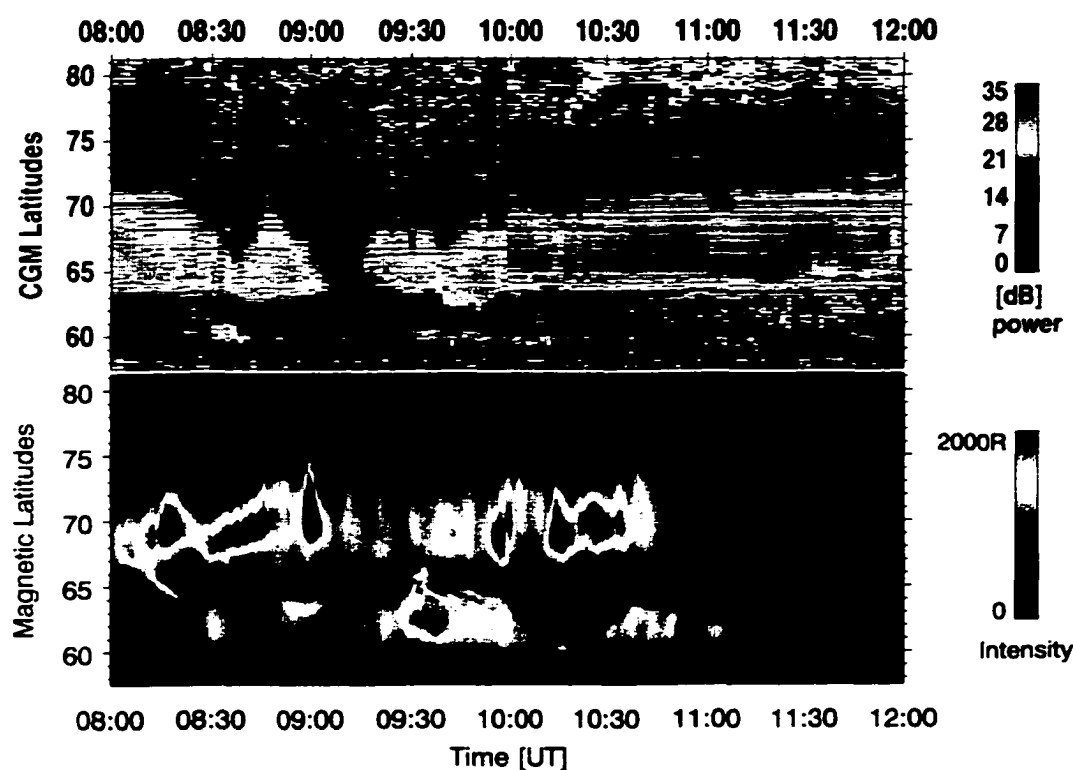


Figure 4.5. Four day averages of SD Kodiak (upper panel) and Poker Flat MSP data (lower panel) for Kp values between 3 and 5<sup>-</sup>.

higher electron concentrations. The range, where the beam is orthogonal to the magnetic field is therefore closer to the radar site. Consequently, the chance to receive far range backscatter is smaller for higher ionospheric densities. At  $60^\circ$  latitudes a narrow backscatter stripe can be seen. It is barely visible on quiet days. It originates in the  $E$  region close to the radar site, where high-energy precipitation of the diffuse auroral oval ionizes at lower altitudes.

The MSP keogram (lower panel) displays active aurora extending south of the zenith to latitudes below  $62^\circ$ . Single intensifications and arcs dominate the superimposed intervals. Noteworthy in the comparison between intensity of scatter and aurora is that while for the days in question the auroral activity ceases already around 11 UT, the power in the echoes continues to show elevated values through the end of the period. This is partly artificial, because on two occasions MSP records ended earlier than the end of the time interval shown. This can be seen in the sharp decreases in brightness at 11:15 UT and 11:35 UT. It might also point to irregularity processes unrelated to auroral precipitation.

The Northern Europe data set is introduced by the observations under quiet magnetic conditions, see figure 4.6. The six occasions with the lower Kp values among common days between Hankasalmi and Pykkvibær have indices between 0 and 1<sup>-</sup>. The upper panel shows the average over Hankasalmi data, the middle panel has the corresponding days for Pykkvibær. In the lower panel, the MSP keogram is shows auroral emissions concentrated at latitudes between  $62^\circ$  to  $73^\circ$ , with the center at  $68^\circ$ .

In the Hankasalmi data (upper panel), the scatter belt is centered at around  $69^\circ$ , extending  $2^\circ$  -  $3^\circ$  to both directions in latitude. This conforms approximately with the locations in figure 4.4 above, the smaller dimensions probably a reflection of the different solar activity level. Modelled ionospheric nighttime densities indicate a more than 4-fold increase in electron concentrations between winter equinox in 1997 and 2000 [*Bilitza*, 1995]. Although the identical days contributed to the diagram for Pykkvibær (middle panel), the result is quite different. Here the scatter spreads over a wide range between  $65^\circ$  -  $77^\circ$ , with generally low power levels and a sharp increase in scatter occurrence at  $65^\circ$ . A significant difference between this projection for Pykkvibær versus for Kodiak and Hankasalmi is the zonal orientation of the radar look-angle and orientation of the FOV. The steep threshold in the Pykkvibær data at  $65^\circ$  is explained by the fact that below that latitude only very



few low-latitude long-range cells contribute to the image. They have generally very low backscatter occurrences due to the long path lengths. At around  $65^\circ$ , a large quantity of contributing cells from middle to near-range are mapped to the resulting meridional scan.

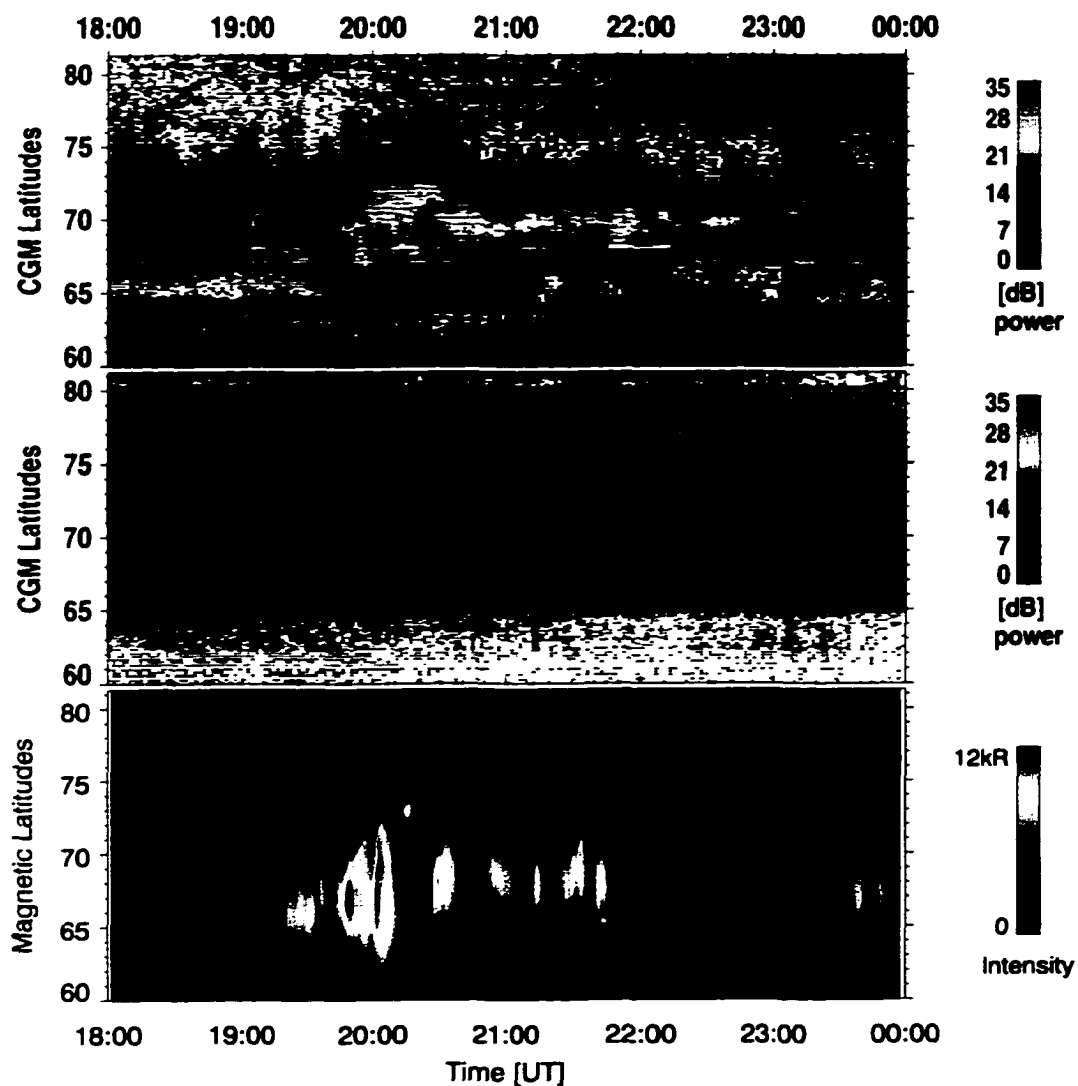


Figure 4.6. Six day averages of CUTLASS Hankasalmi (upper panel), Pykkvibær (middle panel), and MSP Longyearbyen data (lower panel) with  $K_p$  values between 0 and  $1^+$ . Magnetic midnight at Longyearbyen (at  $75.1^\circ$ ) is at 20:40 UT.

Another aspect of this east-west alignment is the pooling of long-distance scatter events with those close to the radar site. Long-range scatter tends to have lower power in the backscatter than close-range echoes. This arises mainly from the  $1/r^2$  dependency of the radar power flux. The diagrams in figure 4.6 indicate therefore that the averaged value of near- and far-range backscatter does not change significantly for the magnetic conditions in question.

The moderately disturbed days in the CUTLASS/Longyearbyen set are shown in figure 4.7. Four days were sampled, with Kp values between 2 and 4<sup>-</sup>. Days with mixed indices between this group and the quiet days were excluded. The optical aurora in the lower panel hardly expands northward of the zenith at 75.12°. The auroral activity can therefore truly be described as moderate. However, the range of latitudes where aurora appears is slightly extended and the emission intensities are higher than under the quiet conditions in figure 4.6. In the upper panel, showing Hankasalmi data, the scatter curtain is slightly displaced at 68° with respect to quiet days, but without the increase in latitudinal spread, as was noticeable in the Kodiak observations. A clear distinction between the quiet (cf. 4.6, upper panel) and the moderately disturbed conditions is that although the power in the scattered echoes increases, the occurrence of scatter decreases under the latter circumstances. A noticeable scatter dropout occurred between 20:50 UT and 21:30 UT. It coincides with stronger auroral brightness in the MSP panel. Possible processes will be discussed in the sections below. In the Pykkvibær data, in the middle panel, higher power occurs at lower latitudes and the equatorward boundary is better defined during these moderately disturbed days, than under the quiet conditions of the previous figure. Apart from those few minor differences between the two disturbance levels, it is not possible to assign an echo pattern to a certain disturbance level. This represents a completely different picture than for the other two HF radars. Averaging over the higher scattered powers closer to the radar site and the low-power far ranges is likely the reason for this. Data for zonal look-directions are apparently not well suited for this kind of averaged projection.

For an orientation roughly perpendicular to the auroral oval, as for Kodiak and Hankasalmi, there is a general correspondence between auroral locations and the probability of receiving backscatter from approximately the same locations. This tendency is likely strongly enhanced for a larger data set than the presented days. The observed occasional

scatter dropouts and single features would then be statistically distributed and therefore expected to be weighted less. However, the trend of higher echo power and extended and more equatorward scatter regions during active periods, and vice versa for quiet times, is already visible in this small set.

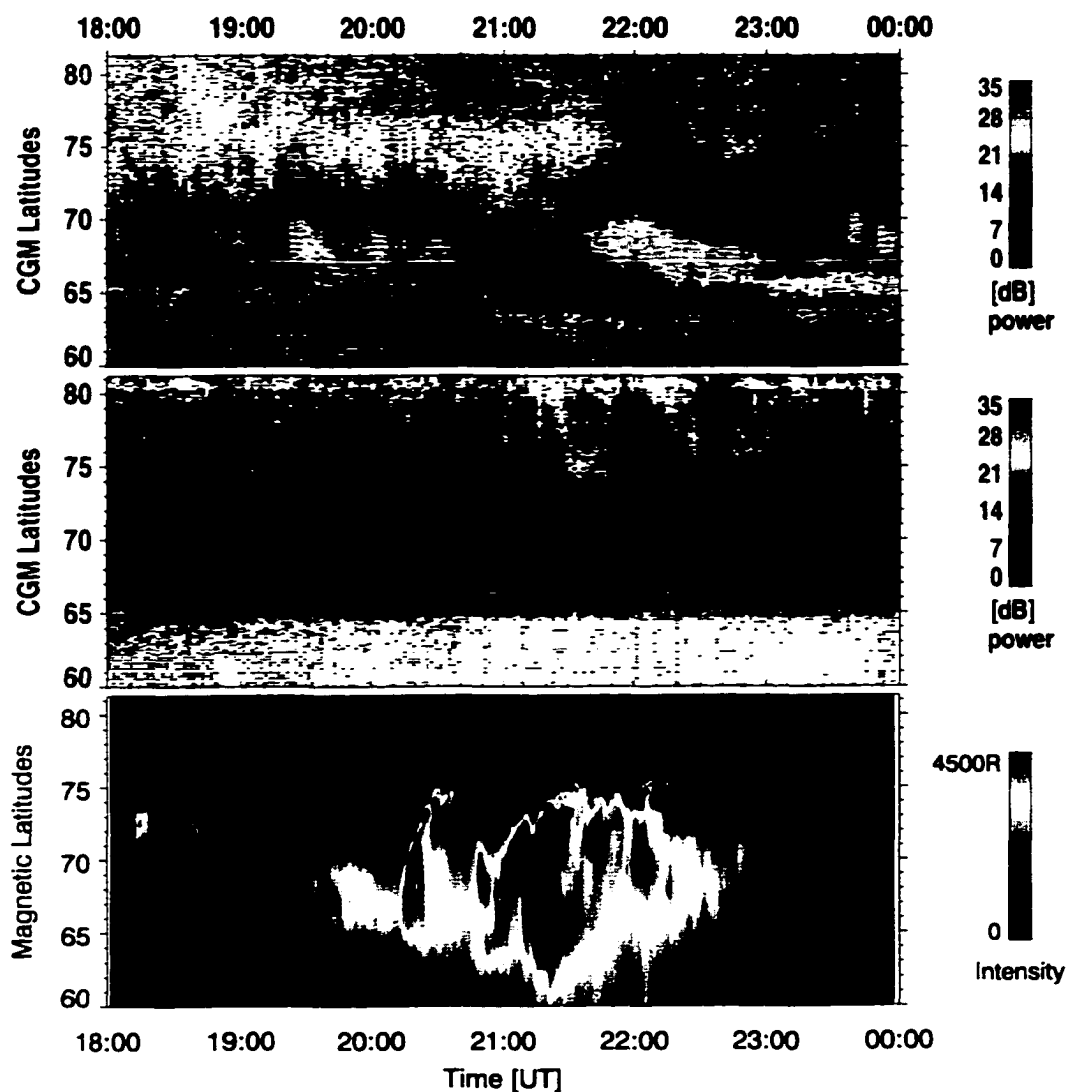


Figure 4.7. Four day averages of CUTLASS Hankasalmi (upper panel), Pykkvibær (middle panel), and MSP Longyearbyen data (lower panel) with Kp values between 2 and 4<sup>+</sup>.

## 4.5 Aspects of the Small-scale Relationships Between Optical and HF Aurora

In the following, the emphasis will be put on the connection between scatter and aurora on the basis of single events. Positive correlations and the occurrence of scatter dropouts for intense aurora are indications of mechanisms that will be investigated and described in the sections below. The complexity of the relationship between HF radar scatter and optical aurora is due to several factors that determine whether or not backscatter will arise from any given location. They include favorable propagation conditions for the radar signal. This implies lack of absorption and favorable ray refraction from the transmission site to the volume with irregularities. The irregularities have to have sufficiently sharp density gradients and the right dimensions for the HF signal. Furthermore, the radio wave vector and the normal of the irregularity boundary must be close to orthogonality for the wave to be scattered back to the receiver. Combined, these effects render a broad spectrum of backscatter patterns even for seemingly similar ionospheric conditions. An attempt is made to structure this spectrum with a start at quiet ionospheric conditions and introducing more perturbations later. The purpose of this analysis is not to explain all phenomena occurring during the time intervals shown, but rather to concentrate on certain aspects that illustrate the current discussion.

### 4.5.1 Aurora-induced Backscatter in Quiet Times

The relation between aurora and scatter is not as close on the basis small spatial and temporal resolution as it is in terms of scatter occurrence for different levels of perturbation. This leads to the question: What determines the presence of backscatter in an auroral feature? Toward answering this we will investigate what happens, in terms of irregularities, after a precipitation onset. Consider for the moment a homogeneous ionosphere with sufficiently high densities to enable  $F$  region probing, but not too high to blanket the  $F$  region, and the onset of a particle beam with low energies to minimize effects in the  $E$  region below. Precipitation of low-energy ( $\leq 1$  keV) particles ionizes mainly in the  $F$  region volume. Diffusion and recombination are counteracting the localized increases in plasma density. The processes are slow compared to the auroral ionization and a significant increase in  $F$  region

densities can happen on the order of one minute or less. A quick estimate shows the validity of this statement:

As a lower limit for a possible precipitation assume a downward directed electron flux of  $10^9$  electrons/(cm<sup>2</sup>s) with a monoenergetic energy of 100 eV. Most of the deposited energy for particle energies of 100 eV and lower is between 300-400 km [*Mantas and Walker, 1976*]. *Mantas and Walker* considered various loss processes, arriving at a higher value than the 35 eV per ionization event given by *Rees* [1988]. They conclude that each incoming 100 eV electron produces 1.71 thermal electrons. Taking, for simplicity's sake, the 100 km vertical slab to be uniformly affected, the ionization rate per second will be 171 electrons/cm<sup>-3</sup>. During one minute of ongoing flux, the charge concentration is raised by about  $10^4$  cm<sup>-3</sup> electron-ion pairs, a considerable fraction of the total *F* region plasma density ( $\sim 10^5$  cm<sup>-3</sup>).

Primary structure due to the spatial shape of the precipitation region is likely in the large ( $\geq 10$  km) wavelength range. The likelihood of unstable configurations can be assessed by the taking a look at the typical midnight scenario. At high latitudes, conditions favoring instabilities involving the  $\mathbf{E} \times \mathbf{B}$  drift are often found. Drifts, electric fields, and field-aligned currents in a non-equilibrium environment all contribute to the appearance of instabilities such as the generalized gradient drift instability (see chapter 2.5.3). In the presence of structured auroral precipitation, a region with enhanced plasma densities forms with the same spatial extensions. The zonal alignment of the auroral oval results in meridional density gradients. The gradients are equatorward at the poleward boundary and poleward at the equatorward boundary. The cross-polar flow of plasma emerges into the nightside throat of the convection pattern at auroral latitudes around magnetic local midnight and has a large equatorward component. This represents a potentially unstable situation at the poleward edge of the density enhancement with its equatorward density gradient. The ionospheric electric field in the premidnight and midnight region is usually large and westward [*Kamide and Kokubun, 1996*]. A perturbation at the unstable poleward boundary leads to the setup of small-scale electric fields favoring the growth of the perturbation amplitudes, as already discussed in chapter 2. The presence of field-aligned currents increases the instability growth rate further. A sufficiently large current density can also destabilize the equatorward border.  $\mathbf{E} \times \mathbf{B}$  drift type instabilities with or without the involvement of Birkeland currents act to shorten the minimum irregularity scale length present within minutes [*Roble and Rees,*

1977; Vickrey *et al.*, 1980]. Conditions for further plasma structuring into decameter scales through the ion-cyclotron instability can be found in differential plasma drifts in field-aligned currents. Soft continuous precipitation in a quiet ionosphere is therefore likely to produce irregularities which can be seen as radar echoes. An example for this process is presented in figure 4.8.

This compound diagram shows in the upper panel the Kodiak HF backscattered power along egn latitudes during three premidnight hours on March 3, 2000. Groundscatter is shaded grey. In the middle panel Poker Flat MSP intensity records of two auroral emissions are superimposed. The red color represents the auroral line at 630 nm, aurora at the 427.8 nm band is colored blue. Brightness in both channels simultaneously results in shades of magenta. The simultaneous display of the auroral lines indicates the height distribution of the auroral emissions, and therefore provides an indication of the relative energy of the incoming particles throughout the interval. The emissions are mapped to the altitudes from which they are assumed to originate, 250 km and 110 km respectively, and are displayed in the resulting magnetic latitudes. Red color indicates emissions at high altitudes, while purple and blue indicates aurora at lower altitudes. The range of  $63^{\circ}$ -  $75^{\circ}$  degrees represents ground distances of 685 - 2020 km to the radar site.

The lowest panel contains information extracted from the two upper panels. Its purpose is to give a simplified overview of the quantity of backscatter in the presence of *F* region aurora. The dashed line represents the sum for each scan over the number of cells with backscatter values in the scatter diagram. Only ionospheric backscatter is taken into account; groundscatter is omitted from the summation. This may skew the result in the presence of enhanced groundscatter occurrence, giving the impression of little scatter. In reality, ionospheric backscatter might be overshadowed by the presence of groundscatter. The sum over corresponding cells with aurora is indicated by the solid line. The binning of the optical emission into discrete values was described in the section 4.3. The threshold defining the presence of aurora is set to a value varying with intensity for each day, here 500 R. Under hazy conditions, this value may be higher to account for the presence of scattered light. The threshold is indicated in the upper right corner of the plot. The result is fairly robust to changes in the threshold value, since only the relative fluctuation of aurora is the information sought after in this context. The summation plot serves as an attempt to

quantify the apparent correlation between the two upper plots. It shows that the occurrence of backscatter increases simultaneously with the latitudinal spread of auroral emissions. In the summation no weight is given to the intensity of either aurora or scatter.

The nighttime of March 3 was characterized by quiet magnetic conditions. Kp values were 0<sup>+</sup> and 1 for the two 3-hour intervals falling into the period between 8 - 11 UT. The number of hours, as in examples below, represents the minimum time for overlapping data coverage in radar and optical measurements. The radar echoes show a good correspondence of scatter and optical aurora in both location and intensity. The low-intensity vertical scatter streaks occurring occasionally are due to external noise. They may be eliminated by the standard SuperDARN median filtering. The scatter diagrams shown in the present analyses are unfiltered to avoid blurring small-scale information. The apparent southern boundary in the red emission is likely a true southern limit rather than the upper part of rays at higher latitudes. It is well defined and relatively sharp, even more so than the gradient in the brightness at higher latitudes. The equatorward auroral boundary follows in this case a relatively straight line, starting at 69° at the beginning of the interval to 67° at the intensification at 10:00 UT, thereafter it is constant at 66°. The backscatter originates poleward of the equatorward soft diffuse auroral boundary. During the more intense precipitation the echo pattern continues the equatorward expansion.

The correspondence between aurora and radar scatter is not as clear for the first hour since the occurrence of groundscatter contaminated the reception of the likely weaker ionospheric scatter. Due to the spread in beam elevation angles, different ray paths are possible at the same time. The travel time can coincide for a 1E groundscatter and a 1/2 F ionospheric signal scattering at about the same radial distances from the radar. Higher signal strength in the groundscatter echo than in the ionospheric backscatter may therefore result in the final cell value to be defined by properties describing groundscatter (low velocities, low spectral width). The groundscatter is part of the diurnal U-shaped scatter traces seen in the daily scatter overview in figure 4.1. The few sprinkled low power echoes amidst the more powerful ground scatter (the signal power in the groundscatter is not shown here) support this explanation. Backscatter powers increase later in the interval with the start of increased values preceding the optical intensification. Signal strength of 35 dB and higher compared to the noise level are found equatorward of the brightest aurora in the red and

the blue channels. However, due to the ambiguity in the interpretation, the interval with groundscatter occurrence should not be weighted in the analysis.

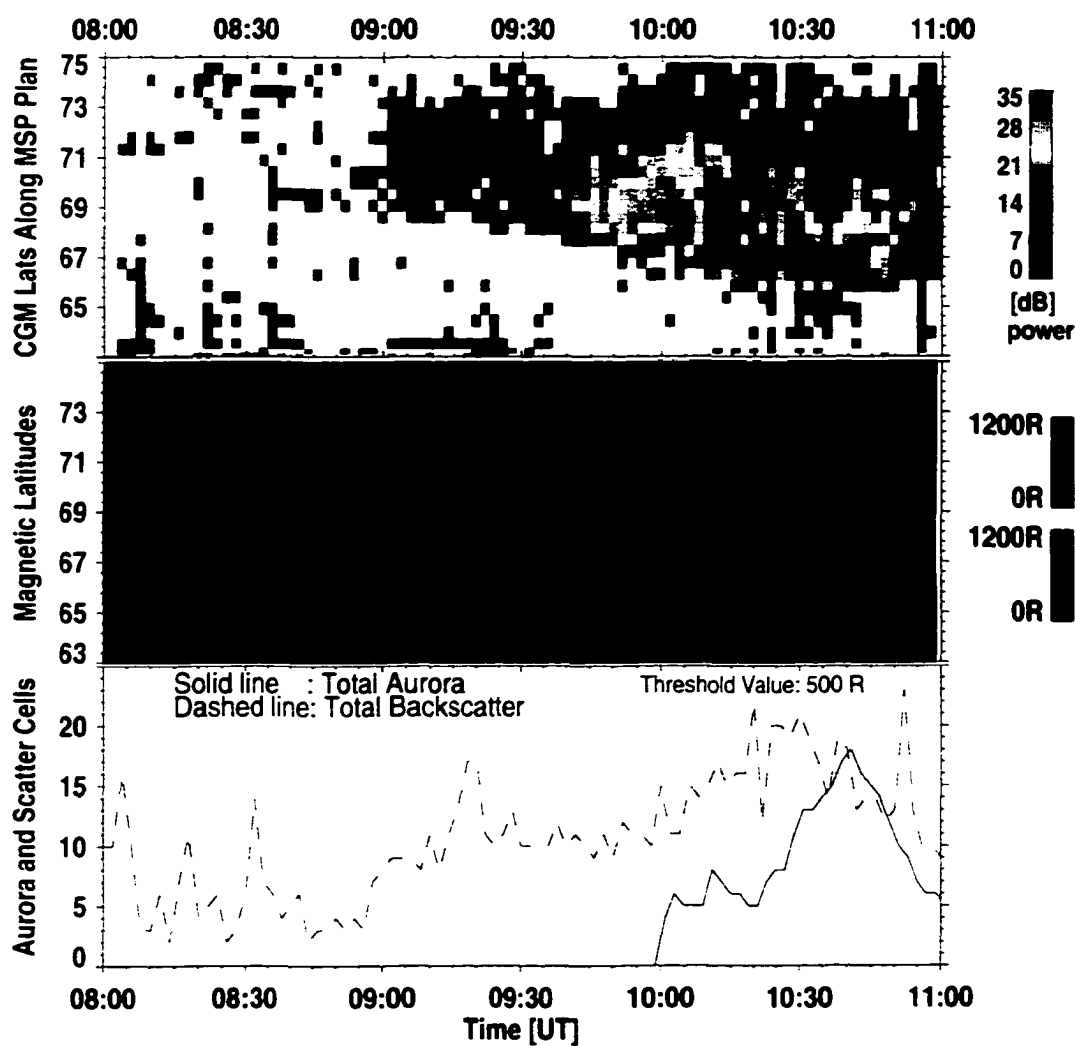


Figure 4.8. Kodiak backscatter (upper panel), Poker Flat MSP auroral brightness (middle panel) for 630 nm (red color) and 427.8 nm (blue color), and the total number of scatter and auroral cells in the MSP scanning plane (lower panel) on March 3, 2000. Zenith in the MSP keogram is at  $65.41^\circ$  N cgm. Magnetic midnight at Poker Flat is at 11:10 UT.

The softness of the flux in the first part of the interval is indicated by the large ratio of the red-to-blue auroral brightnesses. Figure 4.9 displays the ratio of these brightnesses



as a function of time. The total brightness per wavelength is formed by summing over the brightnesses at all MSP elevation angles over the entire sky. This simplification is based on the assumption that the broad emission seen is due to a single and homogeneous feature. In the general case, this assumption is not valid, nor is it here for the auroral arc entering the FOV at 10:30 UT.

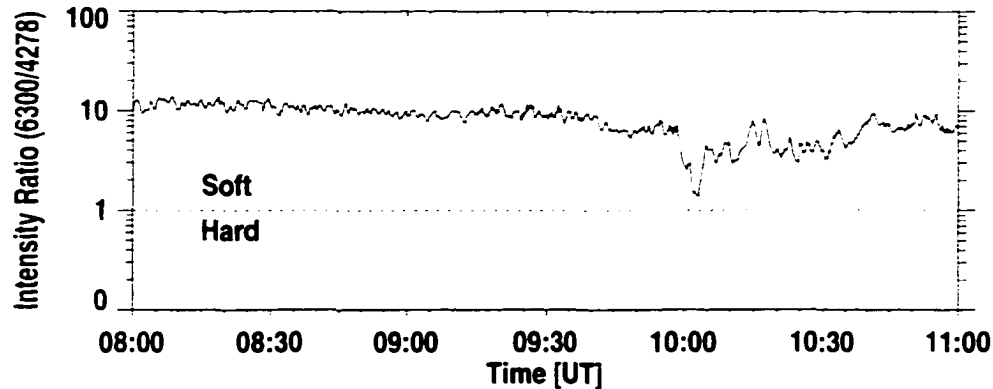


Figure 4.9. Ratio of the red and blue emissions on March 3, 2000.

Theoretically, it is always possible that an ionospheric structure is drifting into the radar view rather than being created locally. This implies that the mechanisms rendering the configuration unstable have to either drift along with the structure or dominate a larger region including the moving plasma. The short life times of decameter irregularities require a continuous production while backscatter echoes are being observed. A check with the line-of-sight Doppler velocities during that interval (not shown) asserts that, while there are some patches with enhanced radial velocities towards the radar within the large region of backscatter, they are embedded in a low background drift, indicating that the latitudinal development of that region is not due to an equatorward convection of pre-existing forms, but a local formation of irregularities.

The direct response of this particular HF echo pattern to processes associated with aurora is likely based on the fact that, through low energy precipitation, the ionization is restricted to the *F* region. The *E* region does not interfere in the generation and detection of *F* region irregularities in this case, neither by blanketing nor by high conductivities. The

50 MHz VHF auroral radar in Elmendorf near Anchorage, Alaska. (cgm 60.98 N. 264.50 E), serves as an indicator of a perturbed  $E$  layer. It records coherently backscattered echoes from 3-meter irregularities in the  $E$  region from an azimuthally narrow FOV along the Poker Flat meridian. The positive correlation between  $E$  region radar backscatter and optical aurora has been repeatedly described in the literature [e.g., Romick *et al.*, 1974; Waldock and Jones, 1985]. A collocation of radar echoes with the auroral electrojet currents was pointed out by Greenwald *et al.* [1975].

The VHF radar echoes for this date are shown in figure 4.10. The latitudinal interval in this diagram is smaller than in previous figures, because of the more limited coverage by this radar, compared to the HF radar. The original web-accessible VHF diagrams (<http://gedds.pfrr.alaska.edu/HLMS/vhf.htm>) indicate three geographic locations along the ray path instead of the magnetic latitudes shown in figure 4.10. The magnetic latitudes were obtained through linear interpolation between these three geographic locations. The time interval was chosen to match the current data period. The first scatter appeared at 10:00 UT at 68°, in the equatorward portion of the auroral emissions. The diagram indicates a very quiet  $E$  region lacking irregularities in the meter-sized domain prior to the detection of the first irregularities at that time.

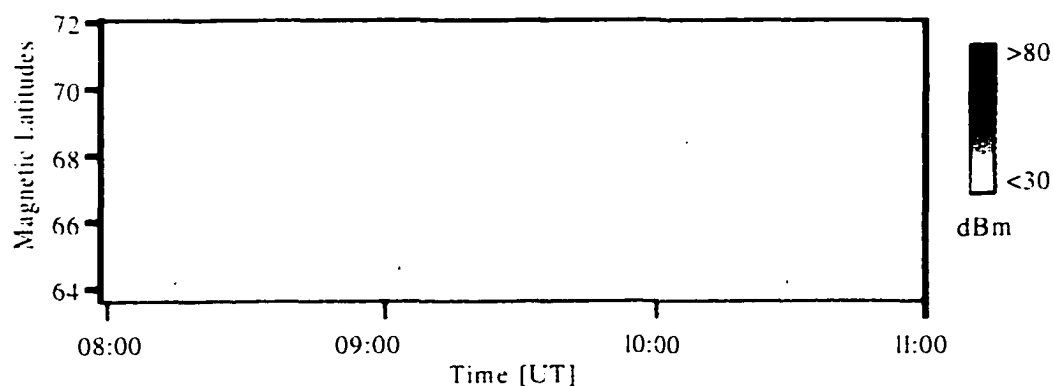


Figure 4.10.  $E$  region radar aurora from the Elmendorf 50 MHz coherent scatter radar on March, 3 2000.

The backscatter in the Kodiak scatter diagram are therefore very likely an indication of irregularities and instability processes which are innate to the  $F$  region. Optical aurora and  $F$  region HF irregularity detection are positively correlated during such conditions.

#### 4.5.2 Irregularity Growth

The auroral emissions in the example above were from soft precipitation and diffuse and without much structure. If aurora is the determining factor in the generation and/or detection of ionospheric irregularities, then structure in auroral features could be expected to be reflected in the radar echoes. Auroral arcs represent areas of downward particle flux, implying ionization and field-aligned currents at the same spatial scales. Inward density gradients at the borders of the arcs in an unstable configuration would lead then to a cascade to smaller irregularities. Thus auroral arcs are likely to entail small-scale ionospheric structure which can be sensed by orthogonally incident radar beams. The time between the onset of the formation of a primary structure until smaller wavelength regimes are populated is dictated by the stability of the situation.

Single arcs can be discerned at or near the zenith on February 24, 2000. Figure 4.11 shows, in the same format as previous figures, from top to bottom, backscatter intensity, the red and blue auroral emissions and the total occurrence of backscatter. Added to the upper two panels is a line which represents the lower border of the poleward red aurora, mapped to an altitude of 200 km. The line is yellow on the MSP keogram and is plotted in stars over the scatter diagram. The lower border is determined by a fixed brightness value for aurora, which is searched in the keogram from the poleward side. Its value is the same as the threshold brightness used for the lower panel, printed there in the upper right corner. The lines are discontinuous where the threshold value was not found in the keogram. The magnetic conditions during this 2 hour interval indicate relatively active disturbances with Kp indices of 4<sup>-</sup> and 5<sup>-</sup> for the first and second hour, respectively.

Red auroral arcs repeatedly moved equatorward during the first hour of the period. The scatter diagram also shows equatorward developing echo patterns, with a varying level of apparent association with the optical traces. For direct comparison between the two upper panels, the most intense of the equatorward moving features, between 08:00 - 08:15 UT, is emphasized with a white line in the middle panel. The same solid line is added to the

upper panel. The additional dashed line in the scatter diagram is placed 4 minutes later. It happens to also trace the apparent equatorward movement of increased backscatter power, thus indicating the time delay in the scatter response. The larger deviation at later times might be an effect of the Doppler velocities away (-250 m/s) and towards (100 m/s) the radar site in the beginning and the end, respectively, of the auroral arc motion (not shown). This probably resulted in a slight eastward rotation of the plasma with respect to the line of sight of the radar beam. Ideally the two-dimensional information about the convection pattern, which is not available for this case, should be consulted to determine zonal plasma motion. The error for the determined 4 minutes due to uncertainty in the determination of the solid line in the middle panel is estimated to be  $\pm 30$  seconds. This error adds to the possible timing error described in the end of section 4.2.

Other equatorward moving auroral arcs were too weak and close to each other so that an association between optical and radar data is difficult. Additionally, a radar frequency change occurred twice during that interval (cf. the all-day scatter diagram for this day in figure 4.1). Its impact on this echo pattern is hard to assess. A switch to higher frequencies (13 MHz) occurred at 08:22 UT and back to 10 MHz at 08:38 UT. A closer correlation between auroral and scatter structures at a later point is therefore not attempted.

The time delay between the auroral arc and the intensification of backscatter power likely reflects the time required for the generation of decameter irregularities following the precipitation onset. There are no comparable observational cases for decameter irregularities to study. *Vickrey et al.* [1980] found a time difference of  $\leq 6$  minutes between  $F$  region density enhancements and the occurrence of scintillations due to kilometer-sized irregularities. The time was interpreted as instability growth time, based on the generalized  $\mathbf{E} \times \mathbf{B}$  instabilities. The kilometer-sized irregularities reported by *Basu et al.* [1983] and *Kelley et al.* [1980], which were observed to form within 1 - 2 minutes after a precipitation-induced density enhancement, were likely due to structure in the downward fluxes. In general, the time between the onset of precipitation and the generation and detection of irregularities with the appropriate small wavelengths certainly depends on the scale of the precipitation region, the density and energy of the particle flux, as well as the prior conditioning of the ionosphere. In this case of a magnetically disturbed night time,  $F$  region ionization started

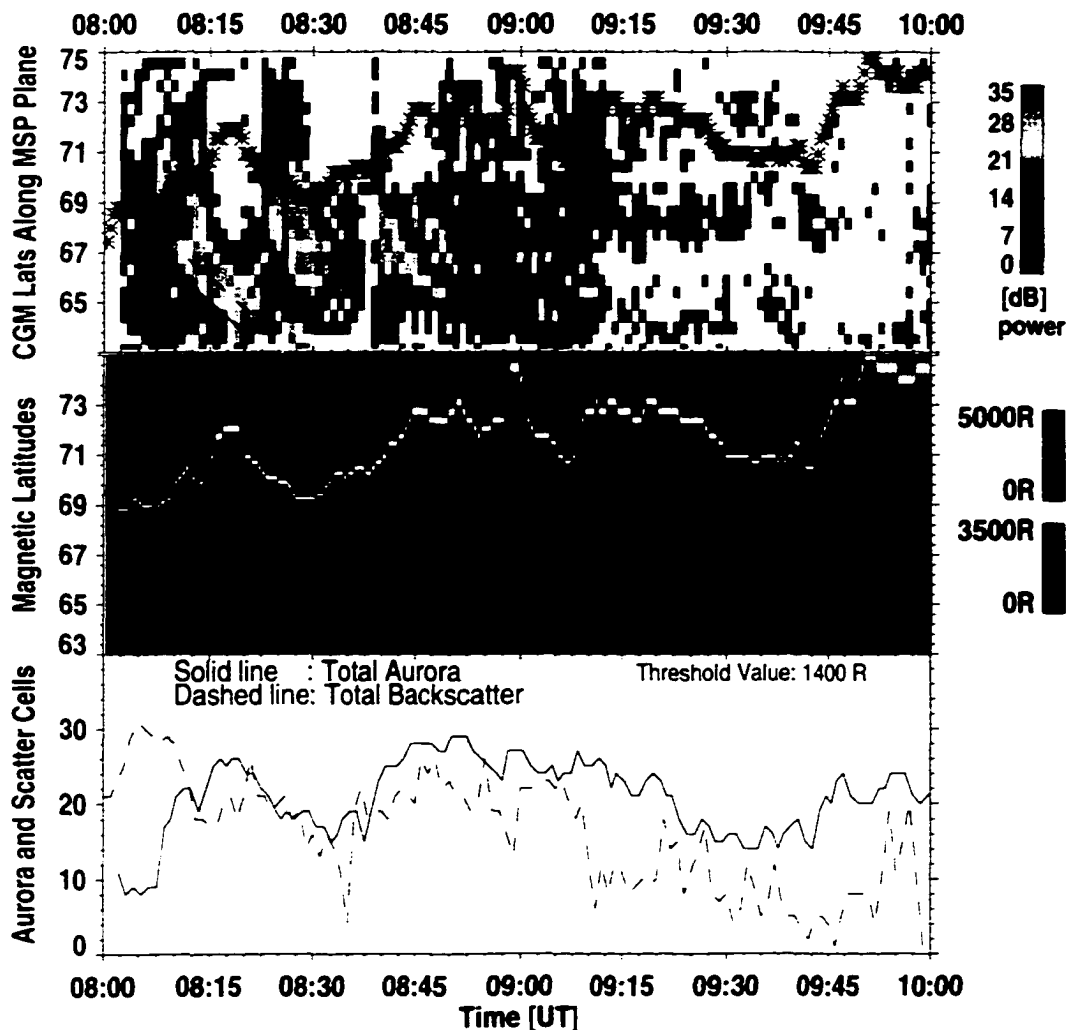


Figure 4.11. Alaskan observations in the same format as in figure 4.8. for February 24, 2000. The crosses (upper panel) and yellow line (middle panel) show the position of the lower border of the red aurora mapped to an altitude of 200 km. The superimposed short lines between 08:00 UT and 08:15 UT are explained in the text.

well before the beginning of the interval at 8 UT. The diagram for the entire day (figure 4.1) shows ionospheric backscatter echoes prior to 05:00 UT, indicating the prolonged presence of ionospheric density irregularities. Thus instability mechanisms generating decameter-scale irregularities have been in place for an extended period and might merely be intensified by processes associated with the equatorward moving arcs. The role of aurora on this occasion

might not have been to provide increased densities, but to destabilize existing structures further.

### 4.5.3 Insufficient Ray Refraction through Low Ionospheric Densities

If ionospheric conditions are not suitable for both radio propagation and irregularity detection, as in the two previous examples, precipitation onset and scatter response can generally not be brought into a clear relationship. Radio waves at frequencies at or above 10 MHz can experience very little refraction in a low-density ionosphere and consequently transverse the  $F_2$  peak density, and escape the ionosphere without reaching orthogonality with the magnetic field.

An example of very calm ionospheric conditions was seen on February 8, 2000 (figure 4.12). The backscatter occurrence level for the four hours was relatively low. Apart from the large-scale backscatter region in the second part of the interval, there were a few echoes spread throughout the period. Despite Kp indices of 2<sup>-</sup> and 3<sup>-</sup> for this interval, local magnetometers as well as the high-latitude magnetic perturbation index, AE, indicated a magnetically extremely quiet time prior to the auroral intensification at 10:20 UT. The characteristic U-shaped groundscatter pattern on the all-day scatter diagram (not shown) indicated a relatively early retraction of the postmidday groundscatter, a sign for rapid decay of ionospheric densities. Ionosonde measurements at Gakona (not shown) found peak  $F_2$  ionospheric densities between  $6.6 \times 10^4$  -  $1.2 \times 10^5$  cm<sup>-3</sup> prior to and during the first half of the interval. Gakona is located in Alaska at 63.1° cgm N, 92.4° cgm W. Ionosonde data are accessible under <http://maestro.haarp.alaska.edu/cgi-bin/digisonde/scaled.cgi>.

The equatorward expansion of the initially predominantly red auroral oval in the first half of the period is similar to the situation of March 3 (figure 4.8, p.75), though at somewhat higher intensity levels. However, on February 8, the scatter occurrence was quite reduced compared to March 3. At 10:15 UT, the aurora brightened and expanded poleward broadening the luminous region in the MSP keogram. The intense and widespread scatter appeared some 18 minutes later. It originated at latitudes comparable to the expanded aurora. The spatial and temporal coincidence and the chronology of aurora and scatter make it appear likely that there is a causal relationship between the two phenomena.

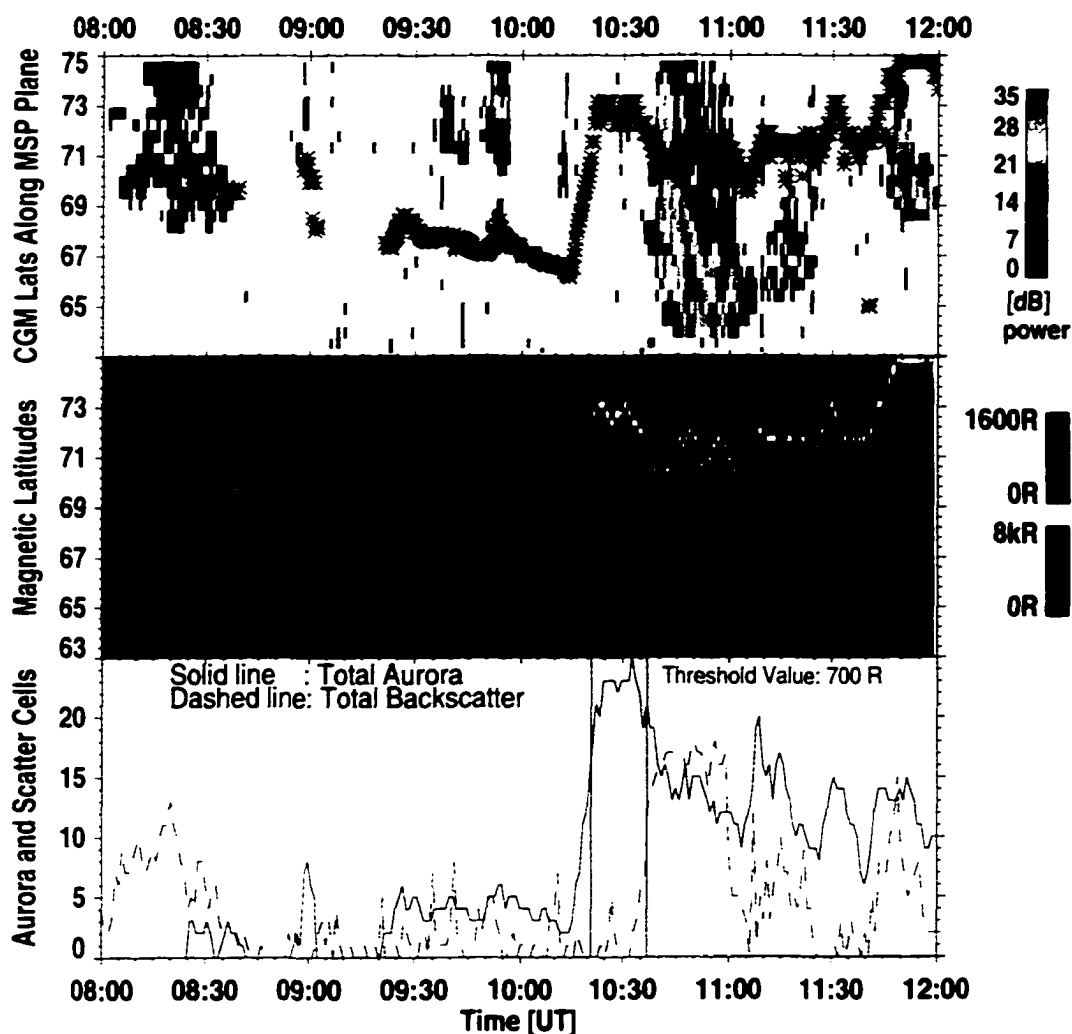


Figure 4.12. Alaskan observations in the same format as in figure 4.8, for February 8, 2000. The vertical lines in the lower panel indicate the time delay between enhanced occurrences of aurora and scatter (see text).

A closer look at the circumstances surrounding the sudden appearance of scatter and the lack thereof during large parts earlier in the time interval helps in estimating the determining factors. First the lack of backscatter will be discussed. In general, there are two possible reasons for the lack of backscatter from a given distance. Either none of the radar beams intersects the ionospheric volume associated with that distance at the right angle, or, there are no irregularities with the relevant dimensions present in the probed

volume. If one or both of these conditions apply, no scatter echoes are received from the corresponding distance. Return of echoes requires the presence of irregularities as well as suitable ionospheric densities along the ray path.

In order to understand the particular echo pattern, it is instructive to consider the possibility of irregularity presence and the propagation conditions separately. A comparison with other days serves as an estimate of the impact of auroral-related processes on the presence of irregularities. On March 3, 2000 (figure 4.8, p.75), propagation conditions apparently promoted ionospheric probing of the latitudinal interval of interest. As described, the amount and location of scatter during this interval reflected the varying auroral intensities. On February 8, on the other hand, we find, in the first half of the period, auroral emissions varying from weak, soft, and red to more intense and energetic, but without clear correspondance to the detection of irregularities. This leads to the conclusion that the presence of aurora alone is not sufficient for the detection of decameter ionospheric structure and that other conditions must prevail in order to successfully probe an ionospheric volume. Namely, plasma densities must allow for suitable ray paths.

From the above rough estimate of the effect of soft precipitation on the  $F$  region, several minutes of flux would be necessary for sufficient ray bending if the ionosphere were depleted below average. In the present case, altitudes and/or geographic locations of the enhanced densities might not be located appropriately to promote probing beams. Again, a comparison with data from March 3 can elucidate the different ionospheric circumstances. Figures 4.13 and 4.14 for March 3 and February 8 respectively show modelled ray traces for the meridional beam at Kodiak during selected times in the beginning of each data period. The elevation angles range between  $5^\circ$  and  $35^\circ$ . The radar frequency was set to the actual 10 MHz employed on these occasions. No perturbations are assumed in the model. The propagation mode is based on half-hop modes only. The ionospheric parameters determining the propagation conditions were measured by the ionosonde at Gakona. Noticeable in the first plot (figure 4.13) are the relatively low refraction altitudes on March 3 determined by the altitude and the plasma frequency of the  $F_2$  layer. Although the single point measurements at Gakona cannot describe changing conditions along the ray paths, an impression of ionospheric conditions can be obtained.



The ionosonde is located with  $63.1^\circ$  at the equatorward border in the data diagrams. The obtained overhead parameters likely do not reflect the more poleward auroral precipitation and represent therefore background conditions. The plasma frequency at the time of the measurement (08:45 UT) represents a peak electron density of  $2.4 \times 10^5 \text{ cm}^{-3}$  at the altitude of 284 km. Regions of vertical incidence of the radio wave on the magnetic field are at distances of 600 km and larger. The latitudinal interval of interest, at ranges between approximately 700 - 2000 km, is probed with a considerable fraction of the beam power.

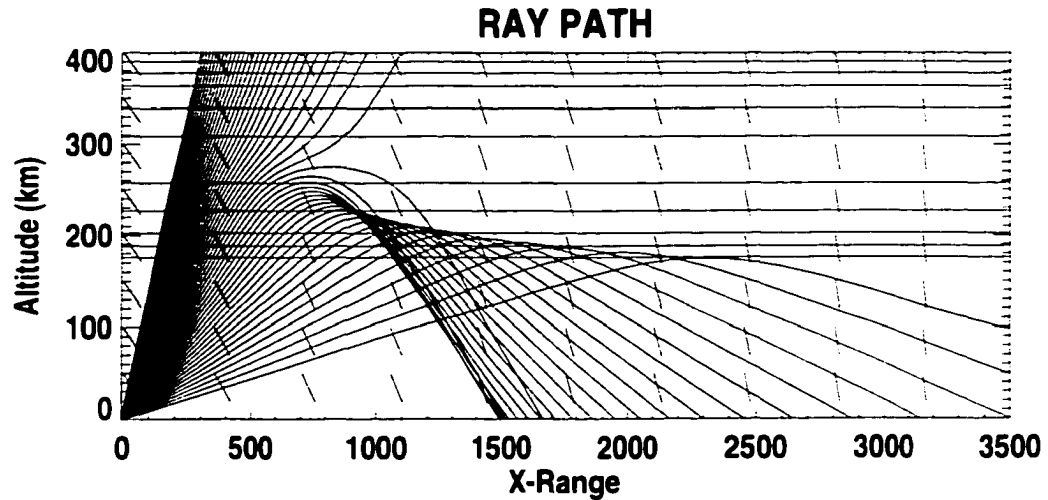


Figure 4.13. Modelled ray tracing for the meridional radar beam on March 3, 2000, 8:45 UT.

The second plot (figure 4.14) presents modelled ray paths for February 8. The maximum  $F_2$  density at 09:14 UT is inferred to be  $6.7 \times 10^4 \text{ cm}^{-3}$  at 362 km altitude. The requirement of orthogonality of wave vector and magnetic field is not fulfilled before an approximate radial distance of 1500 km from the radar. The remainder of the interval between  $63^\circ$  and  $75^\circ$  geom latitudes is illuminated by a power density in the radar beam which is smaller than in the above example. This reduces the chances for obtaining backscatter. The implication of low power in the probing beam will be discussed in more detail in chapter 5.

Thus, ionospheric conditions above Gakona are less favorable for the detection of irregularities around Poker Flat latitudes on February 8 than on March 3. The early soft

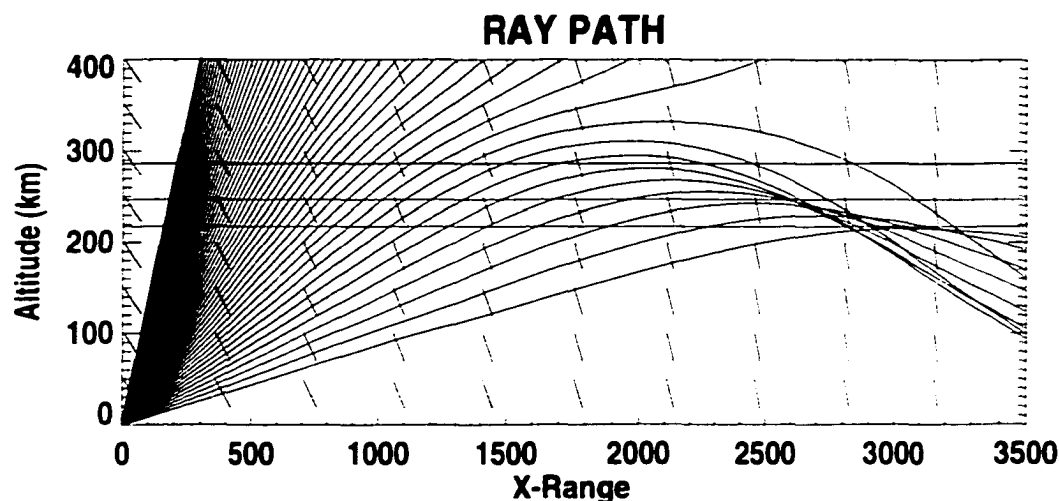


Figure 4.14. Modelled ray tracing for the meridional radar beam on February 8, 2000, 09:14 UT.

fluxes seem not to considerably alter this situation, possibly since they happen at relatively high altitudes and radial distances of 1000 km and larger. The short interval of energetic precipitation at 09:50 UT accompanied by a scatter patch of the auroral intensification supports the hypothesis of the importance of the ionization location under these conditions. Figure 4.15 shows the backscatter and aurora at 09:50 UT. The HF echoes are seen at the poleward edge and further poleward of the auroral arc in the allsky camera FOV. Allsky camera records of Kaktovik, at the north coast of Alaska (not shown) indicate another weak auroral arc system at about the same latitudes. These auroral forms are relatively persistent, unlike the occurrence of scatter echoes. In line with this argument, the comparably sharp increase of scatter at 10:40 UT might very well be ascribed to the production of adequate ionospheric densities through the soft fluxes equatorward of the large scatter region at about the same time. The diffuse red emissions expand southward to  $65^\circ$  and to around  $63^\circ$  geom latitude shortly before and during the onset of the enhanced radar signals.

Two more factors can contribute to the appearance of backscatter in a previously scatter-free volume. One is the relation to the intensification and the spread of the auroral particle flux, which on this day happens after 10:15 UT. The vertical lines in the lower panel of the compound diagram for this day (figure 4.12) indicate the time elapsed between the

occurrences of enhanced aurora and backscatter. The lines were determined by the times of the maximum gradients of the increase in auroral and radar occurrences, respectively. The time interval between the vertical lines is  $18 \pm 1$  minutes. This time might reflect, at least partially, the combined temporal scales required for ionization at closer ranges and the generation of decameter ionospheric structure. On the other hand, drift of plasma density enhancements into the FOV would represent a readily available basis for the generation of irregularities. The time series of the entire radar FOV (not shown) indicates an azimuthal expansion and/or drift of the scatter region with an estimated speed of 700 m/s. Simultaneous observation of Doppler drift velocities show equatorward flow with values up to about 650 m/s in the echo patch (not shown). It is therefore likely that drift of plasma played a role in the observed echo pattern. Drift of the enhanced-density volume out of the FOV would then explain the later decay of the scatter structure.

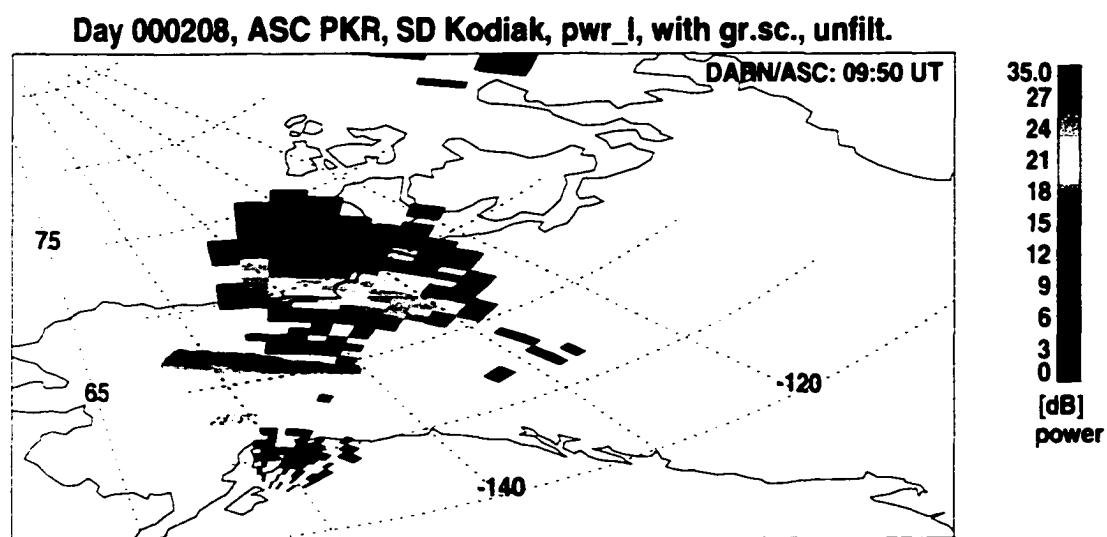


Figure 4.15. Aurora and radar scatter on February 8, 2000. 09:50 UT. Scatter echoes appear in a larger region on the poleward side of the intense auroral arc.

With precipitation-induced ionization, or through drift of dense patches from elsewhere, the importance of the ionospheric plasma densities for the detection of irregularities even under auroral conditions is underlined. The poor correlation between aurora and backscatter under very quiet conditions adds to the spectra of possible relationships so far assembled.

Already discussed is the positive connection under quiet to moderate perturbation levels. In the next two sections upper limits of ionospheric plasma densities will be investigated.

#### 4.5.4 No Irregularities through High Ionospheric Densities

Through Ohm's law the ionospheric electric field is inversely related to the plasma conductivity. The electric field strength in the ionosphere varies considerably, often within short time scales. A significant reduction of the electric field can be an important stabilizing factor with respect to the generation of irregularities. We already know that irregularities with scale sizes below 100 m decay on very short time scales. Detection of decameter structures implies therefore continuous generation. Stabilizing previously unstable conditions would consequently be noticeable within a matter of seconds, through fading of previously received ionospheric scatter echoes. The ionospheric electric field is known to play an important role in destabilizing plasma density gradients. The resulting instability is the  $\mathbf{E} \times \mathbf{B}$  gradient drift instability, generating irregularities over a wide range of scale sizes [Keskinen and Ossakow, 1982, 1983a].

Plasma at  $F$  region altitudes drifts with  $\mathbf{E} \times \mathbf{B}$  velocity. A reduction in plasma flow velocities has been repeatedly observed at the peak of the substorm expansion phase. Flows decrease to values around 50 - 200 m/s [e.g., Morelli et al., 1995; Olsson et al., 1998], corresponding to a decrease of the electric field to a few mV/m. Time scales are on the order of a few minutes. The suppressed fields can be accompanied by a large-scale dropout of HF backscatter [e.g., Lewis et al., 1997; Yeoman and Lühr, 1997].

The determination of instability growth rates in numerical and analytical studies is based on "typical ionospheric parameter" under undisturbed conditions. Assumed electric field values of 10 mV/m are representative for such a set of parameter [e.g., Ossakow and Chaturvedi, 1979; Keskinen and Ossakow, 1982]. Neglecting diffusion and neutral winds, the growth rate for the  $\mathbf{E} \times \mathbf{B}$  instability is approximated by  $\gamma \simeq E_0 / (BL)$ , where  $E_0$  is the convection electric field,  $B$  the ambient magnetic field, 0.5 Gauss, and  $L$  the characteristic density gradient scale length. Typical density gradient scale lengths for primary irregularities in the deca-kilometer range [Keskinen and Ossakow, 1982]. For  $L = 50$  km the growth time for the linear growth phase of instabilities results in 250 s. For an ambient field  $E_0 = 2$  mV/m, the growth time increases to about 21 min. On this time scale diffusion for

small-scale structures becomes very important. For meter-scale irregularities, diffusion can then easily outgrow the generation of new irregularities [Vickrey and Kelley, 1982; Kelley, 1989].

*In situ* measurements in aurora have indicated, that the regions of suppressed electric fields are limited to regions inside auroral arcs. Steep electron density gradients have been found associated with discrete auroral arcs [Prikryl *et al.*, 1995]. Auroral arcs with the associated field-aligned current pairs have characteristic scale sizes of the order of 100 km and well below [Johnson *et al.*, 1998; Zhu *et al.*, 2000]. Electric fields adjacent to auroral arcs are found in the range of tens to hundreds of mV/m, while inside the arcs fields are of the order of 10 mV/m or less [Aikio *et al.*, 1993; Lanchester *et al.*, 1998; Marklund *et al.*, 1998]. The large electric fields outside of the arcs arise from the necessity of current continuity across high-conductivity/low-conductivity regions. Thus, there are two concurrent effects due to auroral precipitation: Continuous ionization in precipitation regions raises the overall conductivity level, thus suppressing the electric field at large scales. At the same time small-scale density gradients in the vicinity of auroral arcs result in electric fields at the same spatial and temporal dimensions, whereas electric fields inside regions with auroral precipitation are decreased. A decrease in scatter occurrence due to low electric fields would be expected to have about the same spatial scales as the extent of the low fields.

A decrease in scatter occurrence in ionospheric volumes with auroral precipitation can be seen in figure 4.16. The data were taken on December 5, 1997 with the HF radar in Pykkvibær and the MSP in Longyearbyen. The middle panel shows the poleward expansion of two moderate substorms. The backscatter echoes (upper panel) appear to be concentrated on areas around the brightest optical aurora. This effect is also seen on the lower panel, although the sums over auroral and scatter echo occurrence mask the latitudinal distribution. The well defined dropout of backscatter at auroral locations could be an indication of very low electric field strength within the auroral arcs. The observed diminishing scatter is hereby associated with an increase in conductivity due to auroral ionization. Noticeable decrease in scatter occurs where the aurora is brighter and accompanied by aurora at the blue wavelength. With the electric field playing an important role in the cascading of irregularities into smaller wavelength domains, lessened irregularity generation can be expected for a decrease in field strength.

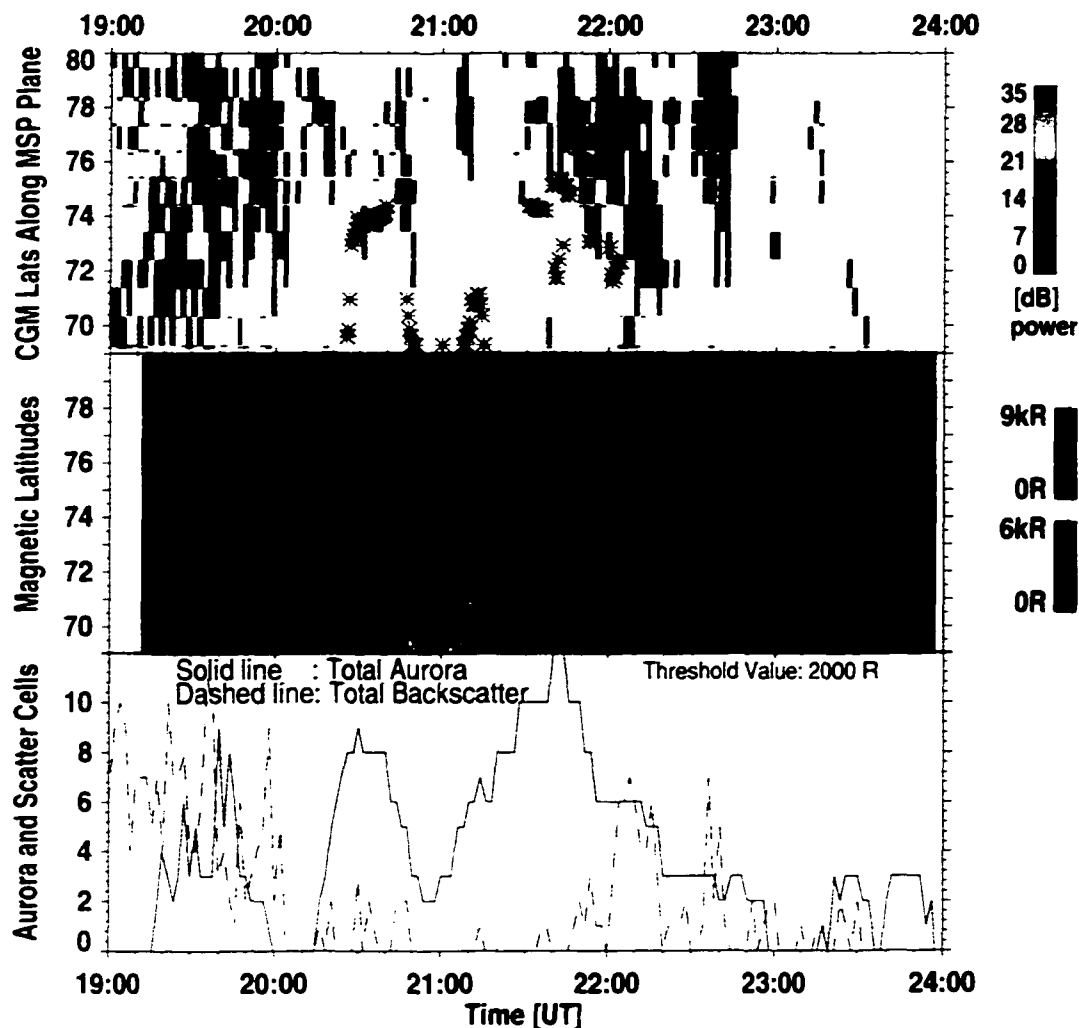


Figure 4.16. North European observations in the same format as in figure 4.8, except for Pykkvibær and Longyearbyen data on December 5, 1997. Magnetic midnight at Longyearbyen is at 20:40 UT.

Also other factors besides the electric field contribute to the growth of instabilities. On the nightside, in the vicinity of the Harang discontinuity, the effect of low ambient electric fields can be counteracted by the motion of the neutral atmosphere relative to the plasma [Kelley, 1989; Temerin and Kintner, 1989]. Slip velocities occur where the plasma reacts instantaneously to electric field changes, whereas neutrals continue their forward drift [e.g., review by Tsunoda, 1988]. There are additional free energy sources which can also result

in growing instabilities, such as velocity shear [Kelley and Carlson, 1977], temperature gradients [Zhu et al., 2000], fluctuations in the electric field [Kelley and Carlson, 1977], or field-aligned currents in conjunction with the aurora. Setting the electric field equal to zero, using the a gradient scale length of 50 km, an electron density of  $2 \times 10^4 \text{ cm}^{-3}$ , a field-aligned current density of  $20 \mu\text{A}/\text{m}^2$ , and an altitude of 500 km, the linear growth time of the current convective instability is 100 seconds [Ossakow and Chaturvedi, 1979]. This time is considerably shorter than the linear growth time for the  $\mathbf{E} \times \mathbf{B}$  instability in a low ambient electric field. However, determination of the relative contribution of a particular destabilizing parameter is not possible based on this data set.

#### 4.5.5 Aspect Sensitivity

An important requirement for a radar signal to be scattered back to the receiver is perpendicularity to the magnetic field line in the scattering region [e.g., Fejer and Kelley, 1980]. The backscatter cross section is related to the incident (aspect) angle, rapidly decreasing for increasing off-perpendicularity. Empirical values were found of 6 dB or more attenuation per degree for values off, but close to, normal incidence [Bates and Albee, 1969].

Birkeland currents and the auroral electrojet, as all electric currents, imply a corresponding magnetic field in their vicinity, decreasing with increasing distance. When this magnetic field is added to the Earth magnetic field, it could lead to small changes in the direction of the magnetic field. To estimate an upper limit of the possible impact on the aspect angle from this effect, observed quantities for the auroral electrojet under active conditions are evaluated.

As an example for high current densities, *Armstrong and Zmuda* [1970] reported magnetic perturbations during a satellite overflight at 1100 km altitude under  $K_p = 8^-$  conditions. The observations are interpreted as consistent with a pair of field-aligned current sheets closing through a Pedersen current and a Hall current at 100 km altitude. The Hall current extends latitudinally for approximately 240 km with a strength of about 8 A/m (i.e.  $33 \mu\text{A}/\text{m}^2$ ). In the approximation of an infinite current sheet the magnetic field  $\mathbf{B}'$  due to the Hall current amounts to 5000 nT. Assuming that this horizontal field is perpendicular to the local ambient magnetic field  $\mathbf{B}$ , the vector addition of both fields results in an angular deviation of  $5.7^\circ$  compared to the ambient field alone (0.5 Gauss). However since the

distance from  $F$  layer altitudes to the current sheet in the  $E$  region is likely of the order of the actual width of the current, the approximation of an infinite current sheet does not hold and the magnetic field decreases with distance.

Also field-aligned currents contribute with their horizontal magnetic field to the overall field, albeit in a direction perpendicular to the Hall current magnetic field. In the above example, *Armstrong and Zmuda* describe current densities of 0.64 A/m for the field-aligned and the Pedersen currents. This current density is in the typical range between 0.5 - 1 A/m under moderate to disturbed conditions [e.g., *Stasiewicz and Potemra*, 1998]. Treating the field-aligned currents as extended sheets, the magnetic field due to one sheet has the absolute value of 400 nT in the infinite sheet approximation, between the sheets the combined fields add to 800 nT. The contribution of the Pedersen current is neglected here. The field due to the parallel current sheets acts to bend the total field up to  $1^\circ$  out of the quiet time orientation. Combined geometrically, these effects can amount to a magnetic field distortion of several degrees at  $F$  region altitudes.

Optically deduced magnetic field distortions have much smaller values than found through the calculations here. Determining the magnetic zenith from a time series of narrow-field auroral images, a variation in the location was found, corresponding to a change in the magnetic field angle of about half a degree (*H. Stenbaek-Nielsen*, personal communication, 1999). An explanation of this apparent mismatch could be that in an optical determination of the magnetic zenith the upper portions of the visible aurora are used as guidelines. However, the largest distortions can be expected close to the current sheet at about 100 km altitude. The distance from the current sheet to the tallest rays at 400 - 600 km altitude is about twice the distance than between the current sheet and the radar reflection altitude. Disturbances in the magnetic field are therefore less noticeable at greater altitudes.

The effect of variations in the magnetic field orientation is to change the angle of incidence between the radar ray and the magnetic field. The power in the radar echo decreases hereby with a few dB attenuation per degree off orthogonal incidence and might even lead to the disappearance of the signal in the noise level. Aspect sensitivity is a factor considered in  $E$  region probing by coherent scatter radars [e.g., *Williams et al.*, 1999, or cf. <http://www.geo.fmi.fi/PLASMA/RADAR/STARE>]. Radar beams for  $E$  region radars typically have a confined range of elevation angles. The region of interest is usually at auroral



electrojet altitudes with a height extension of only a few tens of kilometers. The condition of orthogonality with the field-aligned irregularities has therefore to be met in a small vertical range. The cone of permitted aspect angles is thus quite narrow [*Uspensky et al.*, 1994].

Radars probing the *F* region with a vertically spread beam are less vulnerable to aspect sensitivity. While the change in aspect angles might discriminate the beam at certain elevation angles, power at other elevation angles is likely to have aspect angles closer to orthogonality due to distorted field lines. A noticeable effect is only imaginable for border areas between orthogonal incidence and no orthogonality, i.e. areas where the aspect angle is already large without considering magnetic field distortion. Slight variations around the aspect angle through motion of the field lines might then be visible as fluctuations in the power or might even effect the occurrence of backscatter. Such an effect, however, would be difficult to discern in the typical variability of backscatter pattern. Furthermore, the temporal scale of a variation in the direction of the magnetic field has to be sufficiently large to allow for plasma motion with the field. Although a situation like the one developed above seems plausible under the very disturbed conditions described by *Armstrong and Zmuda*, it is likely, that the associated ionospheric perturbances cause other effects with a larger impact on *F* region backscatter (see other sections 4.5.4, 4.5.6, and 4.5.7).

Ground magnetometer traces can be used to infer horizontal ionospheric currents. Field-aligned current signatures produce about the same variations (in the magnetic D component) as horizontal currents in the north-south direction, and are therefore more difficult to detect than signatures of the east-west aligned auroral electrojet. Typical traces of the ground magnetometer for the moderate conditions of the data set presented are on the order of 500 nT or less. A quick estimate gives an upper level of magnetic perturbation in the ionosphere. For a vertical distance of 100 km from the ground to the current sheet, the same magnitude of the current-induced magnetic field can be found at 200 km altitude. The effect of Birkeland currents in that altitude will be stronger than on the ground. Assuming a local current closure, the same amount of induced magnetic field for the field-aligned currents is added. The total magnetic field vector then has a magnitude of 750 nT. The upper limit is therefore a field line distortion of  $0.9^\circ$  degrees. This would be just enough to change the power in the backscatter a few decibels. Since echo power is varying quite

regularly on a larger scale than few decibel, no data was found to indicate the impact of aspect sensitivity.

Due to the minor possible effects, and, more importantly, the vertical spread in the beam power, aspect sensitivity can be ruled out as an factor with significant impact on  $F$  region HF backscatter measurements.

#### 4.5.6 Unfavorable Ray Propagation through High $E$ Region Densities

Precipitation with characteristic energies of about 1 keV and higher raises plasma densities in the  $E$  region. Enhanced ionization at  $E$  region altitudes can have several effects on  $F$  region radar probing. Coupling along magnetic field lines plays an important role in the case of high  $E$  region conductivities. As discussed in chapter 2, the transport of electrons between the two layers acts to reduce the electric field in the  $F$  region which is due to ion diffusion, thus decreasing decay times [Vickrey and Kelley, 1982]. This process is believed to have time scales of one hour or more for anomalies with kilometer-sized structure, and longer times for larger irregularities. Smaller sizes might be affected differently, even though associated time scales have not been investigated. For the smaller scales, on the other hand, the formation of images of  $F$  region irregularities in the  $E$  region becomes important and counteracts  $F$  layer diffusion, prolonging irregularity lifetimes [Vickrey and Kelley, 1982]. Thus, a conducting  $E$  region is likely to tap the irregularity reservoir on varying time scales. The formation of irregularities, however, is not prevented by these processes, although instability growth times might be affected.

Another implication of high electron densities in the  $E$  layer is the effect of sharper density gradients on the radio wave propagation. The range of interference spans from a slight signal deviation to a complete refraction for sufficiently high electron densities. In that case irregularities might or might not exist in the region of interest, but they simply are not illuminated by the radar beam. As discussed previously, a strong sporadic  $E$  layer builds up during ongoing energetic ( $\geq 1$  keV) electron precipitation [e.g., Kelley *et al.*, 1980]. Conductivities at altitudes around 100 km increase by several orders of magnitude within tens of seconds during precipitation. Resulting high-density layers have a vertical extent of several kilometers, thus acting as a thick impenetrable layer for HF waves. A particular signal might or might not scatter at a later point from either the ground or

in the ionosphere. But the volume in the  $F$  layer that would have been probed without the density enhancement at lower altitudes is now unreachable for the radio waves. If the patch with higher electron concentration radially extended along one radar beam, a range of elevation angles is affected and the  $F$  layer volume is completely shielded from the sight of the radar for the duration of the sporadic  $E$ .

During conditions of energetic precipitation, high electron densities in the lower ionosphere could therefore lead to a lack of local backscatter in radar echoes due to ionospheric refraction much faster than through the increased diffusion rates discussed above. The former effect is likely seen in the following data set from February 9, 2000. Figure 4.17 shows six hours of mainly premidnight data in the usual format with the lower red emission border overplotted on the upper panels. The time period for this day is characterized by a moderate to low  $K_p$  index of  $3^+$  and  $1^+$ . The diagram shows backscatter in the first third of the interval, which is located at the center and the equatorward side of red aurora. Starting at 07:30 UT a dropout in backscatter occurrence is noticeable preceded by a few minutes by intensifications in the 427.8 nm emission, and coinciding with the start of an auroral poleward expansion. Scatter resumes on a large scale with the fading of the aurora, although low levels of diffuse red emissions continue over a large range of latitudes.

Before investigating effects that could arise from high plasma concentrations in the  $E$  region, we want to take a look at the state of the  $E$  layer as seen by the VHF radar (figure 4.18). There was a fairly high scatter occurrence already at the start of the interval at 06:00 UT. The early equatorward moving filaments do not correlate to any features observed in the aurora. They are possibly due to equatorward propagating gravity waves. Between 06:50 - 07:30 UT a change of the filamentary structure during early times into more diffuse-type echoes, simultaneously with a slight intensification. The different types coexist, apparently unrelated, during this time. It is therefore likely that two different generation processes are involved in these structures. The poleward moving scatter enhancements starting at about 08:30 UT do correspond to poleward moving features observed by the MSP. They could be related to the enhanced densities and electrodynamics during the energetic auroral precipitation which starts at about that time. Its prevalence coincides temporally with the dropout of  $F$  region backscatter.

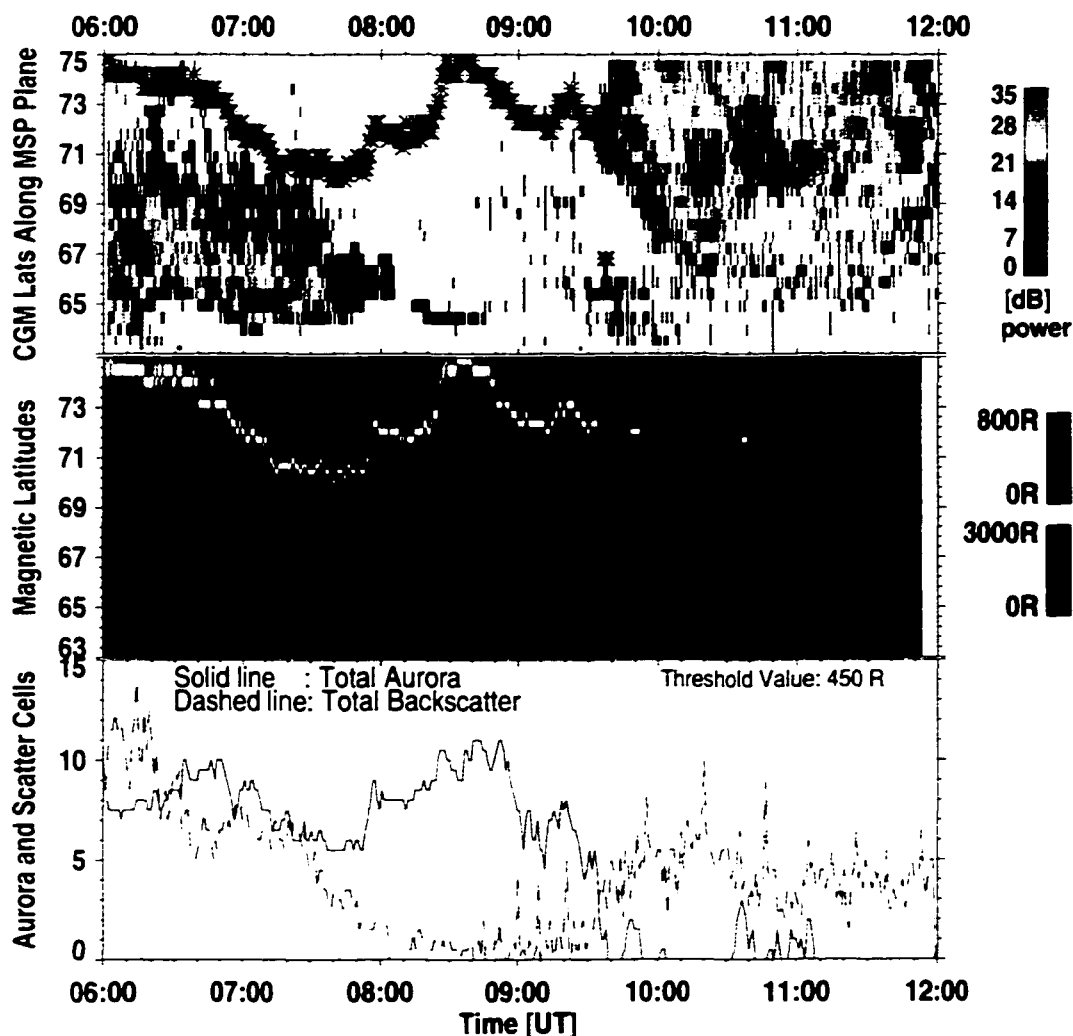


Figure 4.17. Alaskan observations in the same format as in figure 4.8. for February 9, 2000.

The effects of high  $E$  region densities can be investigated through HF ray tracing. Figure 4.19 displays modelled paths for the meridional beam at Kodiak. The ionospheric variables are determined by the ionosonde at Gakona at 07:14 UT on the same day. Gakona was approximately at the equatorward edge of the soft precipitation south of the discrete auroral arcs at that time. The  $F_2$  peak density is found at 290 km with  $1.6 \times 10^5 \text{ cm}^{-3}$ . Reflection altitudes in the figure are below 300 km, similar to the favorable propagation conditions on March 3 (figure 4.13). The ray paths indicate possible backscatter starting at around 800

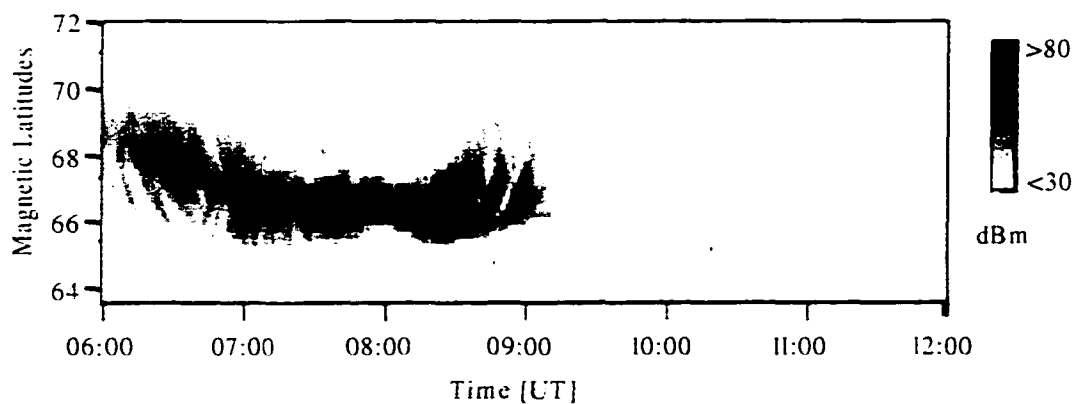


Figure 4.18. *E* region radar aurora from the Elmendorf 50 MHz coherent scatter radar on February 9, 2000.

km and extending to long ranges. This situation is reflected in the simultaneous scatter snapshot over Alaska (figure 4.20). Scatter is shown originating at ranges of 800 km and longer, covering the visible aurora in the allsky camera FOV. Highest signal strengths were found equatorward of the auroral arcs.

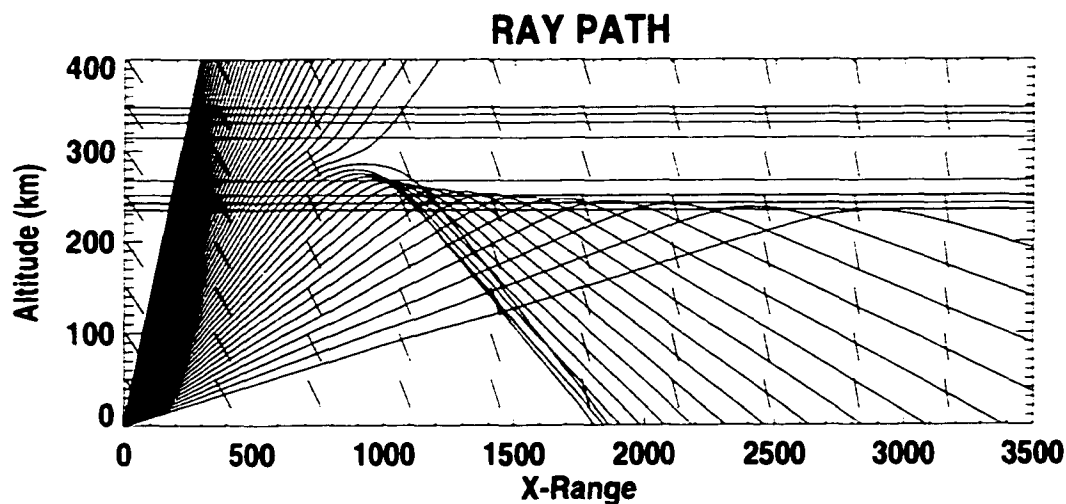


Figure 4.19. Modelled ray tracing for the meridional radar beam on February 9, 2000, 07:14 UT.

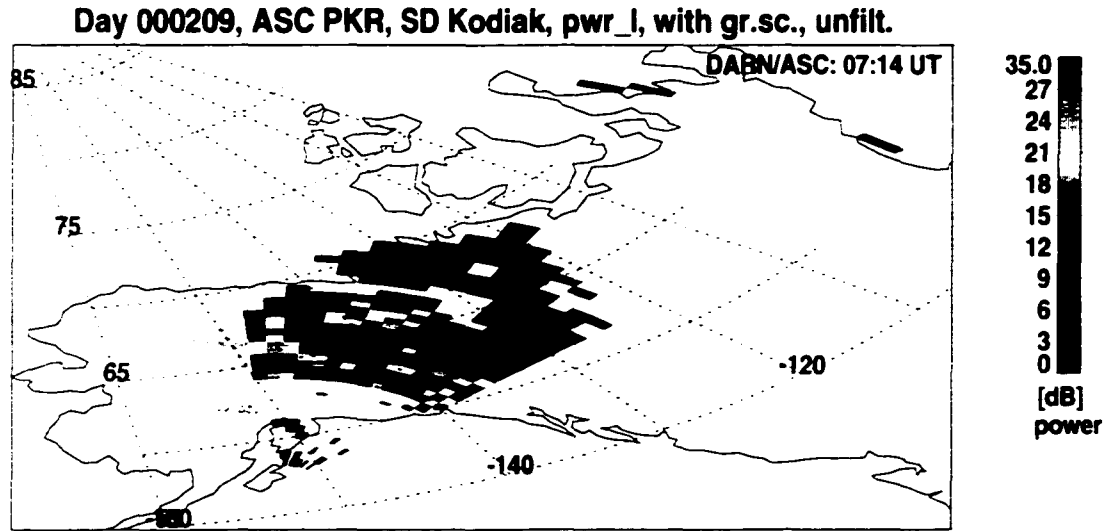


Figure 4.20. Aurora and radar scatter on February 9, 2000. 07:14 UT. Scatter echoes extend to 800 km and more, with maximum signal power equatorward of the aurora in the ASC FOV.

With the onset of the intense precipitation a sporadic *E* region is formed. This has considerable impact on the modelled ray paths, based on Gakona data at 07:59 UT, which can be seen in figure 4.21. The lower elevation angles are now subjected to an additional refraction layer at lower altitudes. Ionosonde measurements indicate critical frequencies corresponding to maximum densities of  $1.7 \times 10^5 \text{cm}^{-3}$  at 400 km and  $7.4 \times 10^4 \text{cm}^{-3}$  at 100 km for the  $F_2$  and sporadic *E* layer respectively. The few scattered echoes around 08:30 UT at latitudes around  $65^\circ$  might be due to scatter off irregularities in the auroral *E* layer. The *F* region is only probed over a limited latitudinal interval and at high altitudes. Additional perturbations along the path can then very likely lead to the observed scatter dropout. The higher altitudes result in an increase of minimum distance of probed ionospheric volume to the radar site. Later in the interval the sporadic *E* layer vanishes together with the transition to weaker and softer precipitation. Backscatter levels rise to and exceed initial occurrence frequencies.

Thus, energetic precipitation and high concentrations in the auroral *E* layer can be a reason for observed backscatter dropout during increased auroral activity. This effect might have been observed in the data from February 9, 2000.

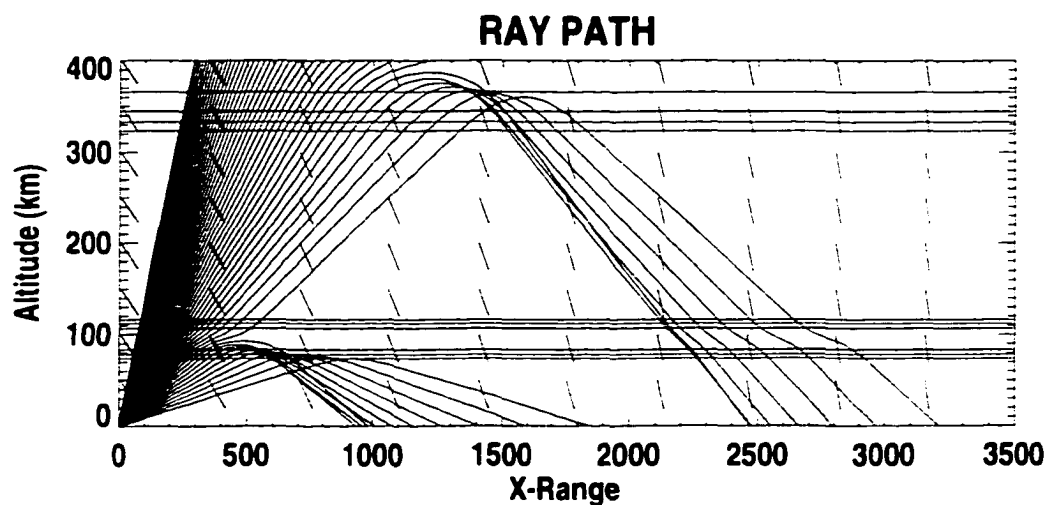


Figure 4.21. Modelled ray tracing for the meridional radar beam on February 9, 2000, 07:59 UT.

#### 4.5.7 Radio Wave Attenuation through High $D$ Region Densities

Particle precipitation in the energy range of the order of 100 keV and higher penetrates the ionosphere to  $D$  region altitudes. Ionization rates vary with the incoming electron energy. High-energy particles create a relatively larger secondary electron population than softer precipitation [Rees, 1988]. Absorption of radio signals due to high electron densities in the  $D$  region can be an important factor for HF radars.

Passing through a plasma, radio waves launch ambient electron oscillations, which are damped by electron-neutral collisions. The excess ionization at  $D$  region altitudes during high-energy precipitation events results in a large number of electrons oscillating with the field of the incoming radar signal. Because of high collision rates much of the energy in the wave is transferred to heating the neutral atmosphere. In a highly collisional medium and with strongly enhanced electron densities the signal can be entirely absorbed. The damping rate varies with the wave frequency, lower frequencies imply longer acceleration times and are therefore more strongly attenuated.  $D$  region attenuation is quoted to be an important factor in the dropout of coherent  $F$  region backscatter [e.g., Yeoman and Lühr, 1997; Milan

*et al.*, 1999]. Attenuation can affect the radar signal where it traverses the *D* region close to the radar site and wherever ground hops are involved.

Particles in the required energy range are not necessarily associated with the visual aurora described here. They are, however, quite regularly observed in the high-latitude ionosphere. They originate from the inner magnetosphere, from the radiation belts and the ring current. The radiation belt consists of electrons and ions with very high energies in the range of keV to several hundred MeV in the inner magnetosphere, a near-Earth region from approximately  $L = 1.1 - 10$ . The particles are trapped in the magnetic field of the Earth, bouncing along closed field lines between mirror points and drifting on constant *L* shells around the Earth. There are two torus-like zones with enhanced electron densities within the entire region. The inner zone is located between  $L = 1.2 - 2$ , the outer zone between  $L = 4 - 6$  [Hess, 1968]. The electrons and ions gradient-B and curvature drift around the Earth. The positive ions in the radiation belt (mainly protons) drift westward, the electrons to the east, resulting in a clockwise ring current, as seen from north. The trapped particles of the radiation belts partly account for the ring current. Positive ions at lower energy ranges than in the radiation belts are responsible for the bulk part of the current density in the ring current. [e.g., review by Hargreaves, 1992]. The average particle energy in the ring current has a maximum of several 100 keV. Besides protons, positive ions of terrestrial origin, mainly  $O^+$ , contribute significantly to the energy density in the ring current [Williams, 1987]. The ring current is generally located between 4 - 6  $R_E$  in the equatorial plane.

Pitch angle diffusion through interaction with fields or waves are a common cause of particle loss from trapped orbits in the outer region of the radiation belt and ring current [e.g., Imran, 1987; Williams, 1987]. The particles are lost on the basis of a steady trickling and as discrete flux events. The former leads to the weakly luminous circumpolar band of auroral emissions, the diffuse auroral oval. It is associated with the stable trapping boundary for ring current electrons with energies  $\geq 40$  keV, and is located equatorward of the discrete auroral oval [cf. review by Galperin and Feldstein, 1996, and references therein]. Flux events of highly energetic electrons and ions into the lower auroral ionosphere are most frequent between approximately  $\text{cgm } 60^\circ$  and  $69^\circ$  [O'Brien, 1962; Frank *et al.*, 1964]. They occur at all local times and are not necessarily related to geomagnetic activity.



The effects of excess ionization at low altitudes, due to high-energy particle precipitation, can be monitored by ground-based instruments. Riometers measure ionospheric absorption of background radiation from space. The intensity of an absorption event is assessed by comparison to the quiet-time average value. With the help of riometer measurements, the radio wave attenuation in the *D* region can be estimated. Attenuation can be due to regular precipitation of the outer ring current particles due to pitch angle diffusion, or to discrete absorption events. Anomalous polar-zone absorption events have been found to accompany magnetic storms. Electron densities below 80 km altitude can rise hereby one order of magnitude to  $10^3 - 5 \times 10^3 \text{ cm}^{-3}$  [Alpert, 1973]. The occurrence frequency is anticorrelated with the sunspot number. (The polar-zone absorption should not be confused with the polar-cap absorption, which increases in occurrence and intensity during high solar activity.)

For the portion of the data set which was taken in Alaska simultaneous measurements of two riometers were consulted. One instrument is located in Elmendorf, near Anchorage, colocated with the VHF auroral radar. The riometer is tuned to radio waves with 38 MHz. Unfortunately, the available data quality is rather coarse from this site (data under <http://dac3.pfrr.alaska.edu/data/hlms-mr.htm>). The other riometer is situated in Gakona, together with the ionosonde (web access under <http://137.229.36.30/cgi-bin/riometer>). It measures absorption at frequencies of 30 MHz.

In the data of the Elmendorf riometer, no significant deviation from the quiet-day curves could be ascertained for any of the data intervals. The data curves (not shown) indicate the voltage across the antenna array rather than absorption in dB, with less voltage implying higher absorption. For the days and times of interest the voltage ranges between 300 - 400 mV, with a possible total range of 0 - 1000 mV. Extraordinary absorption events, which occur a few times per year, result in 0 mV. Less absorption, corresponding to more than 450 mV, is also very rarely found. The observed absorption values were found to be quite within "regular" low levels.

A higher degree of differentiation was possible with the riometer measurements in Gakona. The data for the observational intervals are listed in table 4.3. The days with observations presented in this chapter are marked with an asterisk. The columns indicate the absorption in decibel during the interval, the scatter occurrence level, and Kp indices

Date	Absorption [dB]	Scatter Level	Kp Values
000205	0 - 0.5	low	0 <sup>-</sup> . 1
000208 *	0 - 1	low	2 <sup>-</sup> . 3 <sup>-</sup>
000209 *	~ 0	medium	3 <sup>-</sup> . 1 <sup>-</sup>
000224 *	0 - 1	medium	4 <sup>-</sup> . 5 <sup>-</sup>
000226	0.5 - 1	high	3 . 3 <sup>-</sup>
000301 *	1 - 3	high	4 <sup>-</sup> . 4 <sup>-</sup>
000302	~ 0	low	2 <sup>-</sup> . 1
000303 *	~ 0	high	0 <sup>-</sup> . 1
000305	0	high	1 <sup>-</sup> . 1
000307	1 - 2	medium	3 <sup>-</sup> . 3

Table 4.3. *D* region absorption during the Alaskan data periods, as measured by the riometer in Gakona. The table indicates date, absorption in decibel, scatter level, and Kp indices for the time interval.

for reference. The backscatter occurrence level serves as a rough classification of scatter occurrence during these intervals. Each interval was given one of three possible descriptions: "low," "medium," or "high" backscatter occurrence. Intervals in the first category display generally little backscatter. "Medium" occurrence indicates data with scatter dropout during parts of the interval, but otherwise with a solid presence of backscatter. "High" indicates data with abundant radar echoes. Although the classification of the complex radar echo pattern in only three categories might be disputable, there is undoubtedly a different level of radar response present in the data. The differentiation between the "medium" and "high" scatter levels can at times depend at the choice of the time period presented. These two categories are therefore quite close. There is no direct relationship found between the three categories and Kp level.

The amount of backscatter present is apparently not related to *D* region absorption above Gakona. Attenuation varies from 0 to 3 dB, rather independent of the reception of signal echoes. The only trend visible in table 4.3 is the low absorption level for days with little scatter occurrence. This is in accordance with the expectations of a quiet ionosphere during those times. The Kp index is not necessarily a reflection of locally quiet times (cf.

day 000208), as discussed earlier. Highest cosmic noise attenuation is found to occur in the periods with a medium and high amount of backscatter reception (days 000307 and 000301). This is contrary to the expectation, that a high absorption level could be correlated with diminishing scatter occurrence.

It could be argued that the locations of both instruments, a few degrees poleward of the *D* region crossing of the radar beam, imply that localized *D* layer ionization events could have taken place without being noticed at the riometer stations. However, absorption events only at and below 60° are the exception rather than the rule. Some indication of equatorward expanding energetic fluxes, associated with an equatorward expanding diffuse auroral oval, might be expected to be measurable in the ionosphere above the riometer locations. The statistical absorption level equatorward of the riometer stations is likely not higher than at the sites itself. For the Gakona riometer typical values during disturbed times do not exceed 4 dB attenuation. On typical winter nights about 1 dB of attenuation can be found in the hours around magnetic midnight. Storm time absorption events on the other hand can increase *D* region absorption to over 10 dB.

The indicated level of attenuation at 30 MHz frequency implies higher absorption for longer wavelengths. When neglecting the magnetic field, non-deviative absorption has an inverse square dependency on the frequency [Davidson, 1965]. This dependency causes an approximately 9-fold absorption above the Gakona value of a 10 MHz signal over a 30 MHz wave. Absorption on both ways, to and from the scattering region, results in an 18-fold absorption value for the Kodiak radio wave. In principle a 2 dB attenuation for the 30 MHz wave would cause a complete absorption of the 10 MHz signal. That is, if the 2 dB attenuation measured over Gakona also prevails where the radio wave transverses the *D* region. Such an effect, however, is not observed for a 2 dB absorption. According to empirical values, acquired during these first 10 months of the operation of the Kodiak radar, possibly absorption-related scatter dropouts occur for attenuation values of around 4 - 5 dB at Gakona (W. Bristow, personal communication, 2000). The difference between theoretical expectation and the observations could originate in the fact, that the magnetic field was neglected in the inverse square relationship.

Based on the present data set, absorption in the *D* region under non-storm conditions and with moderate Kp levels is not believed to be a factor determining the absence

of backscatter. The highest absorption in the Gakona riometer occurred at and around data intervals with a large amount of backscatter, but without any noticeable decrease of backscatter. No data can therefore be shown to illustrate the effect of  $D$  region absorption.

#### 4.5.8 Backscatter under Disturbed Auroral Conditions

As we saw above, neither the weakest nor the most intense ionospheric and/or auroral conditions seem to promote the successful detection of  $F$  region scatter. The question is therefore, if there are threshold values determining the reception of backscatter in the auroral region. The importance of favorable propagation conditions in the presence of irregularities is elucidated further in a case which shows both strong particle fluxes and high backscatter occurrence. On March 1, 2000 the disturbance level with Kp values of  $4^+$  and  $4^-$  was relatively high with quite active aurora (figure 4.22). This did not, as seen in previous cases, prevent the reception of a high amount of backscatter throughout the entire interval. The echo pattern is very structured, and shows good correspondence to the concurrent intensifications in the red auroral line. The spatial and temporal occurrence of scatter runs parallel to the optical emissions.

The VHF records confirm that the auroral ionization is not restricted to the  $F$  region. In figure 4.23 large amounts of structured  $E$  region scatter can be seen poleward of Poker Flat, which already starts prior to this interval, at about 5 UT (not shown). Ionospheric densities and structure therefore appear across  $E$  and  $F$  region altitudes without the occurrence of dropouts due to blanketing or absorption.

This seemingly contradicts the observations during the even less disturbed day February 9 (figure 4.17, p.95), where a scatter dropout for higher energy fluxes was observed. Note the higher auroral intensity level on March 1, 2000, reflected in the change of the color bar scales. Under these circumstances the varying flux energies throughout the period do apparently not result in similar disturbed ray paths, as seen before. The higher ratio of blue to red brightnesses at lower latitudes in the center of the interval did not result in a sporadic  $E$  layer and hence did not prevent the probing of the  $F$  region.

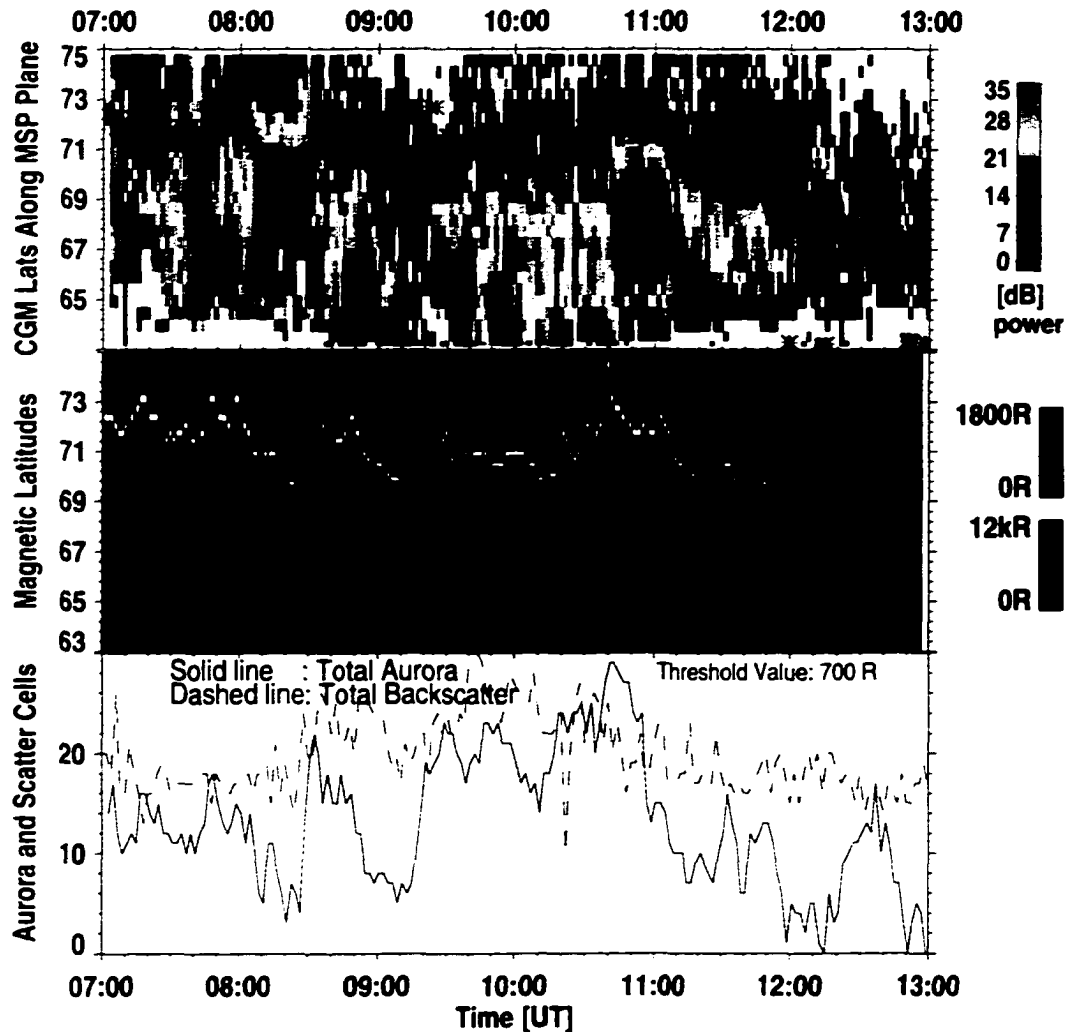


Figure 4.22. Alaskan observations in the same format as in figure 4.8. for March 1, 2000.

Unfortunately, no ionosonde measurements are available for March 1. The all-day scatter diagram for this day (not shown) displays a rather late retreat of groundscatter, signifying relatively high ionospheric densities.

Ray tracing based on a fictitious ionosphere, which could correspond to conditions present during this period, is shown in figure 4.24. Assumed parameters are  $F_2$  and sporadic  $E$  maximum densities and altitudes of  $3 \times 10^5 \text{cm}^{-3}$  at 300 km and  $1 \times 10^5 \text{cm}^{-3}$  at 100 km, respectively. In spite of a blanketing effect by the auroral  $E$  layer,  $F$  region probing at

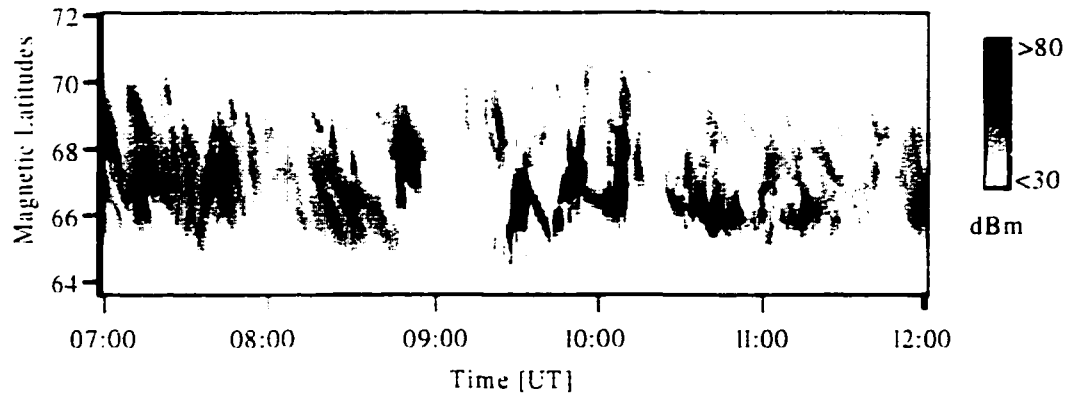


Figure 4.23. *E* region radar aurora from the Elmendorf 50 MHz coherent scatter radar on March 1, 2000.

the same ground ranges is partially still possible through high *F* layer densities. However elevation angle measurements for this day (not shown) indicate scatter echoes from rays with a wide spread of different elevation angles in close proximity. The associated turbulent densities are in discrepancy with the steadiness of a modelled ionosphere. The fact that

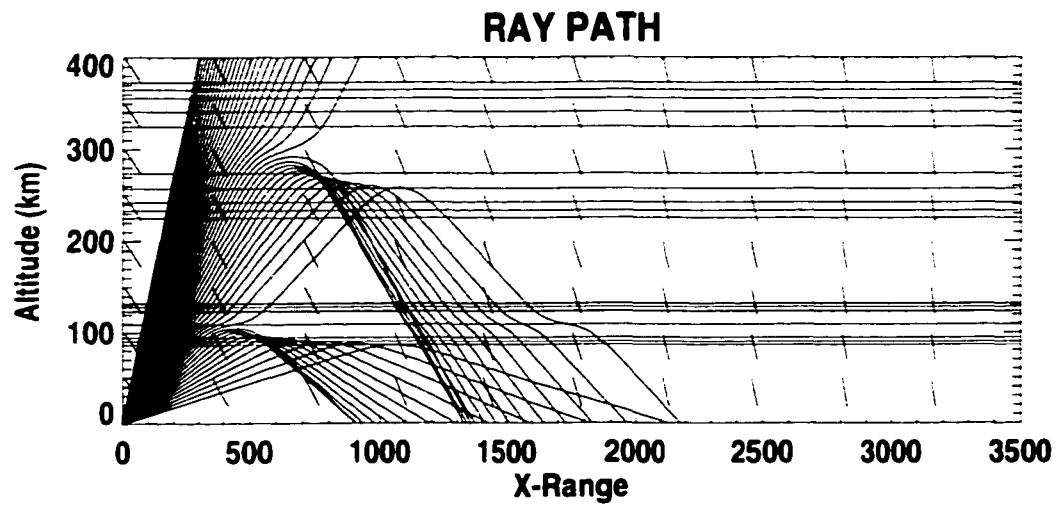


Figure 4.24. Modelled ray tracing for the meridional radar beam for assumed ionospheric conditions.

despite the apparently perturbed ray paths a high occurrence level of backscatter is received. This could emphasize the importance of favorable propagation conditions. High ionospheric concentrations enable the refraction of a larger fraction of the beam power than a depleted ionosphere. This could be to an extent that offsets the adverse impact of blanketing through *E* region densities exceeding *F* layer critical frequencies.

## Chapter 5

# Discussion and Conclusion

This chapter recapitulates the observations and discusses the possible role of ionospheric background densities for the successful reception of backscatter in or despite the presence of aurora. A dayside source for high nighttime plasma densities is suggested and discussed.

In general terms a correspondence was found between the ionospheric disturbance level and the power in radar echoes, their location, and occurrence (section 4.4). The data averaged over the few days with similar Kp indices in the available data set showed agreement, but occasionally also scatter dropouts in regions of active aurora. A larger data set would be expected to smooth over these single features and provide a consistent picture of the mean variation of HF backscatter with Kp . This general approach agrees with the coincidence between the discrete auroral zone and HF backscatter in statistical studies [e.g., *Frihagen and Jacobsen, 1971; Ruohoniemi and Greenwald, 1997*]. However, this coincidence could not be verified in the employed minimum temporal and spatial resolution. A statistical approach based on the occurrence of optical aurora and backscatter in the available data set (42 nighttime data intervals) proved a large degree of variation in backscatter patterns.

The presence of density structure in the decameter range is only part of the requirement for the reception of backscatter. HF wave arrival at long distance sites rely on ionospheric refraction and are strongly affected by propagation conditions. Suitable ray paths have to be present to illuminate ionospheric volumes that contain irregularities. Ionospheric backscatter appears therefore as a convolution of irregularities in the ionosphere and propagation conditions.



The relatively large variation in backscatter patterns on single days is very striking. The variation proved to be too large to enable a statistical approach to quantify possibly stringent relationships. Days with effectively the same type of magnetic traces and comparable auroral activity can have very different radar signatures. The examples presented in the previous chapter prove this diversity. The relationship between auroral occurrence and radar echoes ranges from a close correlation to visible optical forms, over seemingly unrelated auroral and backscatter occurrences, to a complete lack of backscatter at auroral locations in the observed latitudinal interval. The following scenarios were presented, along with interpretations:

HF radio waves were refracted to a relatively small degree in the presence of low versus high background electron densities. This might have been the reason for the lack of backscatter where scatter echoes were expected (example of February 8, 2000, section 4.5.3). Tuning the transmission frequency to lower values, if possible, can increase beam refraction enough to enabling probing of the irregularities associated with aurora in such cases.

On several occasions where radar signal propagation obviously promoted *F* region probing, a positive correspondence between auroral processes and irregularity detection was observed. This correspondence was apparent for relatively soft auroral precipitation (red auroral brightness, example of March 3, 2000, section 4.5.1). In one case the backscattered signal seemed to reflect the higher density gradients in auroral arcs (example of February 24, 2000, section 4.5.2). In the absence of appreciable plasma drift, the time delays between the onset of an auroral feature and the appearance of backscatter from the same volume yield growth times for decameter irregularities from larger scales.

Furthermore, it was found that there is an upper limit to particle fluxes for successful radar probing. High-energy particle precipitation ionizes at low altitudes in the ionosphere. Enhanced plasma concentrations below the *F* layer absorb wave energy or refract radar beams away from the *F* region. Possibly present irregularity structure remains undetected under such circumstances (example of February 9, 2000, section 4.5.6, and also section 4.5.7). Under disturbed conditions the increase in plasma density actively suppresses the required constant generation of smaller irregularities through decreased electric fields in high-conductivity regions (example of December 5, 1997, section 4.5.4).

In the last example of chapter 4 (March 1, 2000, section 4.5.8), that upper limit was not observed, despite active aurora and energetic particle precipitation. Reduced radar signal absorption were ruled out as a possible cause for the high amount of backscatter received on this day (see section 4.5.7). Other typically adverse conditions of high auroral activity (blanketing  $E$  region, low ionospheric electric fields through high conductivity) were overcome by active aurora and relatively high background plasma densities assumed for that day.

In a number of cases ambient electron densities might have been more important than anticipated. High densities can enable backscatter generation under seemingly disadvantageous propagation conditions, but can also hamper backscatter reception on days with little ray refraction. The role of varying ionospheric plasma densities for radar beam refraction is well known. The changing refraction conditions are counteracted by an often adopted dynamic management of the transmission frequency. Fortunately, the data collected for this thesis were obtained at a constant radar frequency. This allows for a direct comparison of possible changes in the plasma frequency. The hypothesis of the possibly dominating role of electron densities will be discussed below. To this goal the ionospheric conditions for the days with available ionosonde measurements, i.e the days of the Alaskan data set, were investigated.

## 5.1 About the Importance of Ionospheric Densities

The ionosonde data from the location at Gakona were surveyed with respect to the peak  $F_2$  layer densities. The ionosonde works with a 15 min resolution, with four completed frequency scans every hour. A scan reveals the critical  $F_2$  frequency, the height and halfwidth of the  $F_2$  layer, and, if present, the corresponding values for the  $E$  and sporadic  $E$  layer. The deduced peak  $F_2$  layer electron density and the  $F_2$  peak altitude were collected for the duration of the intervals investigated. The results are listed in table 5.1. Besides the density for the  $F_2$  critical plasma frequency,  $N(F_2)$ , and the  $F_2$  layer altitude, the number of contributing measurements for that data interval, the backscatter occurrence level and the Kp indices are repeated. The scatter occurrence level reflects roughly the amount of scatter present during a particular interval. It was defined in section 4.5.7. Intervals with

“low” backscatter occurrence level display generally little backscatter. “Medium” occurrence indicates data with scatter dropout during parts of the interval, but else with a solid presence of backscatter, and “high” indicates data with abundant radar echoes. These latter two categories are quite close. There is no direct relationship found between the three categories and Kp level. The days with observations presented in this thesis are marked with an asterisk in table 5.1. For some of the days no ionospheric parameters were found, because the ionosonde did not indicate any values, or a strong sporadic  $E$  layer obscured the  $F$  region. On one occasion the height of the  $F_2$  layer could not be assessed, although  $N(F_2)$  was found.

The ionospheric densities and layer altitudes in this table show a considerable spread. Regarding the categories with low, medium, and high scatter occurrence separately, a slight trend appears. Different ranges for  $F_2$  peak densities and the altitude of the  $F_2$  layer exist for low scatter occurrence on the one side, and medium and high scatter level on the other. Mean peak densities for the days with low scatter occurrence are found to have the lowest values, at or below  $1.61 \times 10^5 \text{ cm}^{-3}$ . The mean altitude of the  $F_2$  layer is at or above 350 km for this group. There is no border to be drawn between the densities for medium and high scatter levels, they have values of  $1.66 \times 10^5 \text{ cm}^{-3}$  and higher. Also, the mean  $F_2$  peak altitudes have similar values in both categories, ranging from 308 km to 337 km. The altitude of the  $F_2$  peak layer determines the height of refraction of the radar beam. While the refraction itself is independent of the altitude, a greater height implies larger radial distances between the radar and potential scattering regions. Together with low electron densities a high  $F_2$  peak altitude can therefore contribute to lack of backscatter from the observed region between 700 - 2000 km.

*Walker et al.* [1987] found that peak ionospheric densities of about  $10^5 \text{ cm}^{-3}$  are necessary to refract a 14.5 MHz radar beam at any elevation angle sufficiently to achieve backscatter. Using the simplified relation between the radar frequency and the plasma frequency through the index of refraction (equation 2.1 on page 26), the corresponding minimum ionospheric density for a 10 MHz signal is found to be  $4.8 \times 10^4 \text{ cm}^{-3}$ . Accordingly, even the lowest peak densities in table 5.1 are capable of sufficiently refracting the radar beam somewhere in the radar FOV. This was demonstrated with modelled ray tracing for the lowest density in the table, on day 000208 (figure 4.14). In the presence of

Date	$N(F_2)$ [ $10^5 \text{ cm}^{-3}$ ]	Altitude [km]	No.	Scatter Level	Kp Values
000205	$1.61 \pm 0.16$	$381 \pm 11$	7	low	$0^- . 1$
000208	$1.17 \pm 0.51$	$371 \pm 15$	7	low	$2^- . 3^-$
000209	$1.73 \pm 0.21$	$321 \pm 29$	22	medium	$3^- . 1^+$
000224	n/a	n/a	n/a	medium	$4^- . 5^-$
000226	$1.82 \pm 0.27$	$331 \pm 37$	14	medium	$3 . 3^-$
000301	n/a	n/a	n/a	high	$4^- . 4^-$
000302	$1.30 \pm 0.41$	$350 \pm 42$	22	low	$2^- . 1$
000303	$2.12 \pm 0.48$	$308 \pm 22$	15	high	$0^+ . 1$
000305	$1.66 \pm 0.49$	$337 \pm 37$	15	high	$1^- . 1$
000307	$2.12 \pm 0.21$	n/a	7	medium	$3^- . 3$

Table 5.1.  $F_2$  region parameter for the Alaskan data periods, as measured by the ionosonde in Gakona. The table indicates date,  $F_2$  peak densities,  $F_2$  layer altitude, number of usable ionosonde measurements per time interval, scatter level, and Kp indices for the time interval.

irregularities, backscatter from far ranges is more likely under low-density conditions. However, under low-density conditions a smaller fraction of the beam power actually probes the ionosphere. The vertical pattern of the antenna beam is determined, among others, by the ground reflection coefficient [Walker *et al.*, 1987]. Due to interference between the free-space beam pattern and its reflection from the ground, the maximum power in the beam is found at an elevation angle higher than the geometrical middle. Walker *et al.* determined the angle of maximum power transmission for a 8 (14.5) MHz beam to be  $35^\circ$  ( $20^\circ$ ) degrees. Higher refraction makes more power available for ionospheric probing. As a consequence, backscattered power increases with ionospheric density. In principle, it could be expected that the backscatter occurrence itself is independent of the power in the signal. If less power is incident on suitable ionospheric structure, a scattered echo would be still measurable, albeit at lower power levels.

There is, however, a low power cutoff, below which no backscatter is received. Walker *et al.* [1987] numerically calculated signal/noise ratios (SNR) for various elevation angles and two different frequencies at the Goose Bay radar. Assuming a model ionosphere of  $10^5 \text{ cm}^{-3}$ , and a mean square density variation  $\langle \Delta N^2 \rangle^{1/2} = 10^4 \text{ cm}^{-3}$ , the SNR was

found as a function of range. Some of the modelling results are shown in figure 5.1. The calculations neglected loss processes. The two curves indicate the SNR (solid line) and the corresponding elevation angle (dashed line) for two frequencies, at 8.5 MHz and 14.5 MHz. For each take-off angle there are usually two possible ranges where backscatter can be achieved. In this respect this model deviates from the ray tracing used earlier in this thesis. In the *Walker et al.* model the rays usually penetrate the ionospheric layers. The smaller ranges in figure 5.1 correspond to the location of normal incidence on the magnetic field below the peak ionospheric density. Above this peak the beam is refracted in the opposite direction and another point of orthogonal incidence occurs. Only those take-off angles were considered, where the beam was refracted enough to achieve orthogonality with the magnetic field at some point within the given range. The solid line for the lower and upper frequencies has maximum values of 24 and 13 dB at the elevation angles of less than  $12^\circ$  and  $7^\circ$ , respectively. The two values represent the maximum power which can be received by the radar under the given ionospheric conditions. The SNR decreases at smaller elevation angles. With an approximately inverse relationship to the radar wavelength [*Walker et al.*, 1987], the maximum SNR is found at roughly 19 dB for a 10 MHz radio wave. Since these curves represent idealized conditions, a correction of about 6 - 10 dB downward for typical operating conditions should be assumed [*Walker et al.*, 1987].

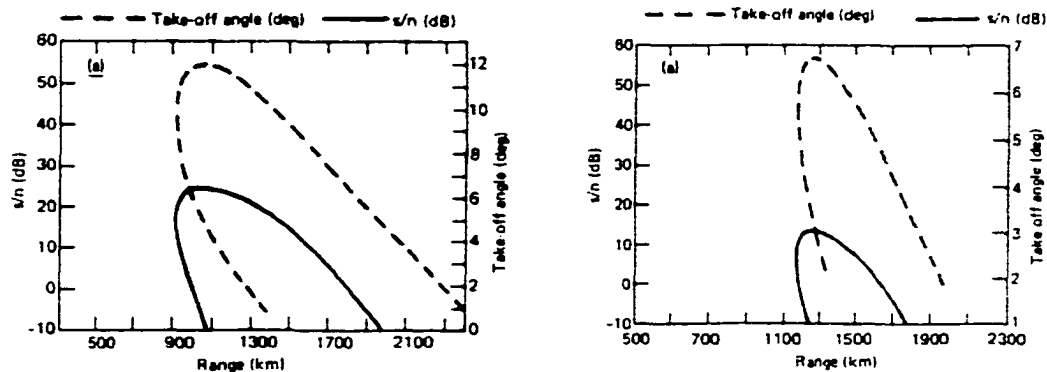


Figure 5.1. SNR and elevation angle for  $\langle \Delta N^2 \rangle^{1/2} = 10^4$ ,  $z_{max} = 300$  km,  $z_{1/2} = 150$  km,  $N_{max} = 10^5$  cm $^{-3}$ , and a radar frequency of 8.5 MHz (left) and 14.5 MHz (right) [*Walker et al.*, 1987].

A high noise level in the return echoes further decreases the SNR. The noise level in the SuperDARN data is determined against mean quiet-time background noise. The noise level on the three data intervals with little backscatter occurrence in table 5.1 is between 3 - 6 dB, on occasions between 6 - 9 dB (not shown). Under the conditions of low ionospheric densities the detected power in the backscatter might therefore decrease drastically, or even be below the detection level. This effect is especially important at ranges where the SNR is already lower than the quoted maximum values in figure 5.1.

Particle precipitation provides high ionization rates and increases therefore radio wave refraction. Accordingly, the chances for receiving backscatter are higher. This could be seen on February 8, 2000 (day 000208 in table 5.1), where the three-time appearance of a sporadic *E* over Gakona (at around 9:45 UT, 10:45 UT, and 11:45 UT, with the highest critical frequencies at 10:45 UT) coincided with the backscatter at longer ranges in the radar FOV (figure 4.12). Due to the small electron densities during these sporadic *E* events (not shown), and possibly their sufficiently large distance to the radar site, no blanketing occurred from this layer. The assumption of low ambient ionospheric densities on this day and the subsequent importance for ionization sources was discussed along with the presentation of this data.

Where aurora occurs at a large distance from the radar site, aurorally induced refraction may not be sufficient for suitable probing under low ambient densities. In order to receive scatter echoes, refraction has to occur between the radar site and the region with irregularities. During most of the three data intervals with low scatter occurrence aurora was at relatively high latitudes. One exception occurred in the second half of February 8, 2000. Following the auroral expansion equatorward, backscatter patches were observed.

Based on these considerations, it is therefore suggested that incidences with little or no ionospheric backscatter from ionospheric volumes where irregularities are expected, are associated with low ambient electron densities. Sufficiently high electron concentrations, on the other hand, facilitate ionospheric probing even under the adverse influence of blanketing effects. On a number of occasions backscatter was received while ionosonde measurements indicated blanketing conditions. To carry this argument further, the impact of a strong *E* layer above Gakona on the path of the radar signal has to be assessed. With its location at  $63.1^\circ$  N *cgm* Gakona is  $1.7^\circ$ -  $4.7^\circ$  degrees poleward of where the radar beam crosses

the  $E$  region to reach the  $F$  region between  $63^\circ$ -  $75^\circ$ . One possible interpretation is that a strong sporadic  $E$  presence was limited in all cases to latitudes around Gakona, but not considerably farther equatorward. Therefore it would not have interfered with the radar beam. Although this limitation might be valid in given cases, it could be ruled out for some of the observations. In these occasions, the ionosonde showed a strong  $E$  region at Gakona which started while the discrete auroral arcs were moving south of the zenith in the MSP data. More precisely, the sporadic  $E$  started slightly equatorward of the equatorward moving auroral brightness. The hydrogen channel of the MSP indicated hydrogen emissions as signature of ring current precipitation on those occasions (not shown). Where the aurora continued to expand equatorward, energetic discrete forms could also be found associated with sporadic  $E$  above Gakona. Hence the ionized  $E$  layer is a response to the continuous motion of the region with auroral emissions. A latitudinally limited effect is therefore expected only where the auroral oval does not extend further equatorward.

Under the active conditions of the days with strong sporadic  $E$ , the aurora indeed expanded south of Gakona. The equatorwardmost locations were presumably at least overhead Kodiak or further south. The ionosonde measured, therefore, in a number of cases density enhancements which most likely also dominated the regions where the ray paths crossed the  $E$  region. However, no concurrent scatter dropout was observed. An example shown in this thesis for high  $E$  layer densities and simultaneous reception of considerable backscatter is the first half of the interval on February 24, 2000 (day 000224). Further occasions happened on the days 000226 and 000307. Unfortunately, for March 1, 2000 (day 000301) no ionosonde data are available. The all-day scatter diagram for that day (not shown) indicates the likelihood of enhanced plasma concentrations, as discussed in section 4.5.8. Peak sporadic  $E$  densities were intermittently higher than the typical winter nighttime  $F$  region densities for these time periods ( $10^5 \leq N(F_2) \leq 2.5 \times 10^5 \text{ cm}^{-3}$ ,  $3 \times 10^5 \leq N(E_s) \leq 4.5 \times 10^5 \text{ cm}^{-3}$ ). During blanketing conditions  $F$  region values could not be obtained. In accordance with the above arguments, densities comparable to the measurements at Gakona are also expected closer to the radar site.

Ionospheric densities do not merely consist of horizontally homogeneous layers of varying plasma concentrations. Rather they have highly variable three-dimensional substructure. High-resolution electron density measurements reveal fluctuations in regions with auroral

fine structure of up to several  $10^5 \text{ cm}^{-3}$  in less than a minute [Lanchester *et al.*, 1997, 2000]. Corresponding spatial scales are typically well under one kilometer in width. While undoubtedly high density levels in sporadic *E* interfere with *F* region probing, it is likely that not the entire high-altitude region is blocked from illumination.

Under the relatively high background densities for these days, a presumably higher fraction of the total beam power was refracted and probed the ionosphere. Walker *et al.* [1987] calculated a difference in signal power of about 20 dB for an increase of  $10^5 \text{ cm}^{-3}$  from maximum *F*<sub>2</sub> densities of  $10^5 \text{ cm}^{-3}$  ( $2 \times 10^5 \text{ cm}^{-3}$ ) for a 8.5 MHz (14.5 MHz) radar signal. The refracted portion of the radar beam that propagates through the “cracks” in the *E* region substructure might therefore carry sufficient power to qualify as strong backscatter signal. Even under the unfavorable conditions of high ionization rates in the *E* region, backscatter from *F* layer irregularities can thus be received, provided the background ionospheric densities are sufficiently high.

Concluding, ionospheric densities play a major role in the detection of irregularities by HF radio waves. Low power in the radar beam distributed over low and few elevation angles for little beam refraction is a reason for unfavorable ray paths and scatter power below detection threshold. High electron densities in turn enable irregularity detection even under seemingly unsuitable conditions. Suggestions to test this statement will be discussed at the end of this chapter. For now the focus turns on a possible source for the varying nighttime ionospheric parameters.

## 5.2 Convection and the Role of the IMF

Enhanced nightside plasma densities are, apart from auroral ionization, also a result of plasma transport from the dayside (cf. section 2.5.1 about convection of dayside plasma). A varying degree of convection of enhanced electron densities might therefore result in different ionospheric conditions at nighttime auroral latitudes. The transport is to a large extent governed by conditions in the solar wind, from the starting point at lower dayside latitudes, over the formation of high-density tongue-like protrusions in the low-density polar cap, the detachment and subsequent convection across the polar cap, eventually the realignment of the patches along L shells on the nightside, and the return flow sunward. Mainly two



components and the total magnitude of the IMF are decisive for the formation of polar cap patches. Tongues of ionization in the polar cap form preferably under a southward orientation of the IMF [Anderson *et al.*, 1988; Rodger *et al.*, 1994; McEwen and Harris, 1996]. Conditions for a detachment of a sizeable blob are enhanced under a northward turn of  $B_z$ , which acts to rearrange drift pattern on the dayside. This diminishes the transport of plasma from lower latitude plasma poleward, thus shutting off further plasma supply to the growing tongue. Changes in the convection pattern due to variations in  $B_y$  have also been found to break up the tongue of ionization into patches [Sojka *et al.*, 1993].

It has been shown that the size of the polar cap patches is related to the time a polar cap potential and accompanying cap size are enlarged [Anderson *et al.*, 1988]. With lifetimes depending on the size of ionospheric structure, large density structures are especially efficient in the transport of plasma to the nightside. Figure 5.2 shows modelling results by Robinson *et al.* [1985] for a large circular blob of ionization convecting antisunward at high latitudes. In the steady convection pattern the patch drifts as a whole and realigns longitudinally at the nightside auroral latitudes. The existence of antisunward drifting irregularities on the nightside is confirmed by Kersley *et al.* [1995] in a study of 7000 satellite passes over a polar cap station at  $79^\circ$  N cgm. The occurrence of these irregularities were found to vary markedly with the solar activity level. A peak of occurrence at 70% of all times in a year of high solar activity level is contrasted by single digits at solar minimum. This dependency could be part of the reason for the low scatter occurrences from Pykkvibær and Hankasalmi in the data set, which was taken during less solar activity than the Kodiak data.

To estimate the possible involvement of high-density plasma transported from the day-side in the HF backscatter observations, the available Kodiak data were surveyed according to observed scatter occurrence levels (high/low) on an hourly basis. Subsequently, these occurrence levels were compared with the IMF  $B_z$  and  $B_y$  components, while looking for simultaneous and time-delayed changes to account for an assumed drift of polar cap patches across the pole. No unambiguous result was found. The variations in the time history for this small data set was too large to prove any meaningful categories of possible IMF configurations. For the general case no simple correlation is to be expected, since the size of the polar cap patches, and the magnetic local time of their arrival at the nightside depend on different time scales. On the one side there is the growth time of the tongue of ionization in

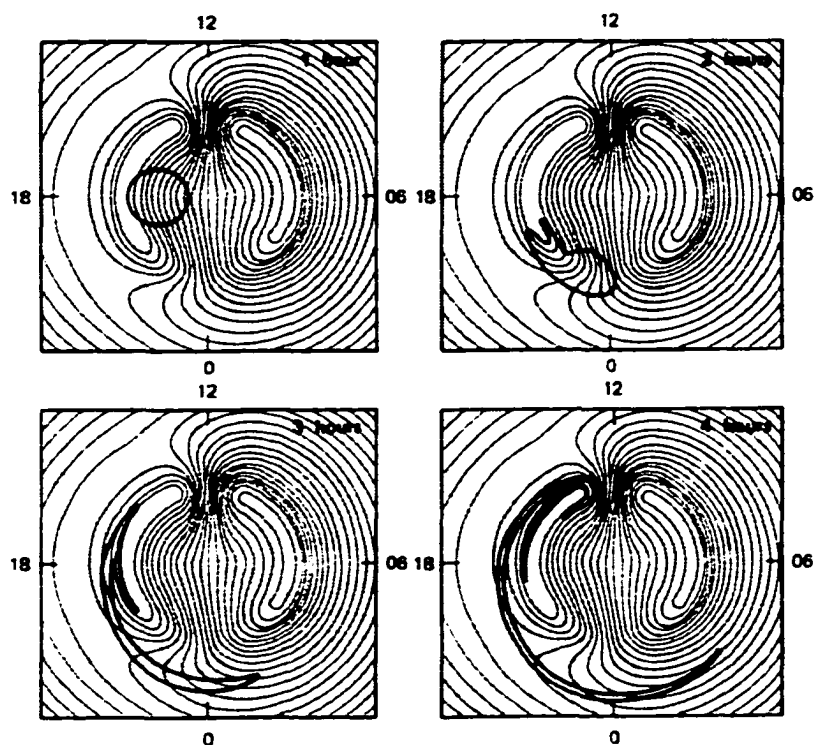


Figure 5.2. Convection of dayside plasma to the nightside (After *Robinson et al. [1985]*).

the dayside polar cap with its dependence on the duration and possibly the steadiness of a southward IMF. On the other hand there are the relatively long time scales of hours for the convection of polar cap patches to the nightside. The drift time over the polar cap with an approximate radius of  $15^\circ$  degrees is about 4 hours for a drift velocity of 200 m/s. The actual time is determined by the convection electric field, which reflects the current IMF configuration. The drift path is subject to changes on the relatively short time scales of reconfiguration of the convection pattern. The point of arrival of polar cap patches on the nightside depends on the orientation of the flow pattern. The local time of the Harang discontinuity can vary from premidnight ( $B_y < 0$ ) to postmidnight ( $B_y > 0$ ) with a maximum time shift of two hours [*Ruohoniemi and Greenwald, 1996*]. In addition, tail reconfiguration on the nightside has an influence on the pattern of ionospheric convection [*Lockwood et al., 1990*].

A closer look at two single cases from the data set is used to elucidate likely important factors for the transport of dayside plasma across the polar cap. Figure 5.3 shows the IMF  $B_z$  and  $B_y$  components during and prior to the data interval on March 1, 2000 (cf. data diagram in figure 4.22, page 104), as recorded by the Wind satellite. (Wind data courtesy R. Lepping at NASA/GSFC and CDAWeb at <http://cdaweb.gsfc.nasa.gov>). The traces display a steady magnetic configuration for long periods. Steady conditions started at 03:30 UT with a negative IMF component of around 5 nT and a positive  $B_y$  with values between 2 - 6 nT, except for a negative excursion at 06:10 UT, until around 08:00 UT. With approximately 40 minutes between the observation at the satellite and the arrival at the Earth for the satellite position and solar wind speed, and a few hours for the cross-polar transport due to enhanced ionospheric convection during this IMF orientation, the time scales of importance are of the order of the steady interval observed. For comparison, the IMF data for the day with little HF backscatter during aurora, February 8, 2000 (cf. data diagram in figure 4.12, page 82) is plotted in figure 5.4. The IMF  $B_y$  component has fluctuating values with a relatively small amplitude. IMF  $B_z$  is oriented mainly northward and undergoes several changes in sign in the hours prior to and in the first part of the data period.

It is plausible that the assumed long and uninterrupted poleward transport of dayside plasma due to the solar wind conditions on March 1, 2000 resulted in large amounts of enhanced plasma densities accumulating in the polar cap at the dayside. It can be speculated that the small fluctuations in  $B_y$  in figure 5.3 favored detachment of one or several blobs with high electron densities which were allowed to build up. The enhanced electron densities, possibly due to polar cap patch plasma, then had a strong impact on the nightside backscatter conditions, as observed on March 1. The decisive aspect of aurora under such conditions might be not the enhancement of ionospheric densities, but the electrodynamic associated with auroral activity. This would establish unstable conditions for the generation of the observed irregularities in an environment, that is highly supportive for HF radio wave propagation.

Unfortunately this hypothesis of the importance of the IMF configuration for nightside  $F$  region HF backscatter reception has no basis in the current dataset to be tested further.

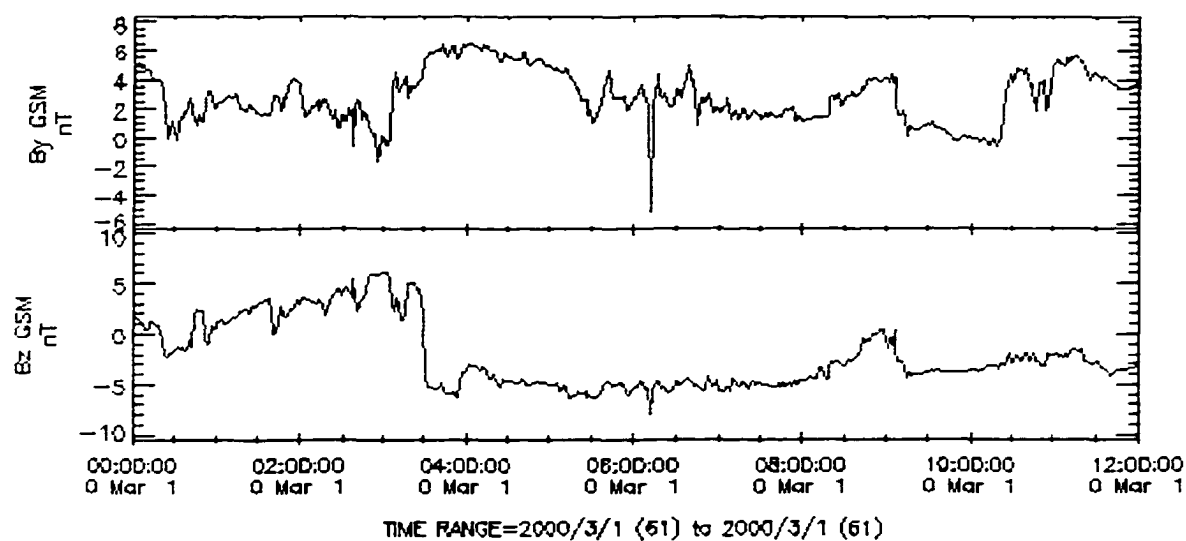


Figure 5.3. IMF data by Wind for March 1, 2000. Extended quiet interval between 3:30 UT and 8:00 UT.

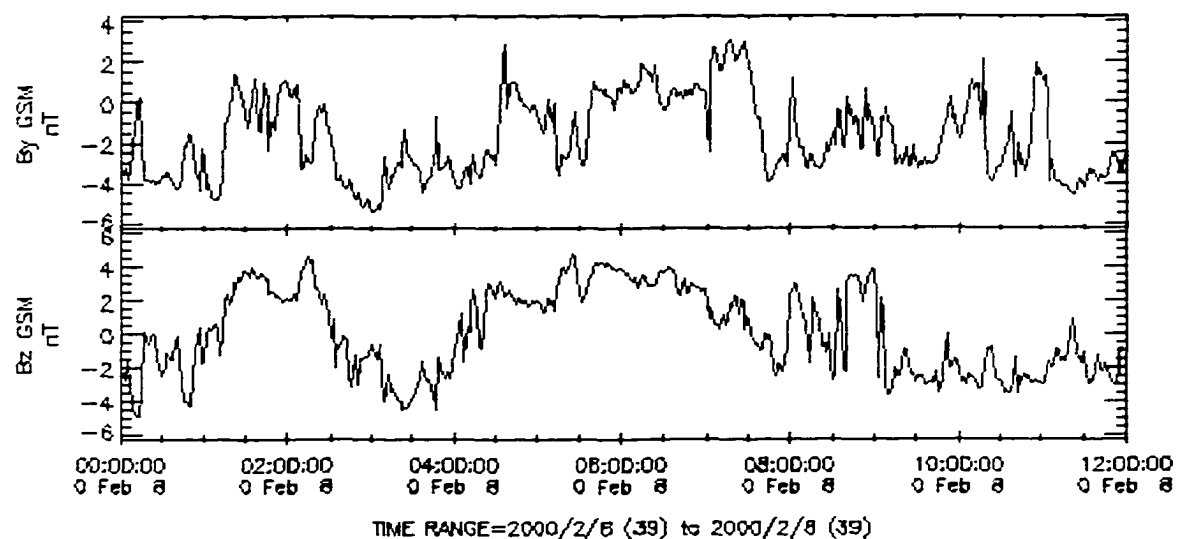


Figure 5.4. IMF data by Wind for February 8, 2000. Northward IMF and small-scale fluctuations in IMF  $B_y$  dominate the hours prior to 08:00 UT, the start of the data interval with ionospheric data.

The possible impact of the solar wind conditions on the backscatter occurrence level deserves to be evaluated more fully.

### 5.3 Suggestions for Further Work

A statistical study relating IMF configurations to the (time-shifted) appearance of night-side auroral region backscatter from small-scale irregularities could prove or disprove a close relationship. Both, the actual configuration of the north/south and east/west IMF components, as well as the overall magnitude and the steadiness of the components would be prime candidates for such a study. These configurations should be brought in comparison with the occurrence of HF backscatter in a study similar to *Ruohoniemi and Greenwald [1997]*, who described scatter rates as a function of daytime, season, year, and Kp indices.

Investigating the importance of ambient plasma densities requires, as a starting point, a larger data set. Information about the ray path is crucial to determine the role of the propagation conditions. This information can be provided in the form of plasma density measurements, preferably at several distances from the radar site. The closest distances should not be farther than a few hundred kilometers from the radar. Unrefracted beam power at the highest elevation angles leaves the ionosphere already in the vicinity of the transmission site (cf. modelled ray traces in figures 4.13 and 4.14). There are limitations by the number and kind of instrumentation available at the appropriate locations in the FOV of the SuperDARN radars. However, there are cases where the electron density measurements can be obtained from ionosondes or incoherent scatter radars (e.g. Sondrestrom radar, EISCAT, and ESR). The electron densities would have to be compared with the radar echo pattern for the same daily times and regions. Clearly, seasonal variations have to be kept in mind for such a comparison. On the nightside, a promising interval to investigate is the time zone around local magnetic midnight, which was the focus in this thesis. This is an interval with significant variations in backscatter occurrence.

Another interesting aspect would be to examine the change in the groundscatter pattern after sunset. The U-shape of the groundscatter around local noon was mentioned a few times in the analysis as a possible indicator for ambient densities. The “slope” and the extent of the groundscatter pattern, as it appears in the time-range scatter diagrams (cf. scatter

diagram 4.1. p. 58) is suggested to indicate absolute  $F$  region plasma density values and decay rates. Care has to be applied in the interpretation of groundscatter, since some of it may in fact be received from the backlobes of the antenna pattern, i.e. from latitudes equatorward of the radar [*Milan et al.*, 1997b].

With the information about ambient densities, a refinement of ray tracing can be achieved. This would also benefit the understanding of HF wave propagation at high latitudes and provide a test for the algorithm translating signal travel time to distance. It would also enhance knowledge about the relative importance of irregularities, associated with aurora or even without the presence of optical aurora, for the radar echo pattern. Valuable hints are contained in the magnitude of the elevation angles. The engagement of beam power at higher elevation angles in the probing indicates higher refraction and therefore higher plasma densities. Higher power densities available for ionospheric probing can overcome the adverse condition of a sporadic  $E$  layer, which else hampers backscatter reception. Ray tracings for five of the days in the Alaskan data set, which indicated "medium" or "high" scatter occurrence, showed a considerable spread in elevation angles over small spatial and temporal scales and coincided temporally with a strong sporadic  $E$ .

Furthermore, it would be interesting to reverse the approach and to attempt to reproduce some of the backscatter patterns in a simulation with the help of detailed ionospheric parameters and a sophisticated ray trace model. For a relatively simple version of such an approach a volume of decameter irregularities would be provided in a given distance from the radar. A "conversion rate" would translate the associated density gradients into scattered power. The observed backscatter pattern would be changed by varying the ionospheric density profiles along the range. A more extended model is achieved by including source terms of ionospheric plasma density. Nighttime ionization levels depend on the length of solar illumination during the day, transport of plasma across the polar cap, and ionization by particle precipitation and associated heating. Such a model has to be based on a large range of scale lengths. Polar cap patches with spatial sizes of hundreds of kilometers would have to be accommodated in the simulation, along with the propagation of HF waves subject to refraction on much smaller scales.

The generation of  $F$  region irregularities itself is a topic far from being resolved. A large part of numerical and analytical work in this field was performed before HF radars

entered the stage with large-scale monitoring of small-scale structure at polar latitude. With much progress in computational possibilities since the 1980's, numerical simulations of generation processes, as well as growth and decay rates of aurorally induced irregularities in a dynamic ionosphere would be desirable. The local impact of suppressed electric fields on the generation of irregularities in active auroral regions is an important issue to be addressed in this context. The determination of the relative importance of particular instabilities would also further the understanding of processes in the high-latitude  $F$  region.

## 5.4 Conclusions

Due to the large number of processes and parameters that determine HF backscatter it was not possible to characterize the relation between aurora and HF backscatter statistically. However, the processes are well understood and convincing arguments could be found for each case study in this thesis. Seemingly contradicting observations (similar aurora and different backscatter, or similar backscatter and different aurora) can be explained with the current understanding of HF radio transmission and instability generation in aurora. The following factors of importance for the relationship between optical and HF radar aurora were identified:

- Irregularity-related
  - With little or no coupling to a conducting  $E$  layer auroral precipitation and related electrodynamics were found to favor the generation of irregularities.
  - Various instability processes have their own time constants and are dependent on different ionospheric parameters such as electric fields, currents, waves, and density, velocity, and temperature gradients. In the determination of growth rates from the data diagrams, the plasma motion has to be taken into account.
  - Growth times and life times of irregularities in the  $F$  region are reduced in the presence of a conducting  $E$  layer. Where the growth times are longer than decay times the result is localized scatter dropout at locations with strong aurora.

- Propagation-related

- High electron density in the  $D$  layer causes absorption of wave energy. However, this effect was not found in the present data. It is therefore concluded that the role of  $D$  region absorption is limited to events with highly disturbed circumstances.
- High electron density in the sporadic  $E$  region refracts the beam away from the higher  $F$  region, thus shielding potential irregularities from the view of the radar.
- High ambient ionospheric density directs a large amount of beam power into the ionosphere. This can offset the blanketing effect of a sporadic  $E$  layer.
- Low ambient ionospheric density results in more beam power exiting the top of the ionosphere and being lost for probing, than high density, for a given transmission frequency. Detection of irregularities requires a minimum in power for a noticeable signal-to-noise ratio. Lack of probing has been found to be a major reason for lack of backscatter where aurora-related irregularities could be expected.



## Chapter 6

### Summary

The ionosphere at polar latitudes is very dynamic. The plasma density undergoes large variations in response to ionization through solar radiation and collisions with precipitating particles. In the dark and relatively depleted ionosphere at the nightside of the Earth, particle fluxes associated with optical aurora are regularly creating local plasma density enhancements at scales of kilometers and larger. These are typically elongated along magnetic field lines. Across the field much higher transverse gradients are found. In the presence of unstable configurations the irregularities decay into smaller structure.

Radars can be used to detect ionospheric plasma structure. Radio waves in the HF range are coherently scattered where the electron density changes rather abruptly. Significant radar wave power is scattered back to the radar site when the structure in electron density has scale sizes of half the radar wavelength. The radio waves are therefore sensitive to irregularities in the decameter range. Aurorally induced irregularities at the appropriate scale sizes are seen in radar returns as so-called HF radar aurora.

This thesis attempted to characterize and explain the relationship between optical and HF radar aurora. A meridian scanning photometer and occasionally an allsky camera served as indicators for the optical aurora. 42 data intervals with common coverage of radar and optical measurements were the basis for the analysis presented.

On an average basis a positive correlation between auroral and backscatter activity could be made. Auroral and backscatter activity levels were higher on magnetically disturbed days. The location of the two "belts," one belt of auroral brightness and one of

radar backscatter, were displaced equatorward during active conditions. The belts were broader, auroral brightnesses and the backscattered power higher. These results also reflect the findings of previous statistical studies on large temporal and spatial scales. Through averaging much of the variation in the immediate response of backscatter to aurora-related processes is smoothed over. This was evidenced in a small-scale statistical overview. Occurrences of optical aurora and backscatter on the minimum spatial resolution for all available data intervals were collected separately. Three groups (occurrences with only aurora, only backscatter, or both) were formed and compared. An inherent correspondence, such as simultaneous decrease and increase or an inverse relationship, would have been detected by unambiguous correlation coefficients. However, a clear relationship between the occurrence of optical and HF radar aurora was not found. The positive correlation in large-scale averages is replaced with a complex relationship on small temporal and spatial scales.

In the investigation of single events no reliable and repeatable connection between optical and HF radar aurora were ascertained. The range of correspondence spans from a close correlation between radar echoes and visible optical forms over seemingly unrelated auroral and backscatter occurrences to a complete lack of backscatter at auroral locations. One explanation, not surprisingly, is found in the well-known dependence of HF radio wave propagation on gradients in electron density. Through this dependency the presence of an (auroral-related) irregularity source is de-emphasized, and the detection mechanism is stressed.

HF waves are significantly refracted by ionospheric density gradients along their path. This property enlarges the ionospheric volume that can be probed. However, it also renders the wave propagation vulnerable to density variations. As a consequence, the path of the radar signal is not predictable and can change, often within short times. The reception of backscatter is therefore dependent on the existence of small-scale irregularities as well as suitable propagation of the radar signal to the probed volume. As a consequence, seemingly similar optical aurora could be found to be associated with a variety of different backscatter patterns. The patterns were characterized and interpreted. The influence of aurora and other processes on irregularity detection by HF waves were isolated and discussed.

Conditions were identified where the beam path was probably undisturbed. In this scenario, the volumes where auroral emissions originate were probed, and backscatter was

generated by the associated irregularities. However, in a number of cases the relationship was not straightforward. Among the aspects found to be of importance are unfavorable radio wave propagation due to either too low or very high ionospheric refraction. Under both circumstances the radar beam may not "see" the density structure in the area under investigation. The beam has to be close to normal incidence on the irregularities to scatter off the structured medium and travel back in the direction of the radar antenna. Refraction can be due to ionization by auroral precipitation itself, or be mainly attributed to the ambient ionospheric densities during the observed interval. Absorption of the radar signal occurs for high-energy particle precipitation into *D* region altitudes. The precipitation raises the electron density in this layer. Radio wave energy transferred to ambient electrons is converted to heat energy due to high collision rates in the lower atmosphere. Finally, the auroral precipitation can itself suppress the generation of the required short irregularity scale lengths. High electron densities are accompanied by high conductivity. This in turn results in weak electric fields. A small electric field is less effective in creating irregularities than a large electric field. Low growth rates for small electric fields can be balanced by diffusion or other temporal changes, so that essentially no radar-detectable irregularities are created. These different processes were found to play roles in the occurrence of HF backscatter. It can be difficult to identify the contribution of a particular mechanism in a given case.

The amount of backscatter varied between the days with data observations. Ionospheric electron density was suggested as an important factor for the backscatter reception. The amount of refraction of the radar beam close to the radar site determines the fraction of the radar beam usable for ionospheric probing. Unrefracted radio signals leave the top of the ionosphere without being able to be backscattered. Higher ambient densities result therefore in a larger fraction of beam power available for the detection of irregularities. It was speculated that high ambient plasma densities might be able to offset the adverse influence of a blanketing *E* layer.

The possible presence of polar cap patches was identified as a potential source for the varying nightside plasma densities. The patches are regularly observed throughout the polar cap. The occurrence and the convection path of polar cap patches are heavily influenced by the orientation and the magnitude of the interplanetary magnetic field. The small data

pool with available plasma density measurements was surveyed with respect to amount of backscatter, ionospheric density, and solar wind conditions. Unfortunately, the variability within the small set was too large for conclusive evidence. Suggestions for the test of this hypothesis and of the assumption about the importance of background ionospheric densities were made.

Thus, different processes such as ionization, plasma transport and diffusion, propagation and refraction of radio waves, and plasma instabilities are ingredients for the interplay between aurora and the detection of associated irregularities by HF radars. This is mirrored in the complex relationship between optical and HF radar aurora and illustrates the variability of the polar ionosphere. The diversity in the backscatter patterns, if properly understood, can reveal information about the state of ionospheric plasma in the auroral zone. The topic of correspondence between the visual aurora and associated HF backscatter is therefore not solved yet. A detailed specification of the ionosphere is required to resolve radar beam paths and to enable more progress on this field.

# Appendix A

## Statistical Approach

This appendix quantifies a statistical method attempted for the optical and radar data set. The preparation of the data was discussed in section 4.3 (p. 59). The starting point were data for the 41 data intervals, binned into geographical areas the same size as the radar cells. For the optical data this implied decreasing the spatial resolution and forming a median value with auroral brightness per cell. The time resolution was also adapted to the radar resolution. Data from the MSP and the allsky camera were compared separately to the radar data.

The obtained cells were sorted after the occurrence of aurora only, backscatter only, or both present. Two more groups were formed by adding all cells with auroral locations and backscatter locations, respectively.

The correlation coefficients between each two groups were found. The purpose of this calculation was to identify underlying mechanisms, as e.g. increased/decreased occurrence of backscatter for increased/decreased appearance of aurora. The degree of correlation is measured by the product moment correlation coefficient  $r$  defined as

$$r = 1/n \sum_i \frac{x_i - \bar{x}}{\sigma_x} * \frac{y_i - \bar{y}}{\sigma_y} \quad (\text{A.1})$$

where  $\bar{x}$  and  $\bar{y}$  are the mean values and  $\sigma_x$  and  $\sigma_y$  the standard deviations of the two samples to be correlated [Moroney, 1968]. Its value between  $-1$  through to  $+1$  indicates the degree of negative correlation to no relationship to positive correlation.

The resulting numbers for the daily averages for the Svalbard and the Alaskan data separately with the constellation radar/MSP and radar/ASC are shown in table A.1. The table can be read asking questions of the form: "If the occurrence in group A increases, to which degree is the occurrence in group B correlated?" Group A and group B are any combinations between

- AandB - cells with aurora and backscatter present
- AnoB - cells with aurora present, no backscatter
- BnoA - cells with backscatter present, no aurora
- totalA - total number of auroral cells in the FOV
- totalB - total number of backscatter cells in the FOV

	Svalbard		Alaska	
	ASC/Radar	MSP/Radar	ASC/Radar	MSP/Radar
AandB / AnoB:	0.11	0.58	0.65	0.44
AandB / BnoA:	0.48	0.24	0.01	0.40
AnoB / BnoA:	-0.17	0.30	-0.33	-0.12
totalA / totalB:	0.06	0.83	0.31	0.20
AandB / totalA:	0.44	0.86	0.95	0.74
AnoB / totalA:	0.94	0.92	0.86	0.93
BnoA / totalA:	0.01	0.31	-0.13	0.06
AandB / totalB:	0.56	0.92	0.46	0.52
AnoB / totalB:	-0.15	0.60	0.00	-0.03
BnoA / totalB:	1.00	0.60	0.89	0.99

Table A.1. Product moment correlation coefficients for various combinations of auroral and backscatter occurrence.

The correlation coefficients are very varying within an instrument group and for the different geographical locations. The consistently highest coefficients are found where the

total number of aurora or backscatter increases: the increase is mainly at locations which shows no increase in occurrence of the opposite group.

The variations between the coefficients for the two optical instruments is partly explained by the dominance of the emissions at lower altitudes in the ASC images, whereas in MSP records the red auroral line was used for the determination of aurora. The same calculations with hourly values instead of daily averages did not introduce qualitatively different results. Also still higher time resolutions for a smaller data set did not improve this trend. Furthermore the distribution of occurrences within the FOV plays an important role for a qualitative analysis. The locations of backscatter with respect of aurora are disregarded in this approach. A relation to the Kp indices, as well as the local magnetic field (with the help of local magnetometer) was investigated. Here again the spread was found to be too large for conclusive evidence.

Significance tests were performed to determine whether the correlation analysis is meaningful for this particular data set. Results ranging from "probably significant" to "highly significant" were obtained. However, these results are ambiguous, since the data in the different groups described above are related to each other by the maximum number of cells available in the common FOV. An independent increase or decrease in occurrence is therefore not possible. The significances calculated by methods described by *Moroney* [1968] were indistinguishable from significances attributable to the behavior of large groups versus small groups under such conditions.

The large variations in the calculated correlation coefficients and the lack of unambiguous significance leads therefore to the conclusion that this method proves not suitable for this kind of data set. The inspection of the large number of possible backscatter patterns in the presence of aurora, as illustrated in chapter 4, underlines the difficulty to quantify the relationship between auroral and HF backscatter.

Yet another attempt to categorize the temporal development was made. It consisted of an investigation of time sequences for the above mentioned groups and their time derivative. This did not provide statistically significant results. The fluctuations were too high for a definite evidence. However, it proved useful in the cases where time delays between aurora and backscatter were observed. A fragment of this procedure is found in the lower panels

of the data diagrams in chapter 4, showing the time sequence for two of the groups (total aurora and total backscatter).



# Bibliography

- Aarons, J.. A descriptive model of  $F$  layer high-latitude irregularities as shown by scintillation observations. *J. Geophys. Res.*, 78, 7441, 1973.
- Aikio, A. T., H. J. Opgenoorth, M. A. L. Persson, and K. U. Kaila. Ground-based measurements of an arc-associated electric field. *J. Atmos. Terr. Phys.*, 55, 797, 1993.
- Al'pert, Y. L.. *Radio Wave Propagation and the Ionosphere*, vol. 1. The Ionosphere, 430 pp., Consultants Bureau, New York, 1973.
- Anderson, D. N., J. Buchau, and R. A. Heelis. Origin of density enhancements in the winter polar cap ionosphere. *Radio Sci.*, 23, 513, 1988.
- Armstrong, J. C., and J. Zmuda. Field-aligned current at 1100 km in the auroral region measured by satellite. *J. Geophys. Res.*, 75, 7122, 1970.
- Baker, K. B., J. R. Dudeney, R. A. Greenwald, M. Pinnock, A. S. Rodger, N. Mattin, and C.-I. Meng. HF radar signatures of the cusp and low-latitude boundary layer. *J. Geophys. Res.*, 100, 7671, 1995.
- Baschin, O.. Die ersten Nordlichtphotographien. *Met. Zeitschr.*, (17), 1900.
- Basu, S., and J. Aarons. The morphology of high-latitude VHF scintillations near 70° W. *Radio Sci.*, 15, 59, 1980.
- Basu, S., E. MacKenzie, S. Basu, H. C. Carlson, D. Hardy, F. J. Rich, and R. C. Livingston. Coordinated measurements of low-energy precipitation and scintillations/TEC in the auroral oval. *Radio Sci.*, 18, 1151, 1983.

- Basu, S., S. Basu, E. MacKenzie, P. F. Fougere, W. R. Cowley, N. Maynard, J. D. Winningham, M. Sugiura, W. B. Hanson, and W. R. Hoegy. Simultaneous density and electric field fluctuation spectra associated with velocity shears in the auroral oval. *J. Geophys. Res.*, *93*, 115, 1988.
- Basu, S., E. J. Weber, T. W. Bulet, M. J. Keskinen, E. MacKenzie, P. Doherty, R. Sheenan, H. Kuenzler, P. Ning, and J. Bongiolatti. Characteristics of plasma structuring in the cusp/cleft region at Svalbard. *Radio Sci.*, *33*, 1885, 1998.
- Bates, H. F.. The height of *F* layer irregularities in the arctic ionosphere. *J. Geophys. Res.*, *64*, 1257, 1959.
- Bates, H. F.. HF propagation through the auroral curtain. *J. Geophys. Res.*, *75*, 143, 1970.
- Bates, H. F., and P. R. Albee. Aspect sensitivity of HF auroral echo. *J. Geophys. Res.*, *74*, 1164, 1969.
- Bilitza, D.. International Reference Ionosphere IRI-95. NSSDC, accessible on the internet at url: <http://nssdc.gsfc.nasa.gov/space/model/models/iri.html>. 1995.
- Bristow, W. A., R. A. Greenwald, and J. C. Samson. Identification of high-latitude acoustic gravity waves sources using the Goose Bay HF radar. *J. Geophys. Res.*, *99*, 319, 1994.
- Cerisier, J. C., J. J. Berthelier, and C. Beghin. Unstable density gradients in the high-latitude ionosphere. *Radio Sci.*, *20*, 755, 1985.
- Chaturvedi, P. K.. Collisional ion cyclotron waves in the auroral ionosphere. *J. Geophys. Res.*, *81*, 6169, 1976.
- Chaturvedi, P. K., and S. L. Ossakow. The current convective instability as applied to the auroral ionosphere. *J. Geophys. Res.*, *86*, 4811, 1981.
- Clark, D. H., and W. J. Raitt. The global morphology of irregularities in the topside ionosphere, as measured by the total ion current probe on ESRO-4. *Planet. Space Sci.*, *24*, 873, 1976.
- Davidson, G. T.. Expected spatial distribution of low-energy protons precipitated in the auroral zones. *J. Geophys. Res.*, *70*, 1061, 1965.

- Davies, K., *Ionospheric Radio Propagation*. 470 pp., National Bureau of Standard Monographs, Washington, 1965.
- de la Beaujardière, O., R. Vondrak, and M. Baron. Radar observations of electric fields and currents associated with auroral arcs. *J. Geophys. Res.*, *82*, 5051, 1977.
- Dyson, P. L., Direct measurements of the size and amplitude of irregularities in the topside ionosphere. *J. Geophys. Res.*, *74*, 6291, 1969.
- Dyson, P. L., and J. D. Winningham. Topside ionospheric spread *F* and particle precipitation in the dayside ionospheric clefts. *J. Geophys. Res.*, *79*, 5219, 1974.
- Dyson, P. L., J. P. McClure, and W. B. Hanson. In situ measurements of the spectral characteristics of *F* region ionospheric irregularities. *J. Geophys. Res.*, *79*, 1497, 1974.
- Evans, J. V., Theory and practice of ionospheric study by Thomson scatter radar. *Proceedings of the IEEE*, *57*, 496, 1969.
- Fejer, B. G., and M. C. Kelley. Ionospheric irregularities. *Rev. Geophys.*, *18*, 401, 1980.
- Feldstein, Y. I., and G. V. Starkov. Dynamics of the auroral belt. *Planet. Space Sci.*, *15*, 209, 1967.
- Frank, L. A., J. A. V. Allen, and J. D. Craven. Large diurnal variations of geomagnetically trapped and of precipitated electrons observed at low altitudes. *J. Geophys. Res.*, *69*, 3155, 1964.
- Frihagen, J., Occurrence of high latitude ionospheric irregularities giving rise to satellite scintillations. *J. Atmos. Terr. Phys.*, *33*, 21, 1971.
- Frihagen, J., and T. Jacobsen. In situ observation of high latitude *F* region irregularities. *J. Atmos. Terr. Phys.*, *33*, 519, 1971.
- Galperin, Y. I., and Y. I. Feldstein. Mapping of the precipitation regions to the plasma sheet. *J. Geomag. Geoelectr.*, *48*, 857, 1996.
- Greenwald, R. A., W. L. Ecklund, and B. B. Balsley. Radar observations of auroral electrojet currents. *J. Geophys. Res.*, *80*, 3635, 1975.

- Greenwald, R. A., K. B. Baker, R. A. Hutchins, and C. Hanuise. An HF phased-array for studying small-scale structure in the high-latitude ionosphere. *Radio Sci.*, 20, 63, 1985.
- Greenwald, R. A., K. B. Baker, and J. M. Ruohoniemi. Experimental evaluation of the propagation of high-frequency radar signals in a moderately disturbed high-latitude ionosphere. *John Hopkins APL Tech. Dig.*, 9, 131, 1988.
- Greenwald, R. A., K. B. Baker, J. R. Dudeney, M. Pinnock, T. B. Jones, E. C. Thomas, J.-P. Villain, J.-C. Cerisier, C. Senior, C. Hanuise, R. D. Hunsucker, G. Sofko, J. Kochler, E. Nielsen, R. Pellinen, A. D. M. Walker, N. Sato, and H. Yamagishi. DARN/SuperDARN. *Space Sci. Rev.*, 71, 761, 1995.
- Gussenhoven, M. S., D. A. Hardy, and N. Heinemann. Systematics of the equatorward diffuse auroral boundary. *J. Geophys. Res.*, 88, 5692, 1983.
- Hallinan, T. J., Auroral spirals. 2. Theory. *J. Geophys. Res.*, 81, 3959, 1976.
- Hanuise, C., High-latitude ionospheric irregularities: A review of recent radar results. *Radio Science*, 18, 1093, 1983.
- Hanuise, C., R. A. Greenwald, and K. B. Baker. Drift motions of very high latitude *F* region irregularities: Azimuthal Doppler analysis. *J. Geophys. Res.*, 90, 9717, 1985.
- Hanuise, C., J.-P. Villain, J. C. Cerisier, C. Senior, J. M. Ruohoniemi, R. A. Greenwald, and K. B. Baker. Statistical study of high-latitude *E* region doppler spectra obtained with the SHERPA HF radar. *Ann. Geophys.*, 9, 273, 1991.
- Hanuise, C., J.-P. Villain, D. Gresillon, B. Cabrit, R. A. Greenwald, and K. B. Baker. Interpretation of HF radar ionospheric doppler spectra by collective wave scattering theory. *Ann. Geophys.*, 11, 29, 1993.
- Hargreaves, J. K., *The solar-terrestrial environment*. 420 pp., Cambridge University Press, Cambridge, 1992.
- Heppner, J. P., Empirical models of high-latitude electric fields. *J. Geophys. Res.*, 82, 1115, 1977.

- Hess, W. N., *The Radiation Belt and Magnetosphere*. 548 pp., Blaisdell, Waltham, Massachusetts, 1968.
- Hower, G. L., D. M. Ranz, and C. L. Allison. Comparison of HF radar echoes and high-latitude spread *F* measurements. *J. Geophys. Res.*, *71*, 3215, 1966.
- Huba, J. D., and S. L. Ossakow. Influence of magnetic shear on the current convective instability in the diffuse aurora. *J. Geophys. Res.*, *85*, 6874, 1980.
- Huba, J. D., H. G. Mitchell, M. J. Keskinen, P. S. J. A. Fedder, and S. T. Zalesak. Simulations of plasma structure evolution in the high-latitude ionosphere. *Radio Science*, *23*, 503, 1988.
- Hudson, M. K., and M. C. Kelley. The temperature gradient drift instability at the equatorward edge of the ionospheric plasma through. *J. Geophys. Res.*, *81*, 3913, 1976.
- Idenden, D. W., R. J. Moffett, and S. Quegan. Ionospheric structure produced during a rapid polar cap expansion. *J. Geophys. Res.*, *102*, 14,581, 1997.
- Imran, U. S., Waves and instabilities. *Rev. Geophys.*, *25*, 588, 1987.
- James, H. G., and J. W. MacDougall. Signatures of polar cap patches in ground ionosonde data. *Radio Sci.*, *32*, 497, 1997.
- Johnson, M. L., J. S. Murphree, G. T. Marklund, and T. Karlsson. Progress on relating optical auroral forms and electric field patterns. *J. Geophys. Res.*, *103*, 4271, 1998.
- Jones, T. B., and C. T. Spacklen. A search for *E*-region disturbances induced by ion cloud release at *F*-region heights. *J. Atmos. Terr. Phys.*, *40*, 409, 1978.
- Kamide, Y., and S. Kokubun. Two-component auroral electrojet: Importance for substorm studies. *J. Geophys. Res.*, *101*, 13,027, 1996.
- Kelley, M. C., *The Earth's Ionosphere. Plasma Physics and Electrodynamics*. 484 pp., Academic Press, San Diego, California, 1989.
- Kelley, M. C., and C. W. Carlson. Observation of intense velocity shear and associated electrostatic waves near an auroral arc. *J. Geophys. Res.*, *82*, 2343, 1977.

- Kelley, M. C., and P. M. Kintner. Evidence for two-dimensional inertial turbulence in a cosmic scale low  $\beta$  plasma. *Astrophys. J.*, 220, 339, 1978.
- Kelley, M. C., and F. S. Mozer. A satellite survey of vector electric fields in the ionosphere at frequencies of 10-500 Hertz. 1. Isotropic, high-latitude electrostatic emissions. *J. Geophys. Res.*, 7, 4158, 1972.
- Kelley, M. C., C. W. Carlson, and F. S. Mozer. Production and distribution of *F* region irregularities. *EOS Trans. AGU*, 57, 297, 1976.
- Kelley, M. C., K. D. Baker, J. C. Ulwick, C. Rino, and M. J. Baron. Simultaneous rocket probe and incoherent scatter radar observations of irregularities in the auroral zone ionosphere. *Radio Sci.*, 15, 491, 1980.
- Kelley, M. C., J. F. Vickrey, C. W. Carlson, and R. Torbert. On the origin and spatial extent of high-latitude *F* region irregularities. *J. Geophys. Res.*, 87, 4469, 1982.
- Kelly, J. D., and V. B. Wickwar. Radar measurements of high-latitude ion composition between 140 and 300 km altitude. *J. Geophys. Res.*, 86, 7617, 1981.
- Kersley, L., C. D. Russell, and D. L. Rice. Phase scintillation and irregularities in the northern polar ionosphere. *Radio Sci.*, 30, 619, 1995.
- Keskinen, M. J., and J. D. Huba. Generation of lower hybrid waves by inhomogeneous electron streams. *J. Geophys. Res.*, 88, 3109, 1983.
- Keskinen, M. J., and S. L. Ossakow. Nonlinear evolution of plasma enhancements in the auroral ionosphere: 1. Long wavelength irregularities. *J. Geophys. Res.*, 87, 144, 1982.
- Keskinen, M. J., and S. L. Ossakow. Nonlinear evolution of plasma enhancements in the auroral ionosphere: 2. Small scale irregularities. *J. Geophys. Res.*, 88, 474, 1983a.
- Keskinen, M. J., and S. L. Ossakow. Theories of high-latitude ionospheric irregularities: A review. *Radio Sci.*, 18, 1077, 1983b.
- Keskinen, M. J., H. G. Mitchell, J. A. Fedder, P. Satyanarayana, S. T. Zalesak, and J. D. Huba. Nonlinear evolution of the Kelvin-Helmholtz instability in the high-latitude ionosphere. *J. Geophys. Res.*, 93, 137, 1988.

- Kintner, P. M.. Observations of velocity shear driven plasma turbulence. *J. Geophys. Res.*, *81*, 5114, 1976.
- Kirkwood, S., and A. Osepian. Quantitative studies of energetic particle precipitation using incoherent scatter radar. *J. Geomag. Geoelectr.*, *47*, 783, 1995.
- Krehbiel, J. P., L. H. Brace, R. F. Theis, W. H. Pinkus, and R. B. Kaplan. The Dynamics Explorer Langmuir probe instrument. *Space Science Instrumentation*, *5*, 493, 1981.
- Lakhina, G. S., and K. G. Bhatia. Ion cyclotron instability in the auroral *F* region. *J. Geophys. Res.*, *89*, 9845, 1984.
- Lanchester, B. S., K. U. Kaila, and I. W. McCrea. Relationship between large horizontal electric fields and auroral arc elements. *J. Geophys. Res.*, *101*, 5075, 1996.
- Lanchester, B. S., M. H. Rees, D. Lummerzheim, A. Otto, and H. U. Frey. Large fluxes of auroral electrons in filaments of 100 m width. *J. Geophys. Res.*, *102*, 9741, 1997.
- Lanchester, B. S., M. H. Rees, K. J. F. Sedgemore, J. R. Palmer, H. U. Frey, and K. U. Kaila. Ionospheric response to variable electric fields in small-scale auroral structure. *Ann. Geophys.*, *16*, 1343, 1998.
- Lanchester, B. S., M. H. Rees, D. Lummerzheim, K. J. F. Sedgemore-Schulthess, H. Zhu, and I. W. McCrea. Ohmic heating as evidence for strong field-aligned currents in filamentary aurora. *J. Geophys. Res.*, *accepted*, 2000.
- Lester, M., S. E. Milan, V. Besser, and R. W. Smith. A case study of HF radar spectra and 630.0 nm auroral emission in the pre-midnight sector. *Ann. Geophys.*, *accepted*, 2000.
- Lewis, R. V., M. P. Freeman, A. S. Rodger, G. D. Reeves, and D. K. Milling. The electric field response to the growth phase and expansion phase onset of a small isolated substorm. *Ann. Geophys.*, *15*, 289, 1997.
- Lockwood, M., S. W. H. Cowley, and M. P. Freeman. The excitation of plasma convection in the high-latitude ionosphere. *J. Geophys. Res.*, *95*, 7961, 1990.

- Lui, A. T. Y., R. W. McEntire, S. Ohtani, L. J. Zanetti, W. A. Bristow, R. A. Greenwald, P. T. Newell, S. P. Christon, T. Mukai, K. Tsurada, T. Yamamoto, S. Kokubun, H. Matsumoto, H. Kojima, T. Murata, D. H. Fairfield, R. P. Lepping, J. C. Samson, G. Rostoker, G. D. Reeves, A. L. Rodger, and H. J. Singer. Study of an isolated substorm with ISTP data. in *Geospace Mass and Energy Flow: Results from the International Solar-Terrestrial Physics Program*, edited by J. L. Horwitz et al., Geophysical Monograph 104, p. 261. American Geophysical Union, 1998.
- Lummerzheim, D., M. H. Rees, and G. J. Romick. The application of spectroscopic studies of the aurora to thermospheric neutral composition. *Planet. Space Sci.*, 38, 67, 1990.
- Lyatsky, W., R. D. Elphinstone, Q. Pao, and L. L. Cogger. Field line resonance interference model for multiple auroral arc generation. *J. Geophys. Res.*, 104, 263, 1999.
- Mantas, G. P., and J. C. G. Walker. The penetration of soft electrons into the ionosphere. *Planet. Space Sci.*, 24, 409, 1976.
- Marklund, G. T., T. Karlsson, L. G. Blomberg, P.-A. Lindqvist, C.-G. Fälthammar, M. L. Johnson, J. S. Murphree, L. E. L. Andersson, H. J. Opgenoorth, and L. J. Zanetti. Observations of the electric field fine structure associated with the westward traveling surge and large-scale auroral spirals. *JGR*, 103, 4125, 1998.
- Maynard, N. C., J. P. Heppner, and A. Egeland. Intense, variable electric fields at ionospheric altitudes in the high-latitude regions as observed by DE-2. *Geophys. Res. Lett.*, 9, 981, 1982.
- McClure, J. P., and W. B. Hanson. A catalog of ionospheric *F* region irregularity behavior based on Ogo 6 retarding potential analyzer data. *J. Geophys. Res.*, 78, 7431, 1973.
- McEwen, D. J., and D. P. Harris. Occurrence pattern of *F* layer patches over the north magnetic pole, *Radio Sci.*, 31, 619, 1996.
- Mikhailovskii, A. B., *Theory of Plasma Instabilities*, vol. 2, 314 pp., Consultants Bureau, New York, 1974.



- Milan, S. E., M. Lester, and J. Moen. A comparison of optical and coherent HF radar backscatter observations of a post-midnight aurora. *Ann. Geophys.*, *15*, 1388, 1997a.
- Milan, S. E., T. B. Jones, T. R. Robinson, E. C. Thomas, and T. K. Yeoman. Interferometric evidence for the observation of ground backscatter originating behind the CUTLASS coherent HF radars. *Ann. Geophys.*, *15*, 29, 1997b.
- Milan, S. E., J. A. Davies, and M. Lester. Coherent HF radar backscatter associated with auroral forms identified by incoherent radar techniques: A comparison of CUTLASS and EISCAT observations. *J. Geophys. Res.*, *104*, 591, 1999.
- Mitchel, H. G., Jr., J. A. Fedder, M. J. Keskinen, and S. T. Zalesak. A simulation of high-latitude *F*-layer instabilities in the presence of magnetosphere-ionosphere coupling. *Geophys. Res. Lett.*, *12*, 283, 1985.
- Moen, J., H. C. Carlson, S. E. Milan, N. Shumilov, B. Lybekk, P. E. Sandholt, and M. Lester. On the collocation between dayside auroral activity and coherent HF backscatter. *Ann. Geophys.*, *submitted*, 2000.
- Möller, H. G., Backscatter results from Lindau, II. The movement of curtains of intense irregularities in the polar *F* layer. *J. Atmos. Terr. Phys.*, *36*, 1487, 1974.
- Möller, H. G., and A. Tauriainen. Observations of intense irregularities in the polar *F* region by HF backscatter and satellite scintillation measurements. *J. Atmos. Terr. Phys.*, *37*, 161, 1975.
- Morelli, J. P., R. J. Bunting, S. W. H. Cowley, C. F. Farrugia, M. P. Freeman, E. Friis-Christensen, G. O. L. Jones, M. Lester, R. V. Lweis, H. Lühr, D. Orr, M. Pinnock, G. D. Reeves, P. J. S. Williams, and T. K. Yeoman. Radar observations of auroral zone flows during a multiple-onset substorm. *Ann. Geophys.*, *13*, 1144, 1995.
- Moroney, M. J., *Facts from Figures*, 472 pp., Penguin Books, Middlesex, England, 1968.
- Muldrew, D. B., and J. F. Vickrey. High-latitude *F* region irregularities observed simultaneously with ISIS 1 and the Chatanika radar. *J. Geophys. Res.*, *87*, 8263, 1982.

- Narcisi, R. S., and A. D. Bailey. Mass spectrometric measurements of positive ions at altitudes from 64 to 112 kilometers. *J. Geophys. Res.*, 70, 3687, 1965.
- Olsson, A., L. Andersson, A. I. Eriksson, J. Clemmons, R. E. Erlandsson, G. Reeves, T. Hughes, and J. S. Murphree. Freja studies of the current-voltage relation in substorm-related events. *J. Geophys. Res.*, 103, 4285, 1998.
- Omholt, A., *The Optical Aurora*, 168 pp., Springer Verlag, Heidelberg, 1971.
- Ossakow, S. L., and P. K. Chaturvedi. Current convective instability in the diffuse aurora. *Geophys. Res. Lett.*, 6, 332, 1979.
- O'Brien, B. J., Lifetimes of outer-zone electrons and their precipitation into the atmosphere. *J. Geophys. Res.*, 67, 3687, 1962.
- Pedersen, T. R., B. G. Fejer, R. A. Doe, and E. J. Weber. Incoherent scatter radar observations of horizontal *F* region plasma structure over Sondrestrom, Greenland, during polar cap patch events. *Radio Sci.*, 6, 1847, 1998.
- Perkins, F. W., and D. L. Jassby. Velocity shear and low frequency plasma instabilities. *Phys. Fluids*, 14, 102, 1971.
- Prikryl, P., G. J. Sofko, J. A. Koehler, J. Mu, and D. André. Steep electron gradients associated with discrete aurorae explaining the diversity of aurora VHF doppler spectra. *Ann. Geophys.*, 13, 25, 1995.
- Rees, M., Auroral ionization and excitation by incident energetic electrons. *Planet. Space Sci.*, 11, 1209, 1963.
- Rees, M. H., *Physics and Chemistry of the Upper Atmosphere*, 289 pp., Cambridge University Press, Cambridge, 1988.
- Reid, G. C., The formation of small-scale irregularities in the ionosphere. *J. Geophys. Res.*, 73, 1627, 1968.
- Rino, C. L., R. C. Livingston, and S. J. Matthews. Evidence for sheet-like auroral ionospheric irregularities. *Geophys. Res. Lett.*, 5, 1039, 1978.

- Rino, C. L., R. C. Livingston, R. T. Tsunoda, R. M. Robinson, J. F. Vickrey, C. Senior, M. D. Cousins, J. Owen, and J. A. Klobuchar. Recent studies of the structure and morphology of auroral zone *F* region irregularities. *Radio Sci.*, 18, 1167, 1983.
- Robinson, R. M., R. T. Tsunoda, J. F. Vickrey, and L. Guerin. Source of *F* region ionization enhancements in the nighttime auroral zone. *J. Geophys. Res.*, 90, 7533, 1985.
- Roble, R. G., and M. H. Rees. Time-dependent studies of the aurora: Effects of particle precipitation on the dynamic morphology of ionospheric and atmospheric properties. *Planet. Space Sci.*, 25, 991, 1977.
- Rodger, A. S., M. Pinnock, J. D. Dudeney, K. B. Baker, and R. A. Greenwald. A new mechanism for patch formation. *J. Geophys. Res.*, 99, 6425, 1994.
- Rodger, A. S., S. B. Mende, T. J. Rosenberg, and K. B. Baker. Simultaneous optical and HF radar observations of the cusp. *Geophys. Res. Lett.*, 22, 2045, 1995.
- Ronick, G. J., W. L. Ecklund, R. A. Greenwald, B. B. Balsley, and W. L. Imhof. The interrelationship between the >130 keV electron trapping boundary, the VHF radar backscatter, and the visual aurora. *J. Geophys. Res.*, 79, 2439, 1974.
- Ruohoniemi, J. M., and R. A. Greenwald. Statistical pattern of high-latitude convection obtained from Goose Bay HF radar observations. *J. Geophys. Res.*, 101, 21,743, 1996.
- Ruohoniemi, J. M., and R. A. Greenwald. Rates of scattering occurrence in routine HF radar observations during solar cycle maximum. *Radio Sci.*, 32, 1051, 1997.
- Ruohoniemi, J. M., R. A. Greenwald, K. B. Baker, and J.-P. Villain. Drift motions of small-scale irregularities in the high-latitude *F* region: An experimental comparison with plasma drift motions. *J. Geophys. Res.*, 92, 4553, 1987.
- Ruohoniemi, J. M., R. A. Greenwald, K. B. Baker, J.-P. Villain, C. Hamise, and J. Kelly. Mapping high-latitude plasma convection with coherent HF radars. *J. Geophys. Res.*, 94, 13,463, 1989.
- Sagalyn, R. C., M. Smiddy, and M. Ahmed. High latitude irregularities in the topside ionosphere based on ISIS-1 thermal ion probe data. *J. Geophys. Res.*, 79, 4252, 1974.

- Samson, J. C., R. A. Greenwald, J. M. Ruohoniemi, and K. B. Baker. High-frequency radar observations of atmospheric gravity waves in the high-latitude ionosphere. *Geophys. Res. Lett.*, *16*, 875. 1989.
- Satyanarayana, P., and P. K. Chaturvedi. Theory of the current-driven ion cyclotron instability in the bottomside ionosphere. *J. Geophys. Res.*, *90*, 12,209. 1985.
- Shimazaki, T., A statistical study of world-wide occurrence probability of spread-*F*. 2. Abnormal state in severe magnetic storms. *J. Radio Res. Labs.*, *6*, 688. 1959.
- Sojka, J. J., M. D. Bowline, R. W. Schunk, D. T. Decker, C. E. Valladares, R. Sheenan, D. N. Anderson, and R. A. Heelis. Modeling polar cap *F*-region patches using time varying convection. *Geophys. Res. Lett.*, *20*, 1783. 1993.
- Sojka, J. J., M. V. Subramaniam, L. Zhu, and R. W. Schunk. Gradient drift instability growth rates from global-scale modeling of the polar ionosphere. *Radio Sci.*, *33*, 1915. 1998.
- Stasiewicz, K., and T. A. Potemra. Multiscale current structures observed by Freja. *J. Geophys. Res.*, *103*, 4315. 1998.
- Temerin, M., and P. M. Kintner. Review of ionospheric turbulence, in *Plasma waves and instabilities at comets and in magnetospheres*, edited by B. T. Tsurutani and H. Qya. Geophysical Monograph 53, p. 65. American Geophysical Union, Washington DC. 1989.
- Tsunoda, R. T., High-latitude *F* region irregularities: A review and synthesis. *Rev. Geophys.*, *26*, 719. 1988.
- Uspensky, M. V., P. J. S. Williams, V. I. Romanov, V. G. Pivovarov, G. J. Sofko, and J. A. Kochler. Auroral radar backscatter at off-perpendicular aspect angles due to enhanced ionospheric refraction. *J. Geophys. Res.*, *99*, 17,503. 1994.
- Vallance Jones, A., *Aurora*, 301 pp., D. Reidel Publishing Company, Dordrecht, 1974.
- Vickrey, J. F., and M. C. Kelley. The effect of a conducting *E* layer on classical *F* region cross-field plasma diffusion. *J. Geophys. Res.*, *87*, 4461. 1982.

- Vickrey, J. F., C. L. Rino, and T. A. Potemra, Chatanika/Triad observations of unstable ionization enhancements in the auroral *F* region. *Geophys. Res. Lett.*, *7*, 789, 1980.
- Vickrey, J. F., R. C. Livingston, N. B. Walker, T. A. Potemra, R. A. Heelis, and F. J. Rich, On the current-voltage relationship of the magnetospheric generator at small spatial scales. *Geophys. Res. Lett.*, *13*, 495, 1982.
- Villain, J.-P., R. A. Greenwald, and J. F. Vickrey, HF ray tracing at high latitudes using measured meridional electron density distributions. *Radio Sci.*, *19*, 359, 1984.
- Villain, J.-P., G. Caudal, and C. Hanuise, A SAFARI-EISCAT comparison between the velocity of *F* region small-scale irregularities and the ion drift. *J. Geophys. Res.*, *90*, 8433, 1985.
- Voronkov, I., E. Friedrich, and J. C. Samson, Dynamics of the substorm growth phase as observed using CANOPUS and SuperDARN instruments. *J. Geophys. Res.*, *104*, 28,491, 1999.
- Waldock, J. A., and T. B. Jones, Statistics of 1-m wavelength plasma irregularities and convection in the auroral *E* region. *Radio Sci.*, *20*, 709, 1985.
- Walker, A. D. M., R. A. Greenwald, and K. B. Baker, Determination of the fluctuation level of ionospheric irregularities from radar backscatter measurements. *Radio Sci.*, *22*, 689, 1987.
- Weaver, P. F., Backscatter echoes from field-aligned irregularities in the *F* region. *J. Geophys. Res.*, *70*, 5425, 1965.
- Weber, E. J., J. F. Vickrey, H. Gallagher, L. Weiss, C. J. Heinselman, R. A. Heelis, and M. C. Kelley, Coordinated radar and optical measurements of stable auroral arcs at the polar cap boundary. *J. Geophys. Res.*, *96*, 17,847, 1991.
- Williams, D. J., Ring current and radiation belts. *Rev. Geophys.*, *25*, 570, 1987.
- Williams, P. J. S., B. Jones, A. V. Kustov, and M. V. Uspensky, The relationship between *E* region electron density and the power of auroral coherent echoes at 45 MHz. *Radio Sci.*, *34*, 449, 1999.

Yeoman, T. K., and H. Lühr. CUTLASS/IMAGE observations of high-latitude convection features during substorms. *Ann. Geophys.*, 15, 692, 1997.

Zhu, L., R. W. Schunk, J. J. Soika, and M. David. Model study of ionospheric dynamics during a substorm. *J. Geophys. Res.*, 105, 15.807, 2000.